

In vivo Magnetic Resonance Spectroscopy and Diffusion Weighted Magnetic Resonance Imaging for Non- Invasive Monitoring of Treatment Response of Subcutaneous HT29 Xenografts in Mice

Kathrine Røe

Master of Science in Electronics

Submission date: June 2006

Supervisor: Tor Audun Ramstad, IET

Co-supervisor: Therese Seierstad, Radiumhospitalet

Problem Description

Oppgaven vil bestå i å følge behandlingsrespons hos mus ved bruk av in vivo magnetisk resonans spektroskopi (MRS) og diffusjonsvektet magnetisk resonans (MR) avbildning. På ulike tidspunkter i forsøkene opereres tumor ut for histologisk bestemmelse av behandlingsrespons og korrelasjon med MR-data. En del av tumor legges på flytende nitrogen for høyoppløselig ex vivo MRS analyse og korrelasjon mellom ex vivo og in vivo MRS data.

Musene får både strålebehandling og medikamentell behandling med cytostatika og strålesensitiserende stoffer. Denne behandlingen er valgt på bakgrunn av den pågående kliniske pasientstudien LARC-RRP (Locally Advanced Rectal Cancer – Radiation Response Prediction) ved Rikshospitalet-Radiumhospitalet HF. Pasienter som inkluderes i studien har store tumorer som mottar medikamentell behandling og stråleterapi for å redusere tumorstørrelsen slik at den kan fjernes kirurgisk. Noen av pasientene vil ikke ha effekt av denne preoperative behandlingen og målet med LARC-RRP-studien er å identifisere faktorer som kan forutsi behandlingsresponsen.

Alle undersøkelser innbefatter avbildning og opptak av data på en av sykehusets kliniske MR-maskiner.

Assignment given: 16. January 2006
Supervisor: Tor Audun Ramstad, IET

Abstract

This work investigates whether *in vivo* magnetic resonance spectroscopy (MRS) and diffusion-weighted magnetic resonance imaging (DW-MRI) can be used for non-invasive monitoring of treatment response in an experimental tumor model.

Twenty-nine nude mice with colorectal adenocarcinoma HT29 xenografts on each flank were included into 2 separate experiments. In the first experiment control tumors were compared to tumors irradiated with 15 Gy at Day 2. MR baseline values were established at Day 1 followed by 4 post-treatment MR examinations. Mice were sacrificed for histological response evaluation and high-resolution *ex vivo* magic angle spinning (HR-MAS) MRS of tumor tissue samples for correlation with *in vivo* MR data.

The second experiment included 3 groups receiving combined chemoradiation therapy; Control group, Capecitabine (359 mg/kg daily Day 1 - Day 5) group and Capecitabine (359 mg/kg daily Day 1 - Day 5) + Oxaliplatin (10 mg/kg at Day 2) group. All left-sided tumors were irradiated with 15 Gy at Day 2. Three repeated MR examinations were compared to the MR baseline values established at Day 1. After MR examinations the mice were sacrificed for histological response evaluation. The choice of chemotherapy was based on a clinical patient study currently running at Rikshospitalet-Radiumhospitalet HF, the LARC-RRP (Locally Advanced Rectal Cancer - Radiation Response Prediction) study.

In Experiment 1, localized ^1H MR spectra were acquired at short (35 ms) and long (144 ms) echo times (TEs) using a single-voxel technique. The metabolite choline is related to tumor growth. The choline peak area relative to the unsuppressed 35 ms TE water area in the same voxel, i.e. the normalized choline ratio, was assessed in all MRS examinations. For both TEs, the choline ratio increased after irradiation, followed by a decrease and a renewed increase 12 days after irradiation. In Experiment 1, statistically significant differences at the 0.1 level were observed between the choline ratios at Day 5 and Day 12 ($p = 0.068$) for short TE and between the ratios at Day 3 and Day 8 ($p = 0.05$) for long TE. The change in choline ratio was in accordance with the tumor necrotic fraction (NF) found in histological analyses. Principal component analysis (PCA) revealed a correlation between the score values of *ex vivo* HR-MAS MR spectra and necrosis. This suggests a correlation between *ex vivo* and *in vivo* MRS.

In both experiments, the diffusion in the HT29 xenografts varied during treatment. There was a correlation between the amount of necrosis in tumor and the calculated apparent diffusion coefficient (ADC) obtained from DW-MRI examinations. In Experiment 1, statistically significant differences at the 0.1 level were observed between the ADCs at Day 3 and Day 5 ($p = 0.05$), between Day 5 and Day 12 ($p = 0.068$), and between Day 8 and Day 12 ($p = 0.068$).

The HT29 xenografts responded to treatment with an initial increase of necrosis due to the short-term effect of treatment, stimulating development of fibrosis. In accordance to the change in choline and ADC, the level of necrosis increased 8 - 12 days after start of treatment, which might correspond to the long-term effect of treatment.

The findings in this work shows that *in vivo* MRS and DW-MRI can be used for non-invasive monitoring of treatment response in an experimental tumor model. This suggests that *in vivo* MRS and DW-MRI could yield important information about a tumors response to therapy.

Preface

This report documents my work on my final master thesis at the Department of Electronics and Telecommunications, Faculty of Information Technology, Mathematics and Electrical Engineering, at the Norwegian University of Science and Technology (NTNU), spring semester 2006.

The work was carried out at the Department of Medical Physics at Rikshospitalet-Radiumhospitalet HF in Oslo under the kind supervision of PhD student Therese Seierstad. I would like to thank her for all the valuable help and support during the work.

I would also like to thank Professor dr.med. Hans Henrik Lien at the MR department for letting me use the clinical MR scanner, radiologist Knut Håkon Hole for sharing his office with mice and students, post doc. Beathe Sitter at the MR centre at St. Olavs Hospital in Trondheim for help with HR-MAS and PCA analysis, engineer Marita Martinsen at the Department of Tumor Biology for inoculation of tumor tissue in mice, Histologisk Forskningslab for preparation of HE-stains, Inger and Anne Lise for giving my mice water, food and clean cages, and physician Sigurd Folkvord for his friendly attitude and help with the chemotherapy.

Oslo, June 19, 2006

Kathrine Røe

Nomenclature

ADC Apparent Diffusion Coefficient

BW Bandwidth

Chemotherapy The treatment of disease by the administration of chemical agents

CSI Chemical Shift Imaging

DW-MRI Diffusion Weighted - Magnetic Resonance Imaging

DTI Diffusion Tensor magnetic resonance Imaging

EPI Echo Planar Imaging

ETL Echo Train Length

FID Free Induction Decay

FSE Fast Spin Echo

FOV Field of View

Gray The SI unit of radiation dose absorbed from a field of ionizing radiation

HR-MAS High Resolution - Magic Angle Spinning

in vivo An investigation or procedure carried out in the living organism or human body

in vitro An investigation performed on material of biological origin, which may include living cells, but in inanimate surroundings

LARC-RRP Locally Advanced Rectal Cancer - Radiation Response Prediction

MR Magnetic Resonance

MRI Magnetic Resonance Imaging

MRS Magnetic Resonance Spectroscopy

NMR Nuclear Magnetic Resonance

PCA Principal Component Analysis

PRESS Point Resolved Spectroscopy

Radiation therapy The treatment of disease by the use of ionizing radiation

ROI Region of Interest

SE Spin Echo

SSFSE Single Shot Fast Spin Echo

STEAM Stimulated Echo Acquisition Mode

TLD Thermo Luminescence Dosimetry

VOI Volume of Interest

Xenograft Human tumors grown in experimental animals

Contents

| | | |
|----------|--|-----------|
| 1 | Introduction | 1 |
| 2 | Background | 5 |
| 2.1 | Cancer | 5 |
| 2.1.1 | Colorectal Cancer | 6 |
| 2.1.2 | Treatment of Colorectal Cancer | 6 |
| 2.1.3 | LARC-RRP | 9 |
| 2.2 | Biochemistry of the Cell | 10 |
| 2.2.1 | Metabolism in Human Cells | 10 |
| 2.2.2 | Metabolism of Tumors | 14 |
| 2.3 | Magnetic Resonance Imaging | 15 |
| 2.3.1 | Principles of Magnetic Resonance | 15 |
| 2.3.2 | Spin Echo | 19 |
| 2.3.3 | Image Reconstruction | 20 |
| 2.3.4 | Imaging Coils | 22 |
| 2.4 | Magnetic Resonance Spectroscopy | 23 |
| 2.4.1 | Principles of MR Spectroscopy | 23 |
| 2.4.2 | Splitting | 24 |
| 2.4.3 | Multi-Dimensional Spectroscopy and CSI | 27 |
| 2.5 | High Resolution - Magic Angle Spinning, HR-MAS | 27 |
| 2.5.1 | Principles of HR-MAS MR Spectroscopy | 27 |
| 2.5.2 | Analysis of HR-MAS Spectra | 29 |
| 2.6 | Diffusion-Weighted Magnetic Resonance Imaging | 30 |
| 2.6.1 | Principles of Diffusion Imaging | 30 |
| 2.7 | Thermo Luminescence Dosimetry (TLD) | 33 |
| 2.8 | Human Xenografts as Tumor Models | 35 |
| 2.9 | Software | 35 |
| 3 | Materials and Methods | 37 |
| 3.1 | Experimental Animals and Anaesthesia | 37 |
| 3.1.1 | Experimental Animals and Tumor Model | 37 |
| 3.1.2 | Anaesthesia | 38 |
| 3.2 | Description of the Experiments | 38 |

| | | |
|----------|--|-----------|
| 3.2.1 | Experiment 1 | 38 |
| 3.2.2 | Experiment 2 | 39 |
| 3.3 | Radiation Therapy | 40 |
| 3.4 | Chemotherapy | 43 |
| 3.5 | MR | 44 |
| 3.5.1 | Preparations for MR Acquisitions | 44 |
| 3.5.2 | MR Imaging | 45 |
| 3.6 | Tumor Tissue Samples | 48 |
| 3.6.1 | Tumor Tissue Samples for Histology | 48 |
| 3.6.2 | Tumor Tissue Samples for <i>ex vivo</i> HR-MAS MR Spectroscopy | 50 |
| 3.7 | Post-Processing Analyses | 52 |
| 3.7.1 | Calculation of Tumor Volume from MR Images | 52 |
| 3.7.2 | Spectroscopy | 52 |
| 3.7.3 | <i>Ex vivo</i> HR-MAS Spectroscopy | 52 |
| 3.7.4 | Diffusion | 53 |
| 3.8 | Statistics | 53 |
| 4 | Results | 55 |
| 4.1 | Experiment 1 | 55 |
| 4.1.1 | Radiation Therapy | 55 |
| 4.1.2 | Tumor Growth Curves | 55 |
| 4.1.3 | Tumor Histology | 57 |
| 4.1.4 | <i>In vivo</i> MR Spectroscopy | 59 |
| 4.1.5 | Diffusion Tensor Imaging (DTI) and ADC | 61 |
| 4.1.6 | <i>Ex vivo</i> HR-MAS MR Spectroscopy | 62 |
| 4.2 | Experiment 2 | 68 |
| 4.2.1 | Chemoradiation Therapy | 69 |
| 4.2.2 | Tumor Growth Curves | 70 |
| 4.2.3 | Tumor Histology | 72 |
| 4.2.4 | <i>In vivo</i> MR Spectroscopy | 73 |
| 4.2.5 | Diffusion Tensor Imaging (DTI) and ADC | 74 |
| 5 | Discussion | 77 |
| 5.1 | Tumor Model | 77 |
| 5.2 | Radiation- and Chemotherapy | 78 |
| 5.3 | Calculation of Tumor Volume | 79 |
| 5.4 | Histology | 80 |
| 5.5 | <i>In vivo</i> MR Spectroscopy | 82 |
| 5.6 | Diffusion Tensor Imaging and ADC | 83 |
| 5.7 | <i>Ex vivo</i> HR-MAS MR Spectroscopy | 85 |
| 5.8 | Clinical Relevance | 86 |
| 5.9 | Suggestions for Further Work | 88 |
| 6 | Conclusion | 89 |

Chapter 1

Introduction

In Norway, colorectal cancer was the second most frequently type of cancer diagnosed in 2004, with a total of 3482 new incidences. The disease occurs at all ages, but with a majority of older people, where 85.4 % of men and 77.3 % of women were older than 55 years [1].

Locally Advanced Rectal Cancer - Radiation Response Prediction (LARC-RRP) is a large study of patients with locally advanced rectal cancer, started at Rikshospitalet-Radiumhospitalet HF in September 2005. This is a group of patients with large tumors which are receiving chemotherapy and radiation therapy to reduce the size of the tumor prior to surgery. Some of these patients do not respond to the pre-operative treatment and the aim of the LARC-RRP study is to identify factors which can predict tumor response to radiation therapy and chemotherapy.

Radiation therapy cures most cancer patients next to surgery, and has evolved into its current status through a century of research in physics, medicine and biology. But still, approximately 1 out of 5 cancer patients die with loco-regional failure. Insight in the mechanisms of response to therapy may improve response and thus survival.

During the recent few years, several new chemotherapeutics and biologically targeting drugs have been available for treatment of advanced colorectal cancer. Although a drug has shown efficient in the metastatic setting, it does not necessarily mean it would increase radiosensitivity of that tumor type. Upon the use as radiosensitizers, the drugs are thought to improve the therapeutic efficacy of radiation therapy in the preoperative setting. The possible mechanisms of radiosensitization needs to be tested in experimental tumor models.

Tumor response to radiation is influenced by cellular, proliferative and tumor physiological factors. Targeted radiation oncology requires understanding of the basic, underlying biologic mechanisms, namely the molecular signatures of radiation response. Based on altered and/or specific metabolic profiles, including those of choline-containing compounds

and liquids, analytical ^1H Magnetic Resonance Spectroscopy (MRS) has demonstrated its potential in diagnosis and grading of colorectal adenocarcinoma.

MRS reveals spectra that are made up of signals at slightly different frequencies, depending on the positions of the atomic nuclei giving rise to them in the molecule. Nuclei in different local chemical environments produce signals at different frequencies and are therefore observed at different positions in the spectrum. The resonance frequency is called the chemical shift, and is in the dimensionless unit part-per-million (ppm). Chemical shifts allow identification of individual compounds in a sample, and for a given signal, the area under the curve is proportional to the concentration of nuclei giving rise to the signal.

Many different nuclei can give MR-visible signals. Proton (^1H) is the most sensitive and abundant nucleus. Since water, and in some tissue fat, are present in large concentrations compared to metabolites, obtaining detailed information from a selected volume of interest *in vivo* can be a methodological challenge. Phosphorous (^{31}P) MR spectroscopy gives information about high-energy metabolites like ATP, ADP, phosphocreatine and phosphosugars, in addition to cell membrane metabolism (phosphomonoesters and diesters) and measurements of pH. Other nuclei like carbon (^{13}C) and fluorine (^{19}F) are easy to study *in vitro* but have been more limited *in vivo* due to low sensitivity and lack of commercially available hardware and software.

On clinical systems, ^1H is the most common nucleus for MRS. MRS provide a powerful tool for studies of biochemical processes. MRS can be related to tumor metabolism and indicate how it differs from normal metabolism [2], [3], [4], [5]. Information related to the grade and state of differentiation and response to therapy may be provided from the spectral characteristics [6], [7].

The most promising clinical potential for *in vivo* MRS is possibly monitoring of treatment response. In addition, tissue samples can be analyzed with *ex vivo* High Resolution - Magic Angle Spinning (HR-MAS) MR spectroscopy. This method reveals detailed metabolic information obtained from the tissue samples and can become a method for diagnosis of rectum cancer, and possibly also for prognosis of metastatic disease.

For the assessment of viability and aggressiveness of the tumor or its response to therapy, a method that gives insights at a cellular level would be desirable. Diffusion-weighted magnetic resonance imaging (DW-MRI) provides MR images whose signal intensity is sensitized by the random motion of free water molecules. The mobility of water molecules within a given voxel is determined by the microscopic cellular structure, i.e. the presence of barriers, such as cell membranes and macromolecules.

A prediction of tumor's response to treatment is of considerable clinical benefit. DW-MRI studies have shown the potential for assessment of early response in animal and human tumors [8], [9]. In quantitative DW-MRI, the magnetic resonance signal arises from both intracellular and extracellular compartments, and the result is given in terms of

the apparent diffusion coefficient (ADC), which is a weighted sum of these contributions [10]. The ADC is a measure of restrictions to diffusion of molecules by structures such as cell membranes, allowing inferences to be made about microstructure of the cellular environment. Thus, DW-MRI has been suggested as a tool to distinguish different tissue compartments based on their different cellular structure [11], [12], [13].

To date, the most important clinical application of DW-MRI has been detection and characterization of cerebral ischemia. In locally advanced rectal cancer, Andrzej Dzik-Jurasz et Al. showed a strong negative correlation between mean pre-treatment tumour water ADC and percentage size change of tumor after chemotherapy and chemoradiation in 14 patients [9].

Traditionally, monitoring of disease progression in experimental animal models has consisted of obtaining tissue samples at different disease stages for histological analyses. These results are 'snapshots' of disease progression originating from different animals. A preferable approach involves non-invasive technologies like MR that permit repeated non-invasive examinations over an extended period of time.

The experiments performed in this work aims to investigate whether the tumor response to radiation therapy and chemoradiation therapy can be monitored by the non-invasive methods MRS and DW-MRI. The radiation therapy includes radiation with a single fraction of 15 Gy, while the chemotherapy involves administration of Capecitabine and Oxaliplatin. The experimental tumor model is nude mice with colorectal HT29 xenografts.

To determine radiation and chemoradiation response, the tumors are excised for histological analyses. The histological examination of tissue samples (HE-stains) gives the amounts of necrosis, fibrosis and viable cells. Tumor tissue samples were also analyzed with *ex vivo* HR-MAS spectroscopy for correlation with the *in vivo* MRS data.

The report is organized as follows. Chapter 2 provides the background theory necessary to understand the experiments performed. Chapter 3 explains the methods and materials used in the experiments. This chapter also explains the different post-processing analyses that have been performed. Chapter 4 presents the results, followed by a discussion of the results in Chapter 5. The report ends with conclusions that can be drawn from the work done.

Chapter 2

Background

2.1 Cancer

Cancer is an increasing cause of death globally. More than ten millions are diagnosed with cancer worldwide and more than six million die from the disease each year [14]. In Norway, there are currently 167 000 people living with a cancer diagnosis. Only in 2003, 23 307 people were diagnosed. Each year, about 10 000 die of cancer, 6 000 of these die within one year after the time of diagnosis [1]. The types of cancer with the highest incidence are lung-, breast- and colon cancer, while highest mortality is associated with cancer of the lungs, stomach and liver [14].

Cancer is a term covering more than 100 different diseases that vary in age of onset, invasiveness, metastatic potential, response to treatment and prognosis [15]. Although tumors are different in site and origin, they have some common features. They all affect the body's basic unit, the cell, and occur when cells become abnormal and divide without control of order due to changes of the deoxyribonucleic acid, DNA. Cancer cells are less differentiated than their normal counterparts. They have the ability to invade and destroy adjacent normal tissue and to metastasize through lymphatic channels or through the blood. Cell proliferation is usually elevated in a tumor compared to normal tissue, and tumors tend to grow despite starvation of the host. Tumor cells can replicate an infinite number of times and evade apoptosis (programmed cell death) [16].

Cancer therapy involves surgery, chemotherapy and radiation therapy, often in combinations. A patient treatment plan is determined by tumor localization, tumor size, metastatic potential and lymph node status.

2.1.1 Colorectal Cancer

Colorectal cancer was the second most frequently type of cancer diagnosed in Norway in 2004, with a total of 3482 new cases [17]. Colorectal cancer can occur at any age, but is most frequent after the age of 50 years. The disease is most common in North America, northern Europe and Australasia, less common in Asia and rare in Africa. This can be understood due to the risk factors which includes physical inactivity, a diet of red meat, obesity, smoking and excess alcohol consumption, characteristic for the life style in the Western world. Other risk factors are genetic predisposition, previous history of polyps and chronic inflammation [18].

Most colorectal cancers results from malignant change in polyps that have developed in the lining of the bowel 10 - 15 years earlier. Certain kinds of polyps, called adenomatous polyps or adenomas, are types that have the largest potential to become cancerous. The adenomas undergo a malignant transformation into adenocarcinomas, which is the most common type of cancer that originates in the cells that line the rectum and large intestine. Adenocarcinomas accounts for over 90-95% of cancers originating in the rectum [18].

2.1.2 Treatment of Colorectal Cancer

Treatment of colorectal cancer consists of surgery, radiation therapy, and chemotherapy. In addition to tumor stage the treatment plan depend on the patient's age, medical history, health, and tolerance for specific medications and therapies.

Surgery

For a majority of the patients, the tumor is removed surgically. The tumor and a length of normal tissue on either side of the tumor and nearby lymph nodes are removed. The survival rate increases when surgery is performed before the cancer has metastasized. Radiation therapy and chemotherapy are often given prior to surgery to shrink the size of the tumor and thereby minimize the resection margins.

For patients with locally advanced rectal cancer, total mesorectal excision (TME) surgery are used. In TME surgery, the entire mesorectum and lymph nodes are removed. Since recurrence of rectal cancer often occurs in the lymph nodes, this technique provides improved survival [19].

Radiation Therapy

Radiation therapy is the medical use of ionizing radiation as part of cancer treatment to control malignant cells. Radiation therapy alters the genetic code in the DNA. The principle of radiation therapy can be explained using the illustration in Figure 2.1, which shows the normal life cycle of a cell in the body.

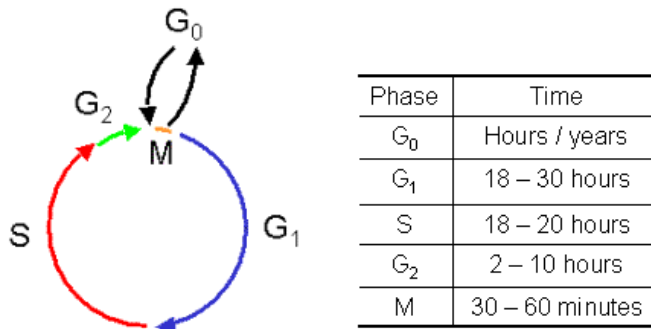


Figure 2.1: A normal cell life cycle. The cycle is made of 5 phases and is divided into: G₀ - resting stage, G₁ - RNA and protein synthesis, S - DNA synthesis, G₂ - construction of mitotic apparatus, M - mitosis. The table express how long each phase lasts.

The cell cycle consists of four phases: G₁ (first growth), S (synthesis), G₂ (second growth) and M (mitosis, cell division). These phases are characterized by the structure of the chromosomes, which contain the genetic material DNA [20]. During the cell cycle each DNA molecule is replicated into two identical daughter DNA molecules. A higher fraction of cancer cells are cycling in the cell cycle compared to normal cells. Normal cells are generally in the resting phase (G₀), continuously dividing to renew and replace cells.

The damaging effect of radiation is most pronounced on proliferating cells and radiosensitivity describes how vulnerable a cell is to radiation damage [21]. Cells in G₀ are resistant to ionizing radiation and damages to the normal cells causes side effects.

Ionizing radiation being used in radiation therapy of cancer includes:

- High-energy photons
- Electron beams
- Protons
- Neutrons

The main goal of radiation therapy is to cure or shrink the cancer either before surgery (pre-operative therapy) or after surgery to prevent recurrence of cancer (adjuvant therapy). Radiation therapy can also used as the only treatment.

Radiation therapy is a local treatment where only cells in the irradiated area are affected. In order to spare normal tissue, several angles of exposure are utilized such that the radiation beams overlap on top of each other at the tumor, providing a much larger absorbed dose in the tumor compared to the surrounding, healthy tissue.

The clinical planning of radiation therapy treatment is done by delineation of the tumor(s), draining lymph nodes and adjacent normal structures in 3 dimensions using a CT scanner and dedicated computer planning software.

Some cancers may have spread too far to be considered curable. In this situation radiation therapy is given to relieve symptoms such as pain, trouble swallowing or breathing, or bowel problems caused by advanced cancer. This radiation therapy is called palliative treatment.

Chemotherapy

Chemotherapy drugs attack proliferating cells in one or several phases of the cell cycle and can reach cancer cells that might have spread to other parts of the body. Chemotherapy is used in curation, control or palliation and there is a balance between destroying the cancer cells in order to cure the disease and minimizing undesirable side effects.

Chemotherapy may be used prior to surgery or radiation as neoadjuvant chemotherapy to shrink a large tumor, or as adjuvant chemotherapy, after surgery or radiation, in order to prevent the growth of stray cancer cells remaining in the body.

Different Types of Chemotherapy Drugs

More than 100 drugs are currently used for chemotherapy. Chemotherapy drugs are divided into several groups based on how they affect specific chemical substances within cancer cells, which cellular activities or processes the drug interfere with, and which specific phases of the cell cycle the drug affects [22].

- Alkylating Agents – These work directly on DNA to prevent the cancer cell from reproducing. These agents are not phase-specific which means that they work in all phases of the cell cycle. These drugs are active against chronic leukemias, non-Hodgkin lymphoma, Hodgkin disease, multiple myeloma, and lung, breast and ovarian cancers. Some examples of alkylating agents include busulfan, cisplatin, carboplatin, chlorambucil, cyclophosphamide, ifosfamide, dacarbazine, mechlorethamine, melphalan, and temozolomide.
- Nitrosoureas – These act in a similar way as alkylating agents. They interfere with enzymes that help repair DNA. These agents are able to travel from the blood to the brain, so they are often used to treat brain tumors. They may also be used to treat non-Hodgkin lymphomas, multiple myeloma, and malignant melanoma. Examples of nitrosoureas include carmustine and lomustine.
- Antimetabolites – These are a class of drugs that interfere with DNA and RNA growth. These agents work during the S phase and are commonly used to treat leukemias, tumors of the breast, ovary, and the gastrointestinal tract. Examples of antimetabolites include 5-fluorouracil, capecitabine, 6-mercaptopurine, methotrexate, gemcitabine, cytarabine, fludarabine, and pemetrexed.

- Anthracyclines – These interfere with enzymes involved in DNA replication and work in all phases of the cell cycle. Examples include daunorubicin, doxorubicin, epirubicin, idarubicin, and mitoxantrone.
- Topoisomerase II inhibitors – These drugs interfere with an enzyme called topoisomerase II, which is important in DNA replication. They are used to treat certain leukemias, and lung, ovarian and gastrointestinal cancers. Examples include topotecan, irinotecan, etoposide, and teniposide.
- Mitotic inhibitors – These are plant alkaloids and other compounds derived from natural products. They can stop mitosis or inhibit enzymes for making proteins needed for reproduction of the cell. These work during the M phase of the cell cycle. Examples of mitotic inhibitors include the taxanes and the vinca alkaloids.
- Corticosteroid hormones – Steroids are natural hormones and hormone-like drugs that are useful in treating some types of cancer as lymphoma, leukemias, and multiple myeloma. Examples include prednisone and dexamethasone.

2.1.3 LARC-RRP

Locally Advanced Rectal Cancer - Radiation Response Prediction (LARC-RRP) is a large study of patients with locally advanced rectal cancer, started at Radiumhospitalet-Rikshospitalet HF in September 2005. This is a group of patients with large tumors which are receiving chemotherapy and radiation therapy to reduce the size of the tumor before surgery. Some of these patients do not respond to the pre-operative treatment and the aim of the LARC-RRP study is to identify factors which can predict tumor response to radiation therapy and chemotherapy. The study includes non-invasive *in vivo* magnetic resonance spectroscopy (MRS) and diffusion weighted magnetic resonance imaging (DW-MRI) acquisitions of the tumor. Acquisitions are performed before treatment, during treatment (after 3 fractions of radiation therapy (6 Gy)) and prior to surgery.

The study includes *ex vivo* high-resolution magic angle spinning (HR-MAS) MR spectroscopy of tumor biopsies. Changes in metabolic profile of the HR-MAS MR spectra from the tumor biopsies prior to and after 6 Gy of treatment are correlated with pathological results of the biopsies. The HR-MAS MR spectra are examined to find possible prognostic factors with respect to 1- and 5-year survivals.

During the recent few years, several new chemotherapeutic and biologically targeting drugs have been available for treatment of advanced colorectal cancer. The patients in the LARC-RRP study receive two cycles with oxaliplatin/capecitabine (5-FU)-based chemotherapy and concomitant oxaliplatin/capecitabine (5-FU)-based chemotherapy during five weeks of radiation therapy (total dose of 50 Gy). A description of these two chemotherapy drugs with respect to their mechanisms are:

- Capecitabine (N^4 -pentyloxycarbonyl-5'-deoxy-5-fluorocytidine) is a novel fluoropyrimidine carbamate which is being converted to 5-fluorouracil (5-FU) by 3 sequential steps of enzyme reactions. In humans, it is sequentially converted first to 5'-deoxy-5-fluorocytidine by carboxylesterase located in the liver, then to 5'-deoxy-5-fluoruridine by cytidine deaminase and finally to 5-FU by thymidine phosphorylase (dThdPhase) with high activity in many types of tumors [23].
- Oxaliplatin is a synthesized diamminocyclohexane platinum compound which causes DNA-adduct formation, resulting in damage such as intrastrand cross-links covalently binding the platinum compounds to guanine radicals, DNA interstrand cross-links, DNA-protein cross-links and DNA strand breaks. Oxaliplatin has demonstrated enhanced activity in combination with other drugs, such as 5-FU, both in preclinical and clinical studies in addition to significant single-agent activity in advanced colorectal cancer [24], [25].

The LARC-RRP study is thoroughly described in a Clinical Study Protocol and an associated Experimental Study Protocol recently approved by public and institutional authorities. One hundred patients is expected to be included over a period of about 3 years.

The two animal experiments performed in this work are connected to the LARC-RRP study. Mice with implanted tumors from human rectal cancer xenografts are being used in both experiments. The experiments includes *in vivo* MRS and diffusion tensor MRI (DTI) in order to see if tumor treatment response can be monitored non-invasively. The mouse tumors are surgically removed at different times before and after treatment for HR-MAS spectroscopy and HE-staining. HE-staining yields results about the presence of viable tumor cells, fibrosis and necrosis. In the first experiment the tumors are only irradiated with a single fraction of 15 Gy. In the second experiment the mice receives both radiation therapy and the same chemotherapy drugs as the patients in the LARC-RRP study, Oxaliplatin and Capecitabine (5-FU).

2.2 Biochemistry of the Cell

2.2.1 Metabolism in Human Cells

Metabolism is the physiological processes in living organisms and cells that takes place in order to utilize nutritive substance, mainly carbohydrates, proteins and fat. These substances are used in the development of tissue and energy (anabolism), in addition to the break-down of waste products (catabolism) [15].

Metabolism consists of several metabolic pathways. Most cells contain the enzymes required for the metabolic pathways, but the level of expression is differently regulated in different tissues. Metabolites are the intermediates and products of metabolism. An

overall figure of human metabolism is shown in Figure 2.2

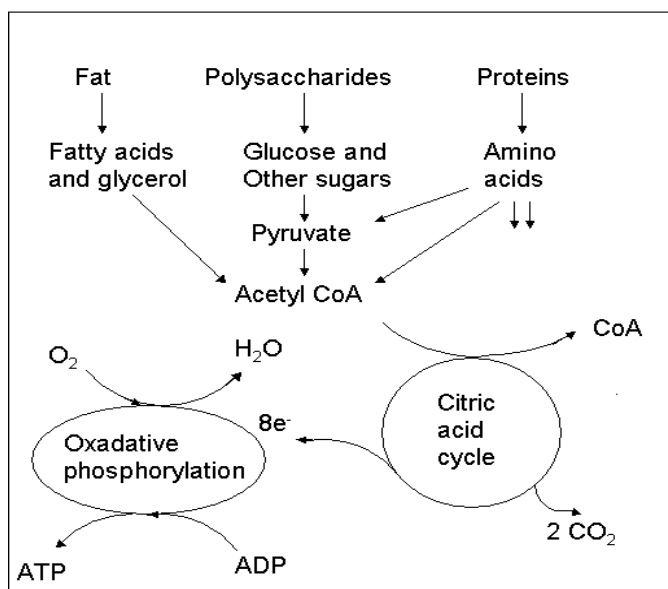
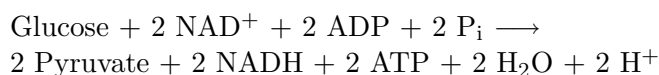


Figure 2.2: The figure shows a simplified, schematic view of the constituents in the metabolism of nutrients in living cells [20].

Glycolysis

Glycolysis is the process that converts glucose into pyruvate. Glycolysis occurs in the cell cytoplasm and serves two fundamental functions: (1) the generation of high-energy molecules, adenosine triphosphate, ATP, and reduced nicotinamide adenine dinucleotide, NADH, and (2) the production of a variety of six- or three-carbon intermediate metabolites [20]. Figure 2.3 gives an illustration of the glycolysis.

The overall reaction of glycolysis is:



In the first half of glycolysis (the preparatory phase) energy are consumed for converting glucose into three-carbon sugar phosphates. In the second half of glycolysis (the pay-off phase) the energy-rich molecules ATP and NADH are achieved.

The flux through the glycolytic pathway is adjusted with respect to conditions both inside and outside the cell and the flux rate is regulated to meet two major cellular needs: (1) the production of ATP, and (2) the supply of building blocks for biosynthetic reactions. In glycolysis, the reactions catalyzed by hexokinase, phosphofructokinase, and pyruvate kinase are irreversible. These enzymes are sites of control in the glycolysis [15].

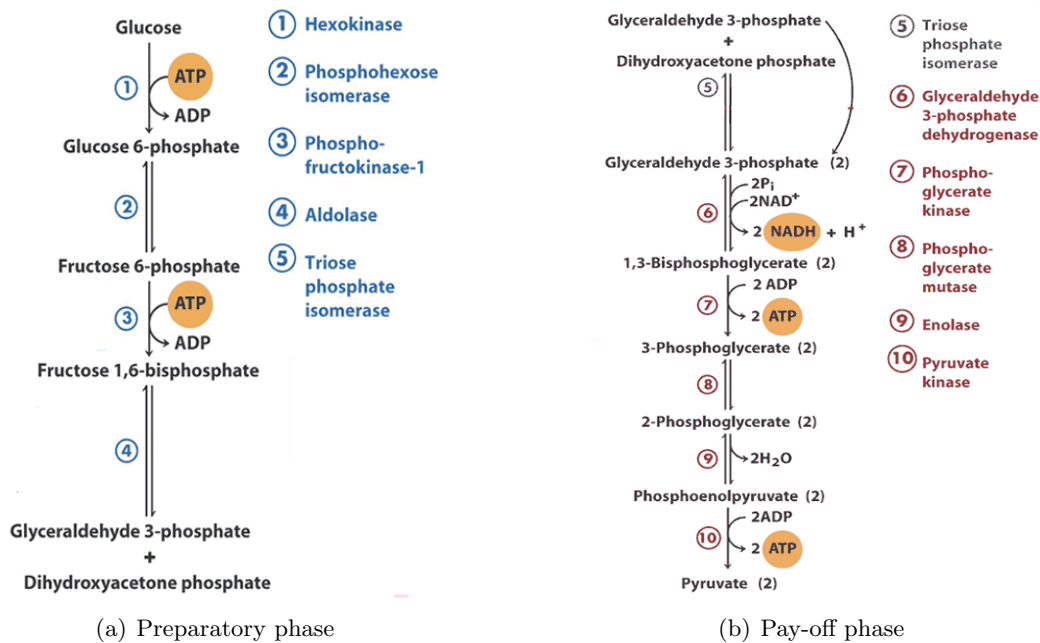


Figure 2.3: The glycolysis pathway divided into two parts. a) The preparatory phase where glucose is converted into three-carbon sugar phosphates. b) The pay-off phase with generation of the high-energy molecules ATP and NADH. The end product is pyruvate [20].

Human metabolism is primarily aerobic, but under hypoxic conditions pyruvate is converted to lactate in the fermentation. Fermentation maintains the metabolic flux through the glycolysis with regeneration of NAD^+ . Fermentation is essential in normal cellular function as it is the only source of ATP in anaerobic or hypoxic conditions.

The citric acid cycle

The citric acid cycle is a series of chemical reactions in all living cells that utilize oxygen as part of cellular respiration. It is a metabolic pathway in the breakdown of carbohydrates, fats and proteins into carbon dioxide and water. The citric acid cycle is the second of three metabolic pathways in fuel molecule catabolism and ATP production, the first being glycolysis and the last being oxidative phosphorylation [15].

The end product of the glycolysis is pyruvate. Pyruvate is transported into the cell mitochondria, where it is oxidatively decarboxylated and connected to coenzyme A, resulting in acetyl CoA. Acetyl CoA is the main input to the citric acid cycle by a reaction of the acetyl group with oxaloacetate to form citric acid [20]. The citric acid cycle is illustrated in Figure 2.4.

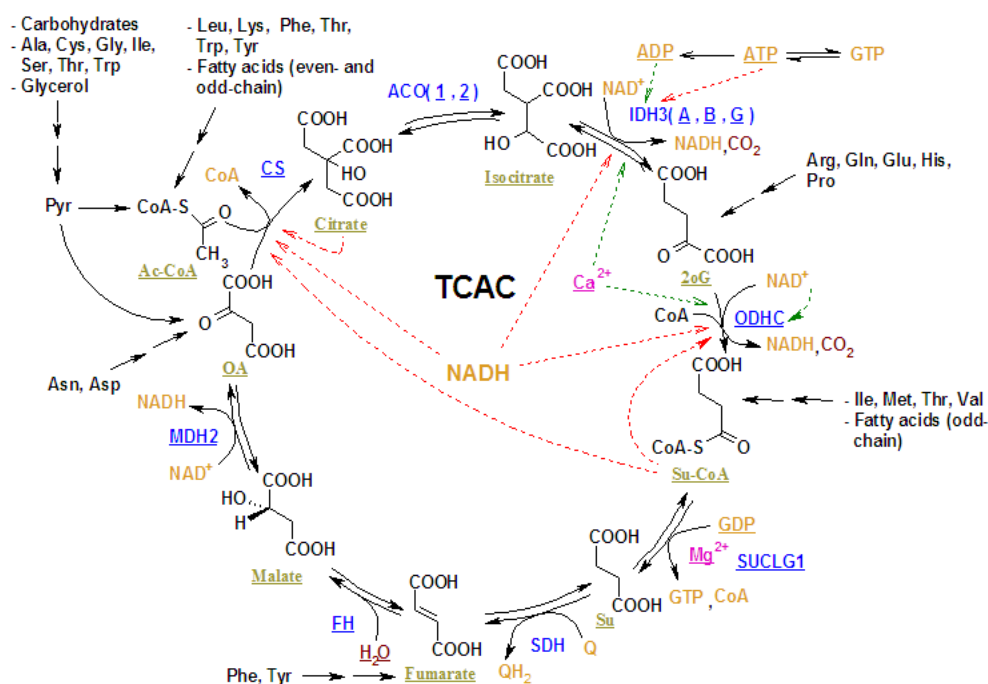
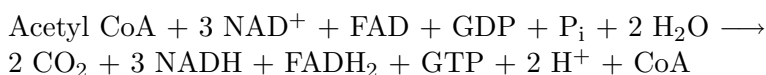


Figure 2.4: The reactions of the tricarboxylic acid cycle (TCAC) in a living cell. The color scheme is as follows: Blue - enzymes, orange - coenzymes, brown - substrate names, pink - metal ions, dark red - inorganic molecules, red - inhibition, green - stimulation [26].

The net reaction of the citric acid cycle is:



The citric acid cycle generates CO_2 , and reduces nicotinamide adenine dinucleotide, NAD, and flavine adenine dinucleotide, FAD, to NADH and FADH_2 . The electron transfer from NADH to FADH_2 release energy providing transport of the hydrogen ions out of the mitochondria. The resulting electrochemical proton gradient drives most of the cells synthesis of ATP [20].

The biosynthesis of macromolecules includes proteins, nucleotides and membrane constituents. Amino acids are precursors of proteins, nucleotides and polysaccharides. Essential properties of living cells depend upon proteins, in oxygen- and membrane transport of ions and molecules. The proteins are broken down by protease enzymes and amino acids in the protein catabolism. The amino acids are the cells source of energy. In fat catabolism, triglycerides are hydrolyzed and broken down into fatty acids and glycerol.

The citric acid cycle is followed by oxidative phosphorylation. This process extracts the energy from NADH and FADH_2 , recreating NAD^+ and FAD to continue the cycle.

2.2.2 Metabolism of Tumors

Cell membranes are composed of a double layer of lipid molecules, embedded with membrane proteins. The most important types of membrane lipids are phospholipids, sphingolipids and cholesterol. These components are synthesised by the cells themselves. The most common hydrophilic ends in phosphoglycerides are phosphoethanolamine (PE), phosphocholine (PC), phosphoserine and phosphoinositol.

Diseased cells have altered metabolism. For example, cancer cells have high rates of metabolism and low levels of oxygen. The hypermetabolic state of cancer cells includes the shift towards the breakdown of glucose in the absence of oxygen. In this process, called anaerobic glycolysis, the majority of glucose is chemically converted into lactic acid. Anaerobic glycolysis in cancer cells is inefficient at generating energy in the form of ATP. Therefore, a cancer cell must consume high levels of glucose to produce enough ATP to support function, survival, and replication of the cell [4].

MR spectroscopic studies of different types of cancer have focused on the alteration in the phospholipid metabolism [5]. Studies of various malignant cell lines have proven increased metabolite levels of choline in tumors compared to normal tissue. *Ex vivo* studies have shown that this is thought to be due to the biosynthesis and catabolism of phospholipids [27], [28]. In addition, it has been shown that phospholipid metabolism is changed when the patient receives successful treatment.

By examining spectra obtained with MR spectroscopy it is possible to compare the relative amounts of each metabolite to determine a disease process. For example, alteration in the following are indicators for tumors [29], [6], [30]:

- N-acetylaspartate, NAA, drop indicates tumor cell invasion. Its relative levels are a marker of neuronal integrity and functional status. Brain diseases (schizophrenia, stroke, certain tumors, multiple sclerosis) can be characterized by the regional alteration in NAA levels.
- Choline elevation indicates tumor growth. Choline is involved in pathways of phospholipid synthesis and degradation, thereby reflecting membrane synthesis and degradation.
- Lactate changes indicates anaerobic conditions, and is a metabolically important marker of tissue ischemia and hypoxia, since its concentration increases markedly in aerobic tissues like brain and muscle which are deprived of oxygen for short periods of time.
- Lipid elevation indicates tumor necrosis.
- Creatine drop indicates malignant tumors with high metabolic activity and depleted energy stores.

2.3 Magnetic Resonance Imaging

In 1946 Bloch and Purcell [31] made the first magnetic resonance (MR) experiments using solids and liquids. They observed that the frequency of the MR signal was dependent on the specific chemical environment of the nuclei, called the chemical shift. In 1973 the first MR images were acquired when Lauterbur discovered that spatial localization of the MR signal could be achieved by using magnetic field gradients [32]. The first human images were obtained in 1977.

Development of computers and dedicated hardware made it possible to design MR scanners for clinical use, and during the 1980s the first magnetic resonance scanners were installed at Norwegian hospitals. The new scanners brought expectations of faster and more reliable diagnostics and the foundation of choosing the correct medical treatment increased. Magnetic resonance scanners have in some areas replaced the well known X-ray scanners, e.g. in identification of malignant tumors.

The advantage of MRI is its high contrast resolution, and the possibility of acquiring cross-sections in several directions. So far, no proven side effects are discovered by the use of MRI, either during scanning nor afterwards. As with computer tomography, CT and conventional X-ray, MRI is a way to depict the inner anatomy of the human body.

2.3.1 Principles of Magnetic Resonance

Nuclei with uneven numbers of protons and neutrons possess magnetic angular momentum or spin. This characterizes numerous nuclei, for example ^{31}P , ^1H and ^{13}C . The spinning nuclei carry electric charges inducing a magnetic moment comparable to a tiny magnetic dipole. When an external magnetic field, B_0 , is applied, the magnetic dipoles will line up parallel or anti-parallel to the magnetic field. For ^1H with a spin quantum number of $\frac{1}{2}$ this means that the nucleus has two energy states corresponding to the spin being directed parallel or anti-parallel to the magnetic field. When there is an odd number of protons in the nucleus as in the ^1H , there will always be an unequal number of spins in the two directions, resulting in a net magnetic field, or a magnetic dipole moment [29].

All nuclei with an odd number of protons can be used for imaging in MR. The reason for using hydrogen is because of its abundance. The human body consists of 63 % hydrogen atoms and hydrogen is found in both water (H_2O) and fat ($-\text{CH}_2-$). If nothing else is mentioned, the rest of the text will concern the hydrogen atom, i.e. the proton.

The magnetic moment of the nuclei will precess around the axis of B_0 at a frequency given by the Larmour equation:

$$\omega = \gamma B_0 \tag{2.1}$$

where ω is the angular precessional frequency of the proton, γ the gyromagnetic ratio and B_0 the strength of the external magnetic field. For the proton, the gyromagnetic ratio is 42.6 MHz/Tesla. That means, in a 1.5 Tesla MR system, the proton precessional frequency is $(42.6)(1.5) = 63.9$ MHz.

The field B_0 is the magnetic induction field or magnetic flux density. This is the net magnetic field effect caused by an external magnetic field. The field H is the magnetic field intensity. These two magnetic fields are related by the following equation [33]:

$$B_0 = \mu H \quad (2.2)$$

where μ is the magnetic permeability. The magnetic susceptibility, χ , of a substance is a measure of how magnetized the substance gets, and is defined as the ratio of the induced magnetic field, M , to the applied magnetic field H :

$$M = \chi H \quad (2.3)$$

Excitation

Inside the MR scanner, the protons with a spin parallel to B_0 will be in excess giving rise to a magnetic dipole moment in the z-direction, i.e. the direction of the external magnetic field, M_z , is positive. The net component of the magnetic dipoles in the xy-plane, M_{xy} , is zero. The signal which is detected in MR imaging is the varying magnetic flux in the xy-plane. The net magnetic moment in the z-direction has to be rotated or 'flipped' into the xy-plane to achieve a detectable signal. This flipping is called excitation.

The excitation of the protons is achieved by applying another magnetic field, B_1 , in the xy-plane. B_1 is a linear polarized oscillating magnetic field with an oscillation frequency equal to the Larmor frequency and the magnetic field has to rotate with this frequency to influence the protons. A linear polarized oscillating field can be regarded as a superpositioning of two circular polarized fields rotating with the frequencies ω and $-\omega$. Only the field rotating with ω will influence the protons. Of this reason, the amplitude of the applied linear polarized field has to be twice the amplitude of the circular polarized field which influence the protons [32].

The B_1 field is applied a time τ and is called the RF pulse or excitation pulse. During the time τ , the magnetic field is flipped an angle, θ (Figure 2.5), given by Equation 2.4 [31].

$$\theta = \gamma B_1 \tau \quad (2.4)$$

where γ is the gyromagnetic ratio, B_1 is the applied magnetic field and τ the time the field is applied. If the B_1 field is applied a time τ_{90} , the magnetization will be flipped 90° . This excitation pulse is called a 90° -pulse. If the B_1 field is applied a time τ_{180} , the pulse is called a 180° -pulse due to the 180° flipping of the magnetic vector. The net magnetization will rotate both around the z-axis and the axis of the linear polarized oscillating excitation field while the excitation pulse is applied.

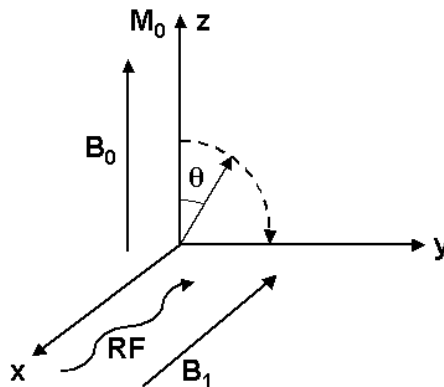


Figure 2.5: A time after the application of the RF pulse, the magnetization vector is 'flipped' towards the xy -plane forming an angle θ with the z axis. The figure is based on a figure from [31].

Rotating Frame of Reference

The stationary frame of reference, x, y, z , is called the laboratory system. A new frame, x^R, y^R, z^R is defined. It rotates around the z -axis with the Larmor frequency and is called the rotating frame of reference. In the rotating laboratory system, the magnetization vector will be static, provided the RF pulse is applied along the x axis. During excitation, the net magnetization will only have a precession around the y^R in the rotating frame [31].

Relaxation

After excitation, the magnetic dipole moment will try to re-establish equilibrium. This is called relaxation. The process of relaxation is divided into a longitudinal and transverse relaxation and is described of the time constants T_1 and T_2 respectively.

T_1 Relaxation

Longitudinal relaxation describes the relaxation of the net magnetization z -component, M_z . Prior to the excitation, M_z has a constant equilibrium value M_0 . After a 90° -pulse, the net magnetization will be rotated into the x^R, y^R -plane and M_z will be zero. The relaxation of M_z is described in Equation 2.5 and is illustrated in Figure 2.6.

$$M_z(t) = M_0(1 - e^{-\frac{t}{T_1}}) \quad (2.5)$$

where T_1 is the time it takes before $M_z = M_0(1 - e^{-1}) \approx 0.63M_0$ [31].

T_1 depends on the interactions between the magnetic dipole moments and the medium the protons are situated in, the lattice. Longitudinal relaxation is therefore also called spin-lattice relaxation time. T_1 relaxation occurs when protons excited to a higher state of energy, spin-up, returns to the lower state, spin-down. The transition between the energy states is stimulated of fluctuating magnetic field in the medium. The fluctuating magnetic fields in the medium originate from molecular movements, and can stimulate

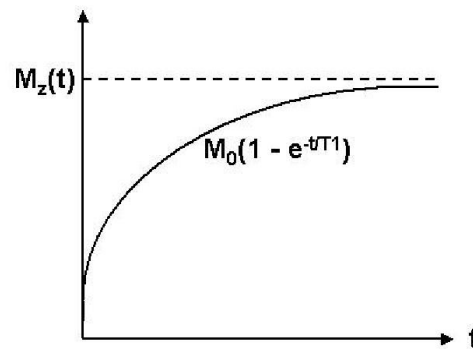


Figure 2.6: The recovery of longitudinal magnetization.

transition between the energy states if the fluctuation has frequency components equal to the Larmor frequency. The energy states at deexcitation leads to an increased thermal energy in the medium. The T_1 constant is specific for the tissue. A short T_1 indicates that the medium containing the protons, is suitable for the energy exchange. Examples of medium with short T_1 is fat and proteinaceous fluid, while water has long T_1 . Solid tissue has intermediate T_1 .

T_2 Relaxation

Transverse relaxation is the relaxation of the net magnetization xy-component, M_{xy} . Prior to the excitation, M_{xy} is zero. The 90° -pulse flips the net magnetization into the x^R, y^R -plane. The magnetization xy-component gets a positive initial value, M_{xy0} . Equation 2.6 gives the relaxation of M_{xy} , and the relaxation is illustrated in Figure 2.7.

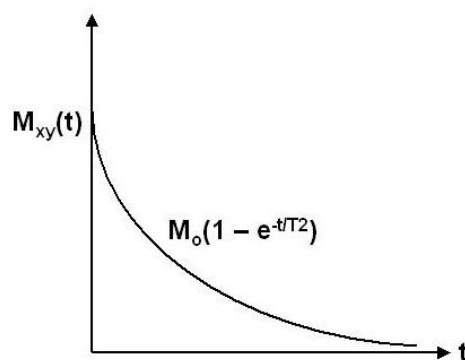


Figure 2.7: The decay of transverse magnetization.

$$M_{xy}(t) = M_0 e^{-\frac{t}{T_2}} \quad (2.6)$$

where T_2 is the time it takes to reduce M_{xy} to $M_{xy0}e^{-1} \approx 0.37M_{xy0}$ [31].

This relaxation is due to the fact that the magnetic dipole of a proton will influence the magnetic field experienced by other magnetic dipoles. This is the reason why the T_2 relaxation is also called spin-spin relaxation. The result is that the Larmor frequencies and consequently the precession speeds of each dipole become slightly different. Due to different precession speeds, the magnetic dipoles will be out of phase and the signal will decay.

In an ideal situation, the static magnetic field, B_0 , will be perfectly uniform. This is not the case, and the inhomogeneities of B_0 produce a contribution to the transversal relaxation. The total effect of spin-spin relaxation and inhomogeneities in the static magnetic field is called T_2^* relaxation and is described by Equation 2.7.

$$\frac{1}{T_2^*} = \frac{1}{T_2} + \gamma \frac{\Delta B_0}{2} \quad (2.7)$$

where ΔB_0 is the inhomogeneities in the magnetic field [31]. The effect of the inhomogeneities in the magnetic field is reversible and can be eliminated in a spin-echo sequence.

2.3.2 Spin Echo

A pulse sequence is a series of RF pulses. The spin echo sequence has the advantage of eliminating inhomogeneities in the static magnetic field. The sequence starts by exciting a 90° -pulse resulting in a net magnetic dipole moment in the xy-direction. These dipole moments will after a time be out of phase because of the different precession speeds, as described in section 2.3.1.

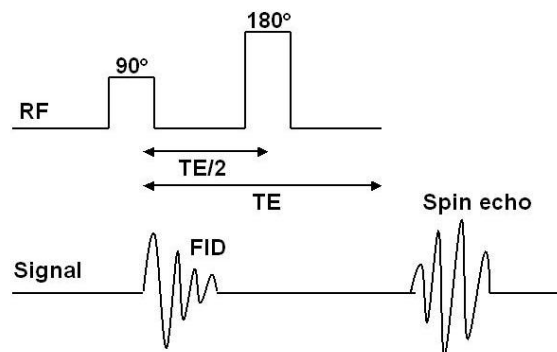


Figure 2.8: The figure shows the spin echo pulse sequence in a timing diagram (upper), and the detected signal for the spin echo pulse sequence (lower).

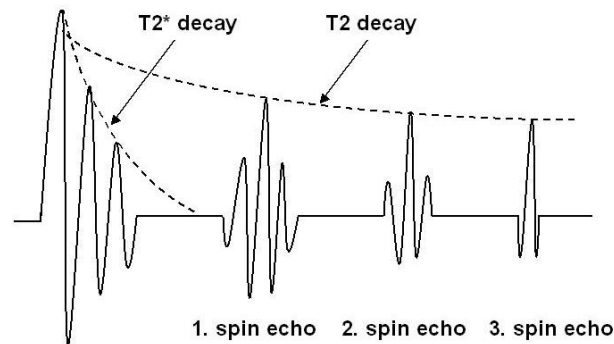


Figure 2.9: The figure shows the echotrain which is detected at a spin echo pulse sequence.

After at time $\frac{TE}{2}$, a 180° -pulse is applied. This causes the magnetic dipole moments which were slowed down due to the lower precession speed to be in front of the magnetic dipole moments with a higher precession speed. At the time TE , the echo time, the dipole moments will be in phase again and a new signal can be registered. This signal is called the echo. An illustration of the spin echo sequence are shown in Figure 2.8. The echo will decrease the same way as the signal after the 90° -pulse, but the maximum signal will be a little lower because the spin-spin (T_2) is not reversible. The 180° pulse are repeated to detect a train of echoes, with the maximum signal declining with the T_2 relaxation constant, as shown in Figure 2.9.

Fast Spin Echo

Fast spin echo, FSE, is a spin echo pulse sequence including a series of rapidly applied 180° rephasing pulses and multiple echoes, changing the phase encoding gradient for each echo. Fast spin echo sequences have replaced conventional T_2 weighted spin echo sequences for most clinical applications. Fast spin echo allows reduced acquisition times, for example an echo train length of 10 will result in a scan time of one tenth of the time. The use of large echo train lengths with short TE results in blurring and loss of contrast. For this reason, T_2 weighted imaging profits most from this technique.

2.3.3 Image Reconstruction

After excitation, the spinning dipoles will relax back to equilibrium. This relaxation can be detected with external coils. The phenomenon is called free induction decay, FID. The detected signal is a sum of contributions from all the excited magnetic dipole moments in the sample volume. To achieve an image with spatial resolution, the contributions from smaller volumes need to be separated.

A magnetic field gradient is a variation of the magnetic field with respect to position which results in a linear dependence of the magnetic field. Gradients in the x , y and z

directions are required to obtain spatial information:

- The slice select gradient, G_z
- The frequency-encoding gradient, G_x
- The phase-encoding gradient, G_y

The Slice Select Gradient

In addition to the external magnetic field, B_0 , a linear magnetic gradient in the z-direction, G_z , is applied. Since the Larmor frequency is proportional to the strength of the magnetic field, the Larmor frequency will have a z-dependence given by [33]

$$\omega = -\gamma(B_0 + zG_z) \quad (2.8)$$

With a z-dependent Larmor frequency, one can excite a thin slice by letting B_1 contain a narrow band of frequencies around the Larmor frequency, corresponding to the z-values of the slice. The magnetic dipole moments outside the slice will not be excited as their Larmor frequencies differs from the frequency of the exciting magnetic field, B_1 .

Frequency and Phase Encoding

Gradients in the x- and y-directions gives the possibility to achieve 2-dimensional MR images. After excitation of a particular slice, the gradient in the y-direction, G_y , is applied. The magnetic dipoles will rotate with a frequency determined by their y position. After a time, G_y is turned off, resulting in the magnetic dipoles to precess with the same frequency. Due to varying precession speed while G_y is on, the magnetic dipole moments will have different phase dependent on the y position. This technique is called phase encoding, and the phase of the individual y positions is given of Equation 2.9 [33].

$$\omega_y t_y = \gamma G_y t_y y = k_y y \quad (2.9)$$

where t_y is the time the gradient G_y is applied and $k_y = \gamma G_y t_y$ has the unit radians per meter and represents spatial frequency.

The gradient G_x turns on while the G_y gradient is active and during detection of the signal. This is called the read-out gradient. The magnetic dipole moments will during detection of the signal precess with a frequency dependent on the x position. This is described by Equation 2.10 [33].

$$\omega_x t_x = \gamma G_x t_x x = k_x x \quad (2.10)$$

where t_x is the time the gradient G_x is applied and $k_x = \gamma G_x t_x$ in units of radians per meter represents spatial frequency.

To be able to image the entire slice, this sequence is repeated with a new G_y in every repetition, resulting in a set of FIDs with different G_y . To make an image with $N_x \times N_y$

points, N_x points are needed in every FID and the sequence must be repeated N_y times.

The signal component detected from each sample volume will be complex. Accordingly, the total signal is a sum of contributions from all sample volumes. Assuming the volumes to be small, the sum is written as an integral, see Equation 2.11.

$$S(k_x, k_y) = C \int_{-\infty}^{\infty} \int_{-\infty}^{\infty} M(x, y) e^{i(k_x x + k_y y)} dx dy \quad (2.11)$$

where C is a constant and $M(x, y)$ an instant image of the net magnetic dipole moment. This is an inverse Fourier transformation. The size of the net magnetic dipole moment can be found by use of the Fourier transformation of the detected signal [33]:

$$M(x, y) = C \int_{-\infty}^{\infty} \int_{-\infty}^{\infty} S(k_x, k_y) e^{-i(k_x x + k_y y)} dx dy \quad (2.12)$$

2.3.4 Imaging Coils

A coil is an electrical device composed of a single or multiple loops of wire. The coil can either generate a magnetic field, a gradient coil, or detect an oscillating magnetic field as an electrical current induced in the wire, a RF coil [31].

Gradient coils include the imaging gradient coils and the shim coil. The imaging gradient coil cause a perturbation in the magnetic field homogeneity which results in spatial encoding. Shim coils are used to create a more uniform external magnetic field, B_0 .

Transmit and/or receive RF coils include the single phase or quadrature coils, the surface or volume coils, called solenoid, and the phased array coils. The quadrature coils have two receivers which are 90° to one another in order to distinguish between the real- and imaginary components of the received signal. The solenoid coils can be wrapped around the patient to increase the SNR. Phased array coils contain multiple small surface coils. These coils allows faster scanning with finer details and increased SNR.

Coil for Imaging of Small Animals

MRI of small animals in clinical whole-body MRI scanners is technically demanding because high spatial resolution images of thin tissue sections, high SNR and high B_1 field homogeneity is needed. Modern scanners usually provide sufficient gradient strength for this purpose, but the sensitivity of conventional coil systems is insufficient. To be able to image small animals, an open gap transmit-receive MR coil for imaging in a clinical whole-body 1.5 T MR scanner was designed by Bjørn Høvik and Therese Seierstad at Rikshospitalet-Radiumhospitalet HF [34]. The coil is shown in Figure 2.10.

The coil consists of two tube-shaped inductively coupled resonance circuits where the primary circuit partly encapsulates the imaging (secondary) circuit in order to reduce the

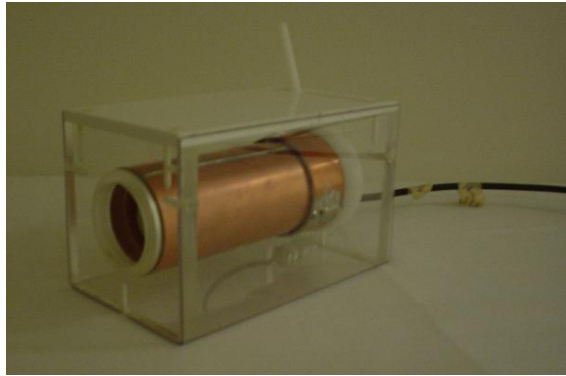


Figure 2.10: The transmit-recvie MR coil for imaging of small animals in a clinical whole-body 1.5 T MR scanner.

capacitive coupling between the object and the detection of RF pulses. The RF field is generated by inductive coupling between the two circuits.

The primary coil is coupled in parallel with a capacitor to the MR scanner RF system via a 50Ω coaxial cable. A handle is connected to the coil to enable manual tuning of the impedance and phase of the loaded coil in order to match the MR system before acquisition of data. The coil is tuned to a frequency close to the expected Larmor frequency of the protons (63.89 MHz), whose resonance signal is being detected. The tuning creates a higher output signal for a given input signal and minimizes losses due to external sources with other frequencies.

The coil provides examinations with nearly homogeneous sensitivity in the entire body at a spatial resolution of 1-2 mm. For all MR experiments with the coil, a 30 dB attenuator has to be connected to the transmit line of the MR scanner in order to reduce the excitation signal. There is no need for hardware modifications of the MR scanner.

2.4 Magnetic Resonance Spectroscopy

2.4.1 Principles of MR Spectroscopy

As in MRI, MR spectroscopy (MRS) utilizes the magnetic properties of nuclei with nuclear spin $I \neq 0$. The nuclear spins will be oriented in $2I+1$ different energy levels according to equilibrium processes. Transmissions between different energy states occurs when RF pulses are applied to the system. The excited nuclei returns to equilibrium via longitudinal (T_1) and transversal (T_2) relaxation processes [30]. This time domain signal is a superposition of the signal decays from all individual spins in the selected volume of interest (VOI). A complex Fourier transform of the time domain signal gives the frequency

spectrum, or MR spectra. The peaks in the spectra corresponds to the molecular environment of the nuclei, in addition to the physical, chemical and biological properties of the studied object. The aim of *in vivo* MR spectroscopy is to obtain a spectrum that arises exclusively from the voxel of interest, VOI, with the best achievable sensitivity and with minimum contribution from other regions [35].

Spectroscopy data is represented as a signal on a frequency or parts per million (ppm) scale. The chemical shift is a convenient conversion of frequency to ppm, converting a MHz scale to a comparable ppm-scale and making results obtained on magnets of different field strengths directly interchangeable. This is done by referring the peak position to a known reference compound, see Equation 2.13. The spectra have chemical shift along the horizontal axis and signal amplitude along the vertical axis. The chemical shift and peak multiplicity of a nucleus depend on the neighboring atoms while the integral under the curve is proportional to the concentration of nuclei in the specie being analyzed. [36].

$$\delta = \frac{\nu_{signal} - \nu_{reference}}{\nu_{reference}} \cdot 10^6 \quad (2.13)$$

MR spectroscopy has been applied on *ex vivo* cells, animal models and tissue extracts for over 20 years [30] and for a few years on patients. The method has shown to be useful in the understanding of biological processes. MR spectroscopy can be used as a unique mean for probing the biochemistry of living systems [35]. Spectroscopic cancer studies typically probe inherent tumor metabolism including the tumor metabolism's alteration by therapy. In the last years, correlation of *in vivo* MR spectra to patient diagnosis have been established.

The two most common methods to locate an *in vivo* spectrum is single voxel techniques and multi-voxel techniques. Both use an image for guidance [29]:

- Single voxel techniques. They use three intersecting slices to locate a single voxel from which to measure the spectrum. There are two main types of single voxel techniques: (1) Stimulated echo acquisition mode (STEAM) and (2) Point resolved spectroscopy spin echo (PRESS).
- Multi-voxel techniques. They are more time efficient as they acquire multiple voxels by encoding in k-space as in conventional imaging.

2.4.2 Splitting

All nuclei are surrounded by an electron cloud. These circulating electrons generate a small magnetic field and shield the nuclei from the large, static magnetic field. Differences in the electron cloud density makes nuclei experience different field strengths, resulting in different resonance frequencies. Therefore the peaks will appear at different values

along the chemical shift scale. Some atoms lack electrons and will pull on the electrons belonging to neighbouring atoms. This pulling leads to a thinner electron cloud and reduced shielding. A nucleus close to such an atom will experience a stronger magnetic field than one further away. A stronger magnetic field implies a higher resonance frequency [30].

Peak multiplicity appear due to the distribution of neighboring spins in different energy states. Every hydrogen in a molecule spins, and moving charged particles generate their own magnetic field. These fields have magnetic moments which interacts with the magnetic moment of the external magnetic field. This results in the splitting of the resonance signal. The number of times the signal split are found by adding up all the neighbouring protons that are non-equivalent to the protons whose resonance signal is being generated.

Figure 2.11 shows a model of the ethanol molecule ($\text{OH-CH}_2\text{-CH}_3$). The 6 protons give rise to 3 peaks. The three protons on the carbon atom will not be in restricted positions, but moving freely around the bounding. In average they experience the same magnetic environment and they appear at the same chemical shift. The same is true for the two protons on the neighboring carbon. The ethanol molecule will give rise to three peaks in the proton spectrum. The hydroxyl proton is not always observed due to exchange with solvent atoms.

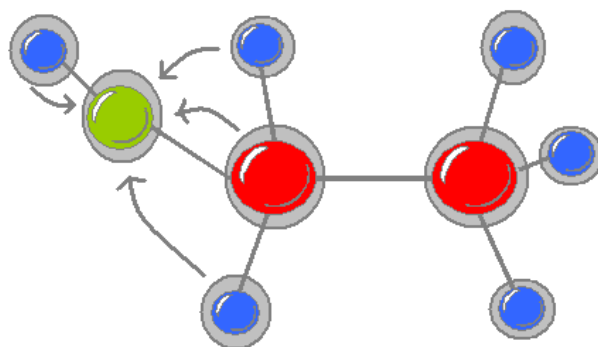


Figure 2.11: A model of the ethanol molecule. Protons are blue, carbons are red and oxygen is green. The electron cloud is grey. Oxygen lacks electrons and pulls on the electrons belonging to neighboring atoms, yielding a thinner electron cloud and reduced shielding. A nucleus close to oxygen will therefore experience a slightly stronger magnetic field than further away.

Peak multiplicity appear because of the distribution of neighboring spins in different energy states (α and β). A sample of ethanol contains a large number of molecules, and the nuclei are distributed in α or β state in accordance to the Boltzman distribution. The two protons on the carbon have half their population in α and the other half in β state, almost equally distributed. This results in that one fourth of the three protons on the outermost carbon see the $\alpha\alpha$ -state, two fourth see the $\alpha\beta$ -state and one fourth see the $\beta\beta$ -state. The

result is a triplet, shown in Figure 2.12.

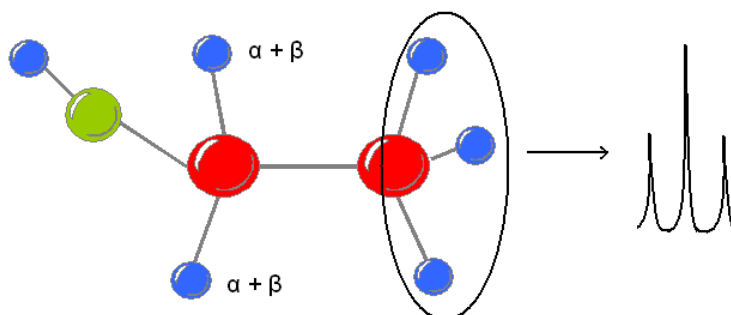


Figure 2.12: Peak multiplicity occurs when neighbouring spins are in different energy states (α and β). The example shows the ethanol molecule.

The signal split in $n+1$ ways where n is the number of non-equivalent protons. This results in doublets, triplets, quartets etc. Neighboring protons that are equivalent to the protons whose signal is being generated, will not split the signal. This results in only one signal, a singlet, since the protons are equivalent.

Additional features characterize spectra, of which the splitting of resonance lines into several smaller lines is the most pronounced. This phenomenon originates from the fact that nuclei with magnetic moments influence each other through space (dipolar coupling) or through chemical bonds (scalar coupling). In a liquid the dipolar interactions normally average out to zero due to rapid tumbling, so that no net interaction between the nuclei remains. Interactions between tissue bounds, i.e. interaction of the nuclear magnetic moment with the much larger electronic magnetic moment of the electrons in the bonds, do not average to zero. This interaction is called spin-spin, or J, coupling. The J coupling constant is independent of the applied external magnetic field, since it is based on the fundamental principle of spin-spin pairing. The coupling constant is therefore expressed in Hertz (Hz). The J coupling constants of ^1H - ^1H is 1-15 Hz. Because the chemical shift and J coupling constant have a different dependency on the amplitude of the main magnetic field B_0 , the appearance of spectra at different B_0 will also change.

The splitting pattern in spectroscopy spectra of coupled nuclei can be described by chemically equivalent and magnetically equivalent nuclei. For equivalent nuclei, all physical and chemical properties are the same. Two nuclei with the same chemical shift can be coupled to a third magnetic nucleus having a different chemical shift. When the J coupling constant of the two nuclei with the third nucleus is different, the nuclei are chemically equivalent but not magnetically equivalent. For magnetically equivalent nuclei, the J coupling constant with a shared third nucleus must be identical.

Magnetically equivalent nuclei do not produce an observable splitting of each others reso-

nance lines. This is because quantum mechanical selection rules prohibit the appropriate transitions. When there are more than two magnetic nuclei in a molecule, coupling may occur between each pair of nuclei, resulting in complex splitting patterns. The presence of magnetically equivalent nuclei in a group of interacting spins simplifies the appearance of the spectrum. The splitting of pattern of spin in a spin system is given by a binomial distribution in which the lines are separated by the J coupling constant [30].

2.4.3 Multi-Dimensional Spectroscopy and CSI

Multi-dimensional spectroscopy can be achieved by separating the various characteristics of resonances along orthogonal axes. Two dimensional, or correlation spectroscopy, provides information about homonuclear coupling connectivities for the identification of scalar coupled spin systems. 2D spectroscopy can be used to observe, identify and study coupled resonances unambiguously, which are unobservable due to spectral overlap in regular 1D spectra. The idea of 2D experiments is to generate a second frequency axis by introducing an evolution delay (and at least one additional pulse) into a pulse sequence, during which the transverse magnetization precesses at a different frequency from that during signal acquisition [30].

Chemical shift imaging (CSI) is an imaging modality where metabolite maps of the occurrence of selected metabolites are obtained. CSI is most useful when the exact localization of an abnormality is unknown. CSI use phase encoding in order to obtain spectra from a matrix of voxels.

2.5 High Resolution - Magic Angle Spinning, HR-MAS

2.5.1 Principles of HR-MAS MR Spectroscopy

Nuclear magnetic resonance (NMR) spectroscopy of tissue give broad lines in the spectra. Andrew et al. and Lowe first described the narrowing of MR lines when solids where spun at a magic angle [37].

A characteristic feature of NMR is that the spectra for solids are much broader than those for liquids. The origin of this difference in behaviour lies in the static anisotropic interactions to which the nuclei in solids are subject. The anisotropic nuclear interactions which are of interest in solid state NMR spectroscopy are:

- Direct magnetic dipolar interactions (homonuclear and heteronuclear)
- Indirect electron couple interactions (homonuclear and heteronuclear)
- Electric quadrupolar interactions (for nuclei with spin $I > \frac{1}{2}$)

- Electron shielding interactions (chemical shift)

Each of these interactions gives rise to NMR spectral broadening which it is desirable to remove.

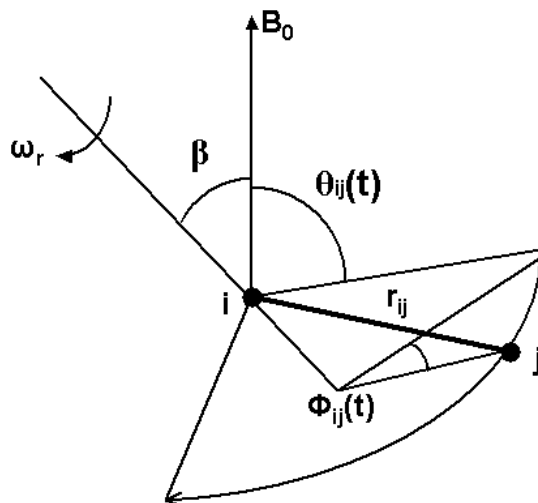


Figure 2.13: Illustration of the motion of a typical internuclear vector r_{ij} when a solid is rotated with angular velocity ω_r about an axis inclined at an angle β to the direction of the static magnetic field B_0 . The figure is based on a figure from [37].

By using the dipolar interactions as an example, the principle of the magic angle is explained. The truncated Hamiltonian dipolar interaction for nuclear pairs i, j in solids, both like and unlike, is [37]

$$H_d = \sum_{i < j} \frac{1}{2} \gamma_i \gamma_j \hbar^2 r_{ij}^{-3} (I_i I_j - 3 I_{iz} I_{jz}) (3 \cos^2 \theta_{ij} - 1) \quad (2.14)$$

where γ_i and γ_j are the nuclear gyromagnetic ratios, r_{ij} is the internuclear displacement, and θ_{ij} is the angle between r_{ij} and the Zeeman field B_0 , which is directed along the z axis. The NMR spectrum is calculated by treating H_d as a perturbation on the Zeeman term H_z , where [37]

$$H_d = - \sum_i \gamma_i \hbar I_i B_0 \quad (2.15)$$

Since the isotropic average $\cos^2 \theta_{ij} = \frac{1}{3}$, Equation 2.14 gives that the isotropic average of the dipolar Hamiltonian, $\bar{H}_d = 0$, and rapid isotropic motion eliminates the dipolar interaction from the NMR spectrum, yielding very sharp lines.

If a solid specimen is rotated uniformly with angular velocity ω_r about an axis inclined to B_0 at an angle β , every internuclear vector r_{ij} in the solid describes a motion illustrated

in Figure 2.13. The factor $3 \cos^2 \theta_{ij} - 1$ in Equation 2.14 becomes zero if β is equal to 54.7° , the magic angle. All spin interactions become time-dependent and sidebands appear at integer multiples of the spinning rate.

As for the dipolar interactions, the factor $3 \cos^2 \theta_{ij} - 1$ also appears for the other interactions. By spinning the samples at the magic angle, line broadening in the spectra is reduced by several orders of magnitude to a liquid-like breadth [37].

Although narrower lines are obtained because of the HR-MAS effect, large molecules like proteins and lipids appear as broad signals in the HR-MAS spectrum. A common method to reduce these broad signals is by utilizing their short T_2 values. This is done by using a Carr-Purcell-Meiboom-Gill (CPMG) spin echo sequence $[90^\circ - (\tau - 180^\circ - \tau)_n]$, in order to separate signals according to their different T_2 value and enhance the metabolites with respect to those of macromolecules.

HR-MAS has been applied to numerous types of tissue and provided detailed descriptions of the chemical composition of healthy and diseased tissue from, for instance, kidney, breast, brain and prostate. The HR-MAS technique gives the opportunity to investigate the same sample by microscopy after MR analysis, providing direct comparisons of morphological and chemical characteristics.

2.5.2 Analysis of HR-MAS Spectra

Biological tissue contains a large amount of MR detectable compounds and the resulting high field proton MR spectra can be very intricate. Different approaches are used to investigate MR spectra. Spectral characteristics can be explored by examining peak intensities or peak areas. Peak areas can be obtained by integration or, in spectra where peaks are overlapping, by deconvolution. Metabolites of interest can be quantified by comparing peak areas to an internal reference like water. Peak-by-peak investigations to extract information have been useful in many studies, and makes direct comparison between chemical and biological features possible.

MR spectra from biological species are often investigated with respect to a specific disease. Characterization of spectral outcome can be tested by comparisons between samples from different stages or to controls. Several MR spectroscopic studies have shown that almost all resonances influence the spectral patterns. Visual inspection of such spectra yield limited information from the available data.

In the last years, multivariate analysis has gained a lot of interest in MR data analyses. Multivariate spectral analyses can be applied to entire data sets. The purpose of these analyses is to reduce the complexity in the data and generate and test scientific hypotheses [38].

An often used unsupervised method for analyses of MR spectroscopic data, is principal component analysis, PCA. The objective of PCA is to convert the multiple and possibly correlated parameters from the measurements to a non-correlated and much smaller set of parameters. PCA creates linear combinations from the original spectra based on variance, leading to a reduced set of independent variables describing the original data set [39], [3].

A set of MR spectra can be considered as a D -dimensional vector \mathbf{x} , consisting of possibly correlated elements. D corresponds to the number of points describing the spectra. By using PCA, the vector \mathbf{x} is transformed into another D -dimensional vector \mathbf{y} , whose elements are not correlated. From the resulting \mathbf{y} -vector, d variables, where $d < D$, are selected that approximately represent the original measured vector \mathbf{x} . These variables are called principal components [38].

The first principal component, $PC1$, contains the largest part of the variance in the data set. The smaller amounts of the variance are contained in the consecutive principal components. In conclusion, PCA is a useful method in visualization of complex data and to reduce data input before classification. In analyses concerning MR spectra, PCA result in sample grouping based on score values for the principal components, i.e. an important tool in MR spectroscopic analyses [39], [40].

2.6 Diffusion-Weighted Magnetic Resonance Imaging

MRI is widely used for detection and diagnosis of diseases, including malignant tumors. For the assessment of viability and aggressiveness of the tumor or its response to therapy, a method that gives information at the cellular level is desirable. Diffusive motion arises from intrinsic energy in the molecules leading to random molecular motions [35].

2.6.1 Principles of Diffusion Imaging

Diffusion-weighted magnetic resonance imaging, DW-MRI, provides MR images where the signal intensity is proportional to the random motion of free water molecules. In diffusion imaging, normal tissue has a lower signal intensity than abnormal tissue as the molecules within it are free to move, while diffusion becomes restricted when pathology is present [41]. Figure 2.14 illustrates the difference between free and restricted diffusion.

According to Fick's law a local difference in concentration will give rise to a net flux of molecules from high concentration regions to low concentration regions. In mathematical terms, J , the net amount of material diffusing across a unit cross-section perpendicular to a direction, x , is proportional to the concentration gradient $\Delta C/\Delta x$, i.e. change in

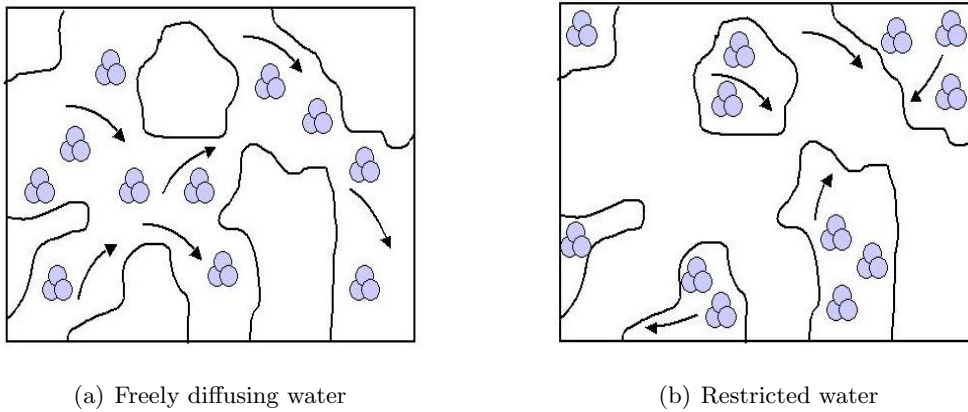


Figure 2.14: The figure shows an illustration of (a) free and (b) restricted water.

concentration per unit distance, as given in Equation 2.16.

$$J = -D \frac{\Delta C}{\Delta x} \quad (2.16)$$

where the constant of proportionality, D , is the diffusion coefficient in units of m^2/s . The minus sign indicates that the material is transported in the direction of decreasing concentration.

Diffusion has until now been discussed for homogeneous systems where diffusion is 'free' or isotropic. In biological tissues, the assumption of free isotropic diffusion is not generally valid. The diffusion is influenced by natural barriers within the cells. Motion is restricted by boundaries such as ligaments, membranes, macromolecules and fibers. Macromolecules in the different cellular compartments change the viscosity and bind water, thus reducing free diffusion. The measured diffusion coefficient in a system where the diffusion is non-isotropic, represents a mixture of diffusion in different compartments with specific degrees of restriction. The term 'apparent diffusion coefficient', ADC, has therefore been applied for the measured diffusion coefficients obtained in *in vivo* studies. This coefficient reflects the net displacement of molecules in a biological tissue [29].

The ADC for a given direction is calculated on a pixel-by-pixel basis by fitting signal intensities to the Stejskal-Tanner equation:

$$S_b = S_0 \cdot e^{-b \cdot \text{ADC}} \quad (2.17)$$

where S_b represents the signal intensity with diffusion gradient, S_0 the signal intensity without diffusion gradient and b the gradient factor in s/mm^2 of the pulse sequence, a measure of strength of the diffusion gradient.

The signal intensity in a diffusion-weighted image also depends on the spin density,

T_1 , T_2 , TR and TE. To eliminate these influences and obtain pure diffusion information, one can calculate diffusion maps, ADC maps. Such a map can be calculated by combining at least two diffusion weighted images that are differently sensitized to diffusion but remain identical with respect to other parameters, spin density, T_1 , T_2 , TR and TE. By using the image S_0 without diffusion weighting ($b = 0$) and one diffusion-weighted image ($b > 0$), the ADC value for each pixel can be calculated with the following equation:

$$ADC = -\frac{1}{b} \ln \frac{S_b}{S_0} \quad (2.18)$$

Anisotropy

As a consequence of their spatial structure, biological tissues exhibit anisotropic diffusion behaviour. This means that the diffusion coefficient depends on the direction and the sensitizing gradient. The diffusion anisotropy effects require geometrical parameters to be taken into account when studying diffusion.

For an anisotropic diffusion process, the signal intensity is described by Equation 2.19.

$$S_b = S_0 \cdot e^{-\sum b_{ij} \cdot ADC_{ij}} \quad (2.19)$$

where i and j can be any of the three spatial directions x, y, z in an orthogonal frame of reference. The b_{ij} terms characterize the sensitizing gradients along the i and j directions, while the ADC_{ij} are defined in terms of Fick's law for anisotropic diffusion:

$$J = -ADC_{ij} \frac{\Delta C}{\Delta j} \quad (2.20)$$

For an anisotropic medium, differences in concentration along e.g. x, can lead to a net particle flux along any of the three spatial directions x, y, z, described by D_{xx} , D_{yx} , D_{zx} . Anisotropy also entails that D_{xx} , D_{yy} , D_{zz} , etc. in general will be different.

Mathematical considerations show the following:

1. Together these diffusion coefficients form a tensor, the diffusion tensor
2. The tensor is symmetric, $D_{ij} = D_{ji}$
3. In each point of space, there exists a frame of reference in which the tensor becomes diagonal: $D_{ij} = 0$ if $i \neq j$

The general, three dimensional diffusion *in vivo* is considered as a tensor D represented by the matrix:

$$\begin{pmatrix} D_{xx} & D_{xy} & D_{xz} \\ D_{yx} & D_{yy} & D_{yz} \\ D_{zx} & D_{zy} & D_{zz} \end{pmatrix}$$

As stated over, the matrix is symmetric, $D_{zx} = D_{xz}$, $D_{yx} = D_{xy}$, $D_{zy} = D_{yz}$, so D can be calculated by applying only six different diffusion encoding directions instead of nine. The

average diffusion tensor, \overline{D} , measures the spatially averaged mobility of free water, and is calculated from the eigenvalues of the tensor:

$$\overline{D} = \frac{\lambda_1 + \lambda_2 + \lambda_3}{3} \quad (2.21)$$

Use of DW-MRI

The most common use of DWI is in the brain after infarction. In early stroke, cells swell and absorb water from the extracellular space. Since cells are full of large molecules and membranes, diffusion is restricted and the ADC of the tissue is reduced. DWI can also be used to differentiate malignant from benign lesions and tumor from edema and infarction and thereby be able to monitor response to therapy. This is because the disease processes have different ADC values [29], [42]. Several researchers have correlated the increased value of tumor ADC to the tumor necrotic fraction [9], [43]. They proposed that the tumor ADC acts as a surrogate marker of tumor necrosis, mainly as a result of the increased extracellular water.

Image Acquisition

Traditionally, diffusion tensor images have been acquired by single-shot echo-planar imaging, EPI, methods achieving a good SNR with a low RF power deposition. EPI utilizes gradient rephasing, which results in spatial distortions from magnetic susceptibility effects, especially near air interfaces [41]. Recent studies has demonstrated the feasibility of using radiofrequency, RF, or RF-refocused single-shot fast spin echo, SSFSE-based diffusion MR acquisitions, which provide images without the significant degree of spatial distortions.

The imaging is accomplished by placing strong sensitizing gradient pulses around a 180° -pulse in a spin echo sequence. These pulses serves to attenuate the signal coming from spins that are diffusing in the presence of the gradient pulses. In diffusion tensor imaging, the diffusion encoding gradients are applied in several directions. The achieved diffusion weighted images rely on the b-value defined by the image sequence parameters

$$b = (\gamma\delta G)^2\left(\Delta - \frac{\delta}{3}\right) \quad (2.22)$$

where γ is the gyromagnetic ratio, G is the magnitude of the diffusion-encoding gradients, δ is the duration of each diffusion encoding gradient and Δ is the time interval between the leading edges of the diffusion-encoding gradients.

2.7 Thermo Luminescence Dosimetry (TLD)

Thermoluminescence is emission of light that occurs when a material is heated to a specific temperature. Thermo Luminescence Dosimetry, TLD, is based on the principle that imperfect crystals can absorb and store the energy of ionizing radiation. When heated to a temperature typical for the detector material, the electrons return to the conducting

band and recombine with a hole, resulting in emission of energy in form of electromagnetic radiation [44]. This is illustrated in Figure 2.15.

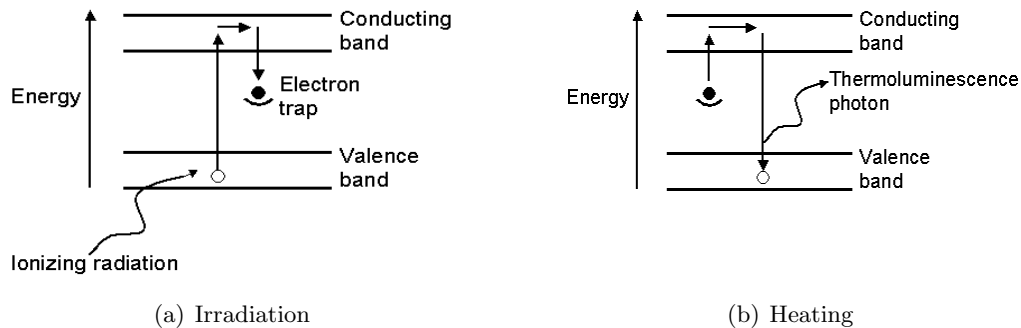


Figure 2.15: An energy-level diagram illustrating the process of thermoluminescence. The crystal exhibits thermoluminescence by ionizing irradiation. The figure is based on a figure from [44].

This emission is detected by a photomultiplier (Figure 2.16) and is correlated to the absorbed dose received by the crystal. The amount of light emitted is dependent upon the ionizing radiation exposure.

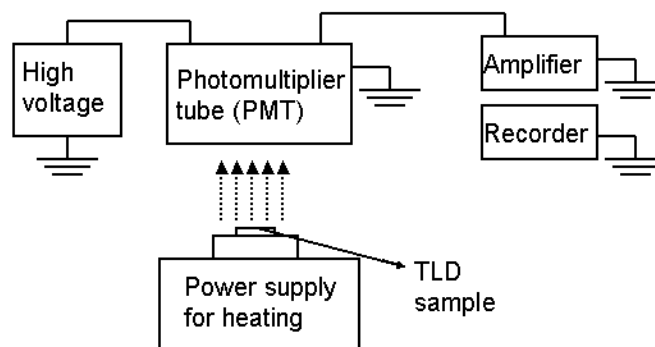


Figure 2.16: A schematic diagram showing the apparatus for measuring the thermoluminescence output. The irradiated material is placed in a heater cup. The emitted light is measured by a photomultiplier tube, PMT, which converts the light into electrical current. The current is then amplified and recorded. The figure is based on a figure from [44].

There are two main types of TLDs. Both consist of a small crystal, either calcium fluoride or lithium fluoride, and a heating filament in a small glass bulb. The former is used to record gamma exposure, the latter for gamma and alpha exposure. The TLD can be reused after annealing. The calibration is necessary since the TLD material is affected

by their previous radiation history. The thermoluminescence is linear compared to the absorbed dose up to 10^3 rad, beyond this it becomes supralinear. The results of the TLD measurements for the higher doses are calibrated for this supralinearity.

2.8 Human Xenografts as Tumor Models

Xenografts are human tumors grown in experimental animals. The host animal have weakened immune system for not rejecting the human tumor cells. Nude mice lacks the thymus. The thymus processes T-lymphocytes which kill foreign cells and stimulate other immune cells to produce antibodies. But even if the immune system in nude mice without thymus is strongly reduced, a few still will reject tumor cells [21].

The benefit of using xenografts as a tumor model is that many of the characteristic histological features from the original tumor can be maintained. In addition, the metabolism in mice occurs at about five times faster in mice compared to humans. Mice are considered the prime model of human disease since they are genetically tractable and share 99 % of their genes with humans.

2.9 Software

nICE

Nordic Image Control and Evaluation, nICE, is a general purpose image processing and analysis tool with emphasis on clinical utility in perfusion, diffusion and functional MRI. It is a medical viewing, analysis and processing package developed to use on a standard Windows platform. In addition to a wide range of basic image processing and analysis functions, nICE provides comprehensive functionality for dynamic image analysis and diffusion imaging including DTI, Fiber Tracking and processing of functional MRI data. nICE is developed by Nordic Ice Medical AS, Bergen, Norway in collaboration with Department of Radiology, Rikshospitalet University Hospital, Oslo, Norway [45].

SAGE

Spectroscopy Analysis General Electrics, SAGE, is a processing tool for spectroscopy data acquired on MR scanners. SAGE runs on a UNIX platform and includes features for spectral post-processing.

AquaCosmos

Aquacosmos is an image acquisition and image processing software for biological applications, made of Hamamatsu Phottonics Norden AB, Solna, Sweden. It works together with a high-sensitivity digital CCD camera and various types of imaging sensors [46]. It is used in this work to examine tumor HE-stains in order to calculate necrotic areas of tumors.

SPSS

SPSS is a statistical tool founded in 1968 which in addition to a large amount of statistical analysis also provide advanced visualization and graphing capabilities. SPSS is made of SPSS Inc, Chicago, US [47].

Chapter 3

Materials and Methods

3.1 Experimental Animals and Anaesthesia

3.1.1 Experimental Animals and Tumor Model

Both experiments were performed using male GBNIH nude mice. The mice were bred under specific pathogenic-free conditions, with constant temperature, 24°C- 26°C, and constant air humidity, 30 - 50 %. The mice were housed in cages with air-flow racks. Each cage contained 5 - 8 mice and the cages were bedded with aspen wood chips (Scanbur BK A/S, Denmark). The mice were fed with standard pellet diet (Special Diets Service, England) and water *ad libitum*.

The human colon cancer xenograft HT 29 was used. HT 29 is a human colonic adenocarcinoma cell line that express differentiation features characteristic of mature intestinal cells. The xenografts were initially established by subcutaneous injection of cells in suspension and maintained by serial passage of fragments of viable tumor. A tumor tissue of 2 x 2 mm² was inoculated on each flank of the mice. This was performed by technologists at the animal department at Rikshospitalet-Radiumhospitalet HF.

Tumor size was measured twice a week. The perpendicularly shortest and longest diameter of the tumor was measured by a slide caliper. The tumor volume, V , was estimated by the following equation

$$V_{caliper} = \frac{\pi}{6} \cdot a \cdot b^2 \quad (3.1)$$

where a is the longest diameter and b is the shortest diameter. This formula is derived from the formula for the volume of an ellipse, where the b and c axes are assumed to be equal.

The mice having tumors with a minimum diameter of 10 mm at the shortest axis were

inserted into the experiment. Most of the tumors satisfied this criteria 4-5 weeks after implantation of tumor tissue.

The mice were sacrificed by neck dislocation at the end of the experiment. Both experiments were approved by the national committee of experimental animals, Forsøksdyrutvalget. The signed application forms are enclosed in Appendix A.

3.1.2 Anaesthesia

The mice were sedated subcutaneously with zoletil mixture during chemoradiation therapy and MR imaging Zoletil veterinaria (containing 125 mg tiletamine and 125 mg zolazepam) was mixed with 10 ml Narcoxyl veterinaria (xylazine 20 mg/kg) and 0.5 ml Torbugesic ('Fort Dodge' butorphanol 10 mg/ml). The mixture was kept in a 4°C refrigerator and new solutions were prepared weekly.

For MR imaging the mice were given a subcutaneous injection of 0.15 ml/25 g mouse. Prior to radiation and chemotherapy a dosage of 0.05 ml/25 g mouse was used. Eye ointment (Simplex, Ophtha) was used during every anaesthesia to prevent the eyes from dryness.

3.2 Description of the Experiments

3.2.1 Experiment 1

An overview of Experiment 1 is shown in Figure 3.1. Due to differences in growth rate, the mice were included in the experiment on three consecutive Mondays (Day 1). MR acquisitions were performed of all the tumors prior to treatment (Day 1) and at four different times after irradiation (Day 3, Day 5, Day 8, Day 12). The MR data were analyzed using dedicated software before statistical analyses were performed on the results.

12 mice with HT29 xenografts on both flanks were allocated into two groups:

- Group 1: The radiation group – 16 tumors receiving 15 Gy radiation therapy
- Group 2: The control group – 8 tumors

Two mice were sacrificed after each MR acquisition for obtaining tissue samples to histology (left tumor) and *ex vivo* HR-MAS spectroscopy (right tumor). The controls were sacrificed after the MR acquisition at Day 1.

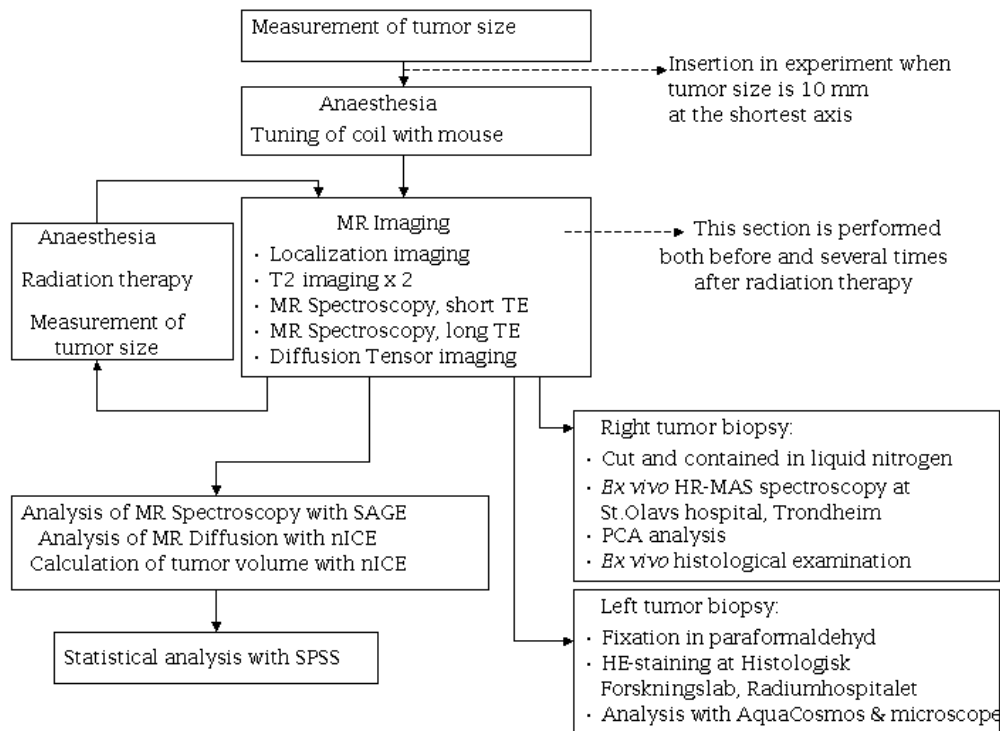


Figure 3.1: Schematic view of the experimental procedure in Experiment 1.

3.2.2 Experiment 2

An overview of Experiment 2 is shown in Figure 3.2. In this experiment the mice received chemoradiation therapy. The mice were included in the experiment on two consecutive Mondays (Day 1). MR acquisitions were performed prior to treatment (Day 1) and at 3, 5 and 10 days after onset of treatment. The MR data were analyzed using dedicated software before statistical analyses were performed on the results.

Seventeen mice with HT29 xenograft on both flanks (1 mouse with one tumor) were allocated into three treatment groups; Control (Group 1), Capecitabine (Group 2) and Capecitabine + Oxaliplatin (Group 3). All left-sided tumors in the three groups were irradiated with 15 Gy at Day 2. The right tumors were control tumors.

Mice were sacrificed after MR acquisitions at Day 5 and Day 10. Tumors were excised for histology and *ex vivo* HR-MAS spectroscopy.

Tumor and Toxicity Measurements

Tumor sizes were recorded twice a week and at the days of MR imaging. Body weights were measured at Day 1, Day 2, Day 3, Day 4, Day 5 and Day 10. Toxicity was evaluated

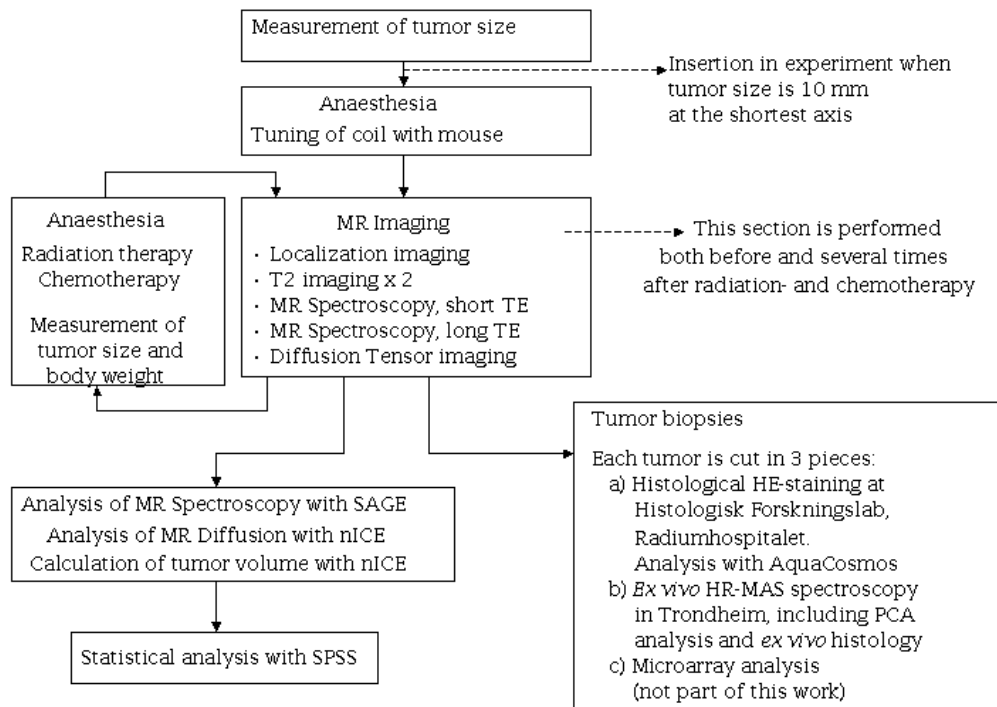


Figure 3.2: Schematic view of the experimental procedure in Experiment 2.

in terms of mortality and the body weight ratio W_n/W_0 , where W_n is the body weight after n days after the start of treatment and W_0 is the weight at the start of the treatment.

3.3 Radiation Therapy

The tumors were irradiated with a Cobalt⁶⁰-unit (Mobaltron 80, TEM Instruments Limited). The ⁶⁰Co source is contained inside a stainless-steel capsule sealed by a welding, which is placed in another steel capsule and welding to prevent any leakage of the radioactive material, see Figure 3.3. The ⁶⁰Co source emits radiation when the ⁶⁰Co nucleus decays to ⁶⁰Ni by emission of β -particles and two photons per disintegration with energies of 1.173 MeV and 1.332 MeV. These γ -rays constitute the useful treatment beam. The β -particles are absorbed in the cobalt metal [44].

For absolute dosimetry of ⁶⁰Co units in radiation therapy, there is chosen a depth of reference in 0.5 cm water at a distance 80 cm from the source and a field size of 10 x 10 cm. Since the rate of decay of ⁶⁰Co is known, an absolute measurement will give the dose rate in future exposures.

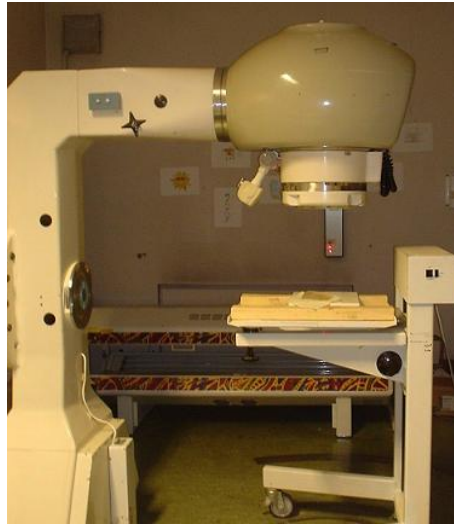


Figure 3.3: The Cobalt⁶⁰-unit used in irradiation of the tumors in both experiments.

When a patient or mice is treated with a megavolt beam, the surface dose is lower than the maximum dose that occurs in the subcutaneous tissues. In contrast to lower energy beams which give rise to maximum ionization at, or close to, the skin surface, the megavoltage beams produce an initial electronic buildup with depth, resulting in maximum dose at the equilibrium depth. A bolus is a tissue-like material placed on the skin surface to compensate irregular contours and achieve a flat surface perpendicular to the radiation direction. In these experiments, a bolus of 5 mm was used. The bolus function as a buildup region and maximize the dose at the skin or in the area near the skin. For the ⁶⁰Co unit at 80 cm distance, the buildup dose distribution in polystyrene for a 10 x 10 cm field is given in Table 3.1.

| Depth [mm] | ⁶⁰ Co [%] |
|------------|----------------------|
| 0 | 18.0 |
| 1 | 70.5 |
| 2 | 90.0 |
| 3 | 98.0 |
| 4 | 100.0 |
| 5 | 100.0 |

Table 3.1: Buildup dose distribution in polystyrene for a 10 x 10 cm field by the use of a ⁶⁰Co unit [44].

The ⁶⁰Co unit was initially measured the 15th of September in 1996, with a dose rate of $A^{-1}(0) = 31.350$ s/Gy. Since the ⁶⁰Co source is decaying, the dose rate is adjusted monthly according to the decay constant of the ⁶⁰Co source. Correct dose rate at the date

of radiation, $A^{-1}(t)$, is calculated by the following formula

$$A^{-1}(t) = A^{-1}(t_{15}) \cdot \frac{\ln 2}{T_h} \cdot n + A^{-1}(t_{15}) \quad (3.2)$$

where $A^{-1}(t_{15})$ is the dose rate at the 15th day of the last month, T_h is the halftime of Cobalt⁶⁰ (1925.1 days), and n the number of days since the 15th. The unit of dose rate is s/Gy. The radiation time in seconds is found by multiplying the dose rate $A^{-1}(t)$ with the dose in Gy.

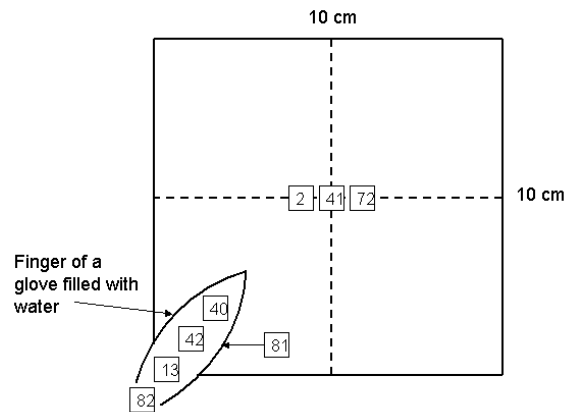


Figure 3.4: Illustration of the radiation field and placement of numbered TLD chips at testing with phantom.

In both experiment the dose to the tumor was 15 Gy. The dimensions of the source give a large penumbra which has to be taken into account when the mouse (placed in the corner of the radiation field) shall receive a certain dose. The correct dose was found by using a phantom. The phantom was a plastic glove filled with tempered water. The radiation field was adjusted to 10 x 10 cm and the distance between source and phantom was 80 cm. The glove was placed as shown in Figure 3.4. Below and above one of the fingers and in the center of the radiation field there were placed TLD chips to measure the radiation dose.

Each TLD chip contained three crystals, which lead to a mean value and a standard deviation (SD) of three measurements in Coloumb, C, per chip. The dose was calculated by multiplying the charge or net signal in nC with a calibration factor in Gy/nC. The net signal for high radiation doses is not linear, and a supralinearity correction was applied to achieve the correct dose. All values were calibrated for a background value of 0.210 Gy.

Measurements with TLDs gave the doses listed in Table 3.2. 13.09 Gy were given to the tumor region at 1.5 cm into the radiation field from the outer corner (TLD number 42). This corresponds to 87.3 % of the wanted dose. To compensate for this, the tumors are irradiated a time corresponding to 17.18 Gy in the center of the radiation field.

| TLD No | Placing | Dose [Gy] |
|--------|----------------------------------|-----------|
| 2 | Center, left | 14.81 |
| 41 | Center, middle | 14.85 |
| 72 | Center, right | 14.28 |
| 40 | 3.2 cm into field | 15.14 |
| 42 | 1.5 cm into field | 13.09 |
| 13 | In the corner | 5.10 |
| 82 | 1.8 cm out of field | 0.28 |
| 81 | Under phantom, 1.5 cm into field | 12.72 |

Table 3.2: TLD dose measurements with phantom

Prior to radiation, the mouse was sedated and eye salve applied. The sleeping mouse was placed in the radiation field with the tumor 1.5 cm into the radiation field, measured from the outer corner. This placing reduced radiation deposition to the rest of the mouse. Figure 3.5 shows the mouse in the radiation field, the placing of TLD with tape and the bolus.

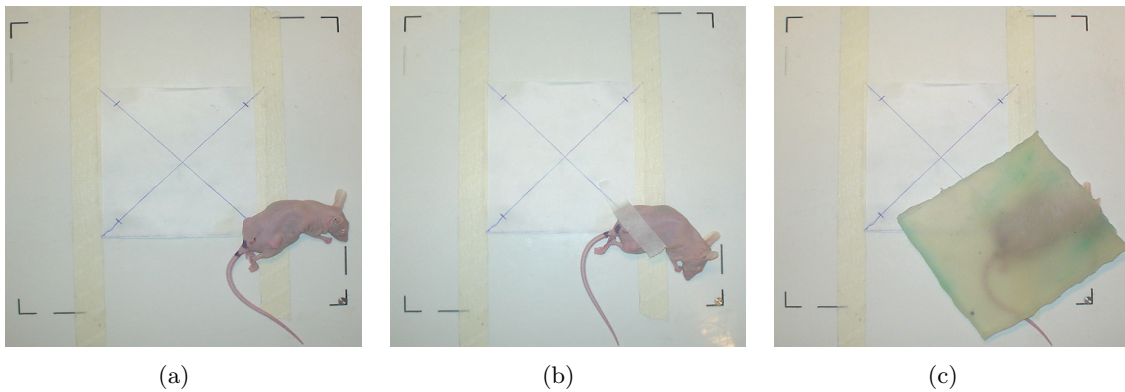


Figure 3.5: The figure shows an illustration of (a) a mouse in the radiation field, (b) a mouse with TLD chip fastened with tape and (c) a mouse with bolus. The tumor is placed 1.5 cm into the radiation field, marked with a cross.

3.4 Chemotherapy

The radiosensitizing drugs Capecitabine and Oxaliplatin were given as part of the treatment in Experiment 2. The mice not receiving chemotherapy, were given placebo solutions.

Capecitabine

Capecitabine was obtained in 150 mg tablets (Xeloda, Roche, United Kingdom). After crushing, capecitabine powder was suspended in 40 mM citrate buffer (pH 6.0) containing

5% gum arabic as the vehicle and then administered by gavage to the mice. The mice in Group 2 and 3 received a dosage corresponding to 359 mg/kg/day. The animals in Group 1 received only the vehicle. Administration of Capecitabine and vehicle was done daily at 10 p.m. from Day 1 to Day 5.

Oxaliplatin

Liquid Oxaliplatin was obtained in 5 mg/ml (Eloxatin, Sanofi-Synthelabo, France) and diluted five times in 5 % glucose solution. The animals in Group 3 received oxaliplatin as a single i.v. injection via the caudal vein at a dosage corresponding to 10 mg/kg. The other two groups were given i.v. injections of 5 % glucose solution as placebo. Oxaliplatin and placebo was administered at 8 p.m. on Day 2. Irradiation of the left tumors in all three groups were performed two hours later, at 10 p.m. at Day 2.

3.5 MR

3.5.1 Preparations for MR Acquisitions

The mouse was sedated and eye ointment was applied. The mouse was placed in a stretcher made of extruded polystyrene thermal insulation material (Styrofoam). To reduce breathing artefacts in the MR images the mouse was placed with the tumor down in the stretcher as shown in Figure 3.6a). After MR acquisition of one of the tumors, the mouse was turned to place the other tumor down in the stretcher and perform MR acquisition of that tumor.

The loaded mouse coil was tuned with a vector impedance meter (Hewlett Packard 4193A) to 63.89 MHz. This is the Larmor frequency of the protons, whose resonance signal is being detected. The tuning match the MR system before acquisition of data and results in a higher output signal and minimizes losses due to external sources with other frequencies.

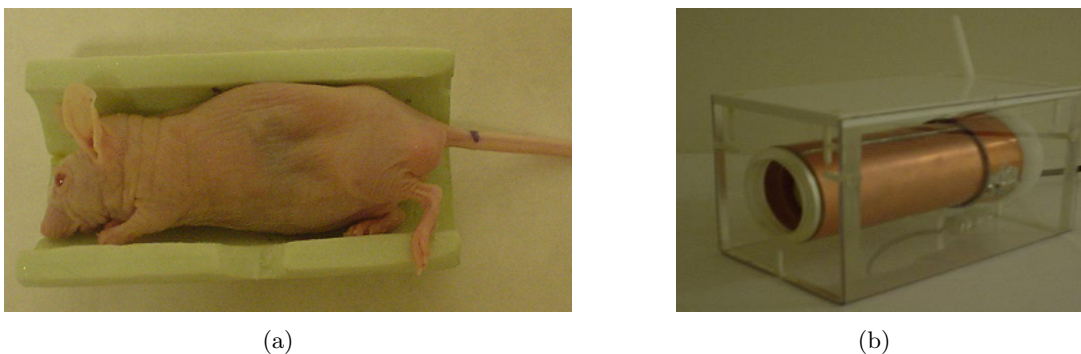


Figure 3.6: (a) An illustration of a mouse in the stretcher, and (b) the mouse coil. The stretcher with mouse are placed inside in the coil during imaging.

3.5.2 MR Imaging

MR imaging was performed using a 1.5 T whole-body clinical MR system (Signa, General Electrics, Milwaukee, USA) at the MR facility at Rikshospitalet-Radiumhospital HF (Figure 3.7). The volume to be excited in imaging of mice is substantial less than the volume to be excited at clinical imaging of patients. Thus, the transmitted signal was attenuated with 30 dB during all experiments.



Figure 3.7: The 1.5 T clinical MR scanner used in the experiments. The mouse coil is in the iso-center of the MR scanner.

The mouse coil was attached to the clinical MR scanner in the connector for standard transmit/receive extremity coils used for MR. The coil was placed in the iso-center of the MR scanner.

***In vivo* MR Image Acquisitions**

The excitation field B_1 must be perpendicular to the main magnetic field B_0 , hence the mouse coil was placed as illustrated in Figure 3.8.

The MR-protocol given in Table 3.3 was used for both Experiment 1 and Experiment 2. All imaging parameters were kept throughout the experiment. Below a description of the different sequences, including the imaging parameters, are given.

Localization

A fast 3D gradient echo sequence giving survey images of the mouse in the axial, coronal and sagittal directions were performed (Figure 3.9). The acquisition was performed with an acquisition matrix of 256 x 256, 2 mm slice thickness and no slice gap.

| Sequence No | Type of sequence | Scantime |
|-------------|--------------------------------|----------|
| 1 | Localization | 1:36 |
| 2 | T ₂ -weighted image | 1:52 |
| 3 | Spectroscopy, short TE | 5:04 |
| 4 | Spectroscopy, long TE | 5:04 |
| 5 | Tensor diffusion image | 1:52 |
| 6 | T ₂ -weighted image | 0:40 |

Table 3.3: The MR-protocol used in imaging of a tumor. For large tumors, the scan times of T₂-weighted images and diffusion series were increased due to the increased number of slices needed.

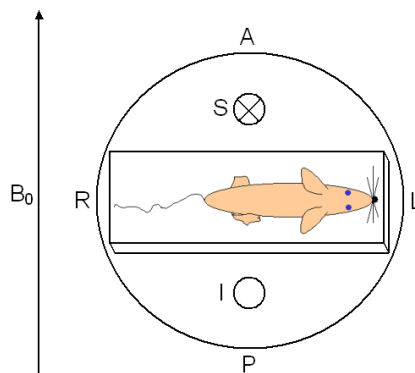


Figure 3.8: The figure illustrates the placing of the mouse coil in the MR scanner. The mouse is placed perpendicular to the B₀ field in the MR scanner. A = anterior, P = posterior, R = right, L = left, S = supine and I = inferior.

T₂-Weighted Image

Axial 2D T₂-weighted images were obtained using a fast spin echo sequence. These images were used for orientation of the spectroscopy voxel and for calculating tumor volume. The acquisition was performed with an acquisition matrix of 192 x 160, TE/TR = 85 ms/4000 ms, 2 mm slice thickness, 1 mm interslice gap, bandwidth (BW) of 15.63 Hz, echo train length (ETL) of 16 and field of view (FOV) = 4 cm.

MRS

The axial T₂-weighted spin echo sequence was used for placing the volume of interest (VOI). MRS data was acquired using a PRESS sequence: PROBE/SV (PROton Brain Examination/Single Volume). PRESS, Point Resolved Spectroscopy, is a double spin echo sequence that uses a 90°-180°-180° slice selective pulse sequence to acquire the proton spectra. The 90°-pulse rotates the spin into the xy-plane, while the first 180°-pulse rotates the spin into the xz-plane. The second 180°-pulse results in spin rotation into the xy-plane and the resultant is a FID originating from the VOI. The sequence contains chemical selective saturation water suppression pulses and uses water as an internal reference to locate metabolic references.

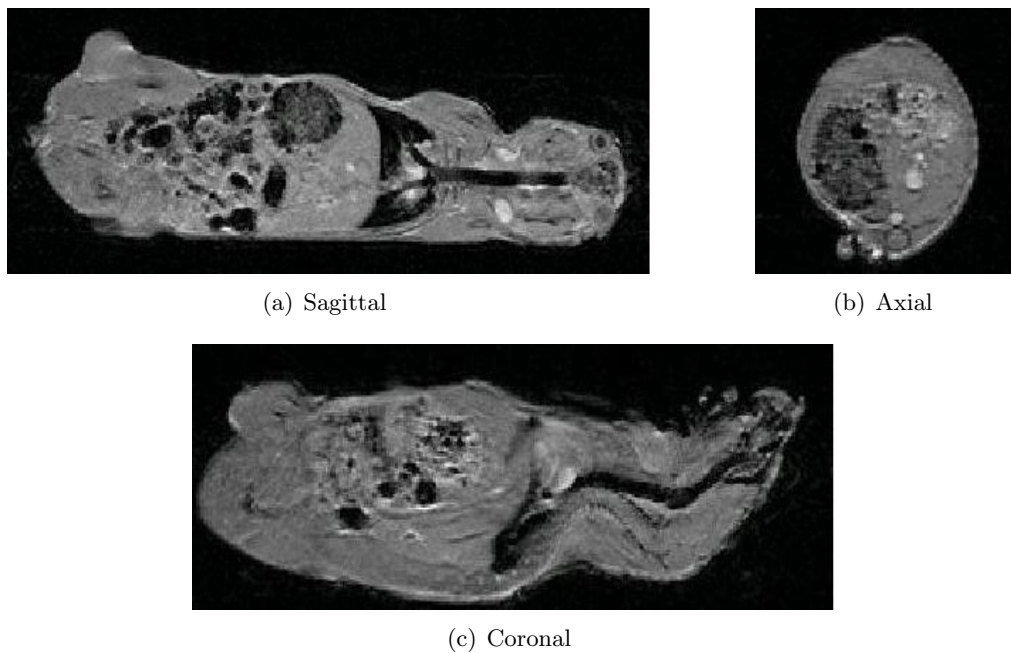


Figure 3.9: (a) A survey image of a mouse in the sagittal direction, (b) a survey image in the axial direction and (c) a survey image in the coronal direction.

The VOI was shimmed using an automated procedure to less than 15 Hz in all instances. Typically, 5 - 10 Hz linewidths of the water signal were achieved. The VOI of $[4 \text{ mm}]^3$ was placed in the central part of the tumor and spectra was obtained from this VOI. Spectra were acquired at two different TE's, TE = 35 ms and TE = 144 ms. For both spectra TR = 2000 ms, phase cycling = 8 and 128 acquisitions was used.

Diffusion Tensor Image

A single shot fast spin echo (SSFSE) sequence providing diffusion weighting in the direction of slice selection was used. This acquisition provided images without the significant degree of spatial distortions that affect EPI-based diffusion imaging. The tensor DTI-SSFSE sequence used in the experiments contained six gradient directions ($[1 \ 0 \ 1]$, $[-1 \ 0 \ 1]$, $[0 \ 1 \ 1]$, $[0 \ 1 \ -1]$, $[1 \ 1 \ 0]$ and $[-1 \ 1 \ 0]$) in addition to the zero gradient ($[0 \ 0 \ 0]$). This enabled calculation of the diffusion tensor and its eigenvalues, λ_1 , λ_2 and λ_3 . The acquisition was performed with an acquisition matrix of 192×160 , TE/TR = 85 ms/4000 ms, BW = 15.63 Hz, ETL = 16, 2 mm slice thickness, 1 mm interslice gap and FOV = 14 cm. All DTI acquisitions were performed using a $b_1 = 0 \text{ s/mm}^2$ and $b_2 = 300 \text{ s/mm}^2$.

T₂-Weighted Image

Axial 2D T₂-weighted image was obtained using a fast spin echo sequence with the same dimensions as the diffusion series (FOV = 14 cm), to be able to calculate ADC maps. The resting parameters were identical to the first T₂-serie in the exam.

3.6 Tumor Tissue Samples

The mice were sacrificed by neck dislocation and the tumors were excised for histological analyses and *ex vivo* HR-MAS spectroscopy.

3.6.1 Tumor Tissue Samples for Histology

Hematoxylin and eosin (HE) is a staining method for diagnostic histopathology. The dye haematoxylin colors basophilic structures with blue-purple hue, whereas the alcohol-based acidic eosin Y colors eosinophilic structures bright pink.

The basophilic structures are usually the ones containing nucleic acids, such as the ribosomes and the chromatin-rich cell nucleus, and the cytoplasmic regions rich in RNA. The eosinophilic structures are generally composed of intracellular or extracellular protein. Most of the cytoplasm is eosinophilic. Red blood cells are stained intensely red. Some structures do not stain well, for example hydrophobic structures remain clear, due to elevated level of fat.

Fixation of Tumors

After MR acquisition, the tumors were marked with a felt pen at the direction of the axial slice imaged with MR. After the sacrifice, the tumors were surgically removed. The tumor was fixated in paraformaldehyd in a 7 ml bijou container (Sterilin, United Kingdom).

Preparation of HE-stains in Experiment 1

The histological staining was performed by Histologisk Forskningslaboratorium at Rikshospitalet-Radiumhospitalet HF. First, the tumor was divided in two parts in the axial direction imaged with MR. From each of the two halves, four histological stains were made, totally 8 stains. The first histological stain was placed along the cross-section of the central axis, and the other stains were placed 1000 μm from this axis and outwards (Figure 3.10). All the histological stains had a thickness of 3 μm . By choosing a distance of 1000 μm and as much as 8 stains, the average necrotic fraction of the whole tumor could be calculated.

Preparation of HE-stains in Experiment 2

The excised tumors were cut in three parts (Figure 3.10). Part A for histological HE-staining, part B for *ex vivo* HR-MAS spectroscopy and part C to future analysis (not being part of this work). In Experiment 2 only one stain was made from each tumor. This stain was placed along the cross-section of the central axis (part A) and had a thickness of 3 μm .

Imaging of Histological HE-Stains

After preparation of HE-stains at the Histologisk Forskningslab, the stains were imaged using a multi-format scanner (Nikon, Super Coolscab 8000, ED 1.11). The scanner gave

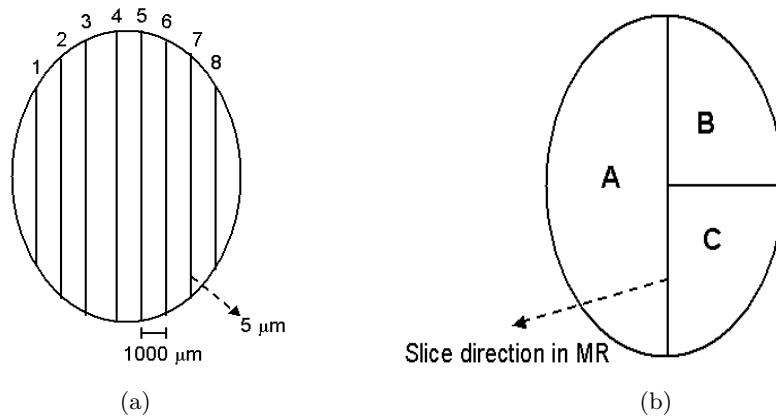


Figure 3.10: (a) Illustration of placing of the HE-stains, stain thickness and distance between the stains in Experiment 1. (b) Illustration of the tumor cutting in Experiment 2. Part A for histological HE-staining, part B for *ex vivo* HR-MAS spectroscopy and part C for future microarray analysis.

a resolution of 4000 pixels per inch, which corresponds to 157.5 pixels per mm. Photo of the HE-stains were made using a microscope with camera (Axiovert 200M, Carl Zeiss, Germany).

Calculation of Necrotic Fraction

The scanned HE-stains were analyzed by use of a light microscope (Leitz Wetzlar, Germany) and the image processing software tool AquaCosmos 2.5 (Hamamatsu Photonics Norden AB, Solna, Sweden). The necrotic fraction was found by examination of all the histological stains with manual delineation of viable tumor and tumor necrosis. The total tumor area was found by excluding the connective tissue in the outer parts of the tumor. Figure 3.11 shows a HE-stain where the ROIs around necrosis are delineated using AquaCosmos. The degree of fibrosis in the tumors was scored visually by using the microscope. The degree of fibrosis were divided into three levels corresponding to a little fibrosis (10 - 30 %), some fibrosis (30 - 60 %), and a lot of fibrosis (60 - 100 %) in the tumor.

The tumor necrotic fraction, NF , is found as the relation between the necrotic area, A_{nec} to the total tumor area, A_{tot} .

$$NF_{i=1} = \frac{A_{nec}}{A_{tot}} \quad (3.3)$$

This formula gave the tumor necrotic fraction of the HE-stained slice in Experiment 2. In Experiment 1, the total tumor necrotic fraction was found as the average of all the eight stains.

$$NF_{i=8} = \frac{1}{8} \sum_{i=1}^8 NF \quad (3.4)$$

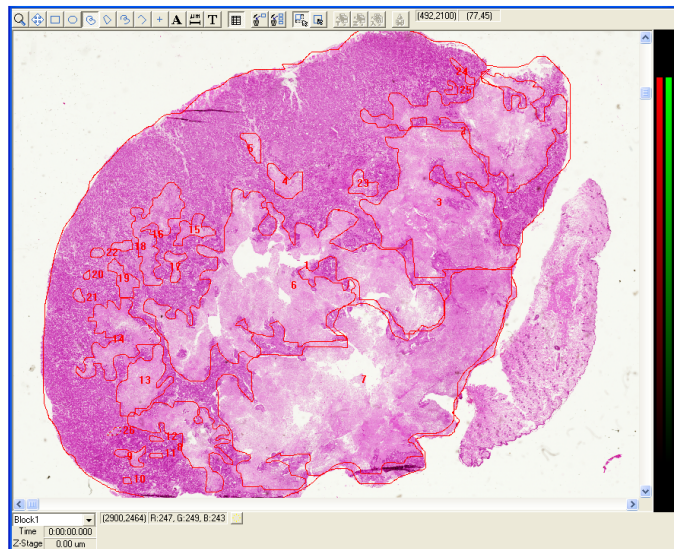


Figure 3.11: ROI is marked around the total tumor area (excluding epithelial tissue) and necrotic areas in the HE-stains by using AquaCosmos and a microscope. The necrotic fraction is calculated pixel-by-pixel as the ratio of all necrotic areas to the area of viable cells.

For some of the histological stains, there were mechanical damages caused by the preparation process. The stains that contained such large holes without biological material and the uncertainty in determination of the tumor necrotic fraction was considerable. These stains were excluded from further analysis.

3.6.2 Tumor Tissue Samples for *ex vivo* HR-MAS MR Spectroscopy

In both Experiment 1 and Experiment 2, samples for *ex vivo* HR-MAS experiments were excised. The HR-MAS experiments were performed for Experiment 1. Due to the restricted time for this thesis and limited access to the instrument in Trondheim, HR-MAS could not be included for the samples from Experiment 2. Analyses will be performed in September.

After the sacrifice, the tumors were excised by use of a pincette and a scissor, before the tumor was cut in pieces by a scalpel. It was important to remove all the skin and as much connective tissue as possible, as this would influence the HR-MAS results. The samples were immediately put in liquid nitrogen and kept in 1.5 ml cryotubes (NUNC, Nalge Europe Ltd, United Kingdom). All the tumor samples ($n = 12$) were stored in a -86°C freezer for about 1 month before the HR-MAS analysis.

Preparation of Species

The species were transported from Oslo to Trondheim in an insulating box with dry

ice. The HR-MAS analysis were performed at the MR centre at St. Olavs Hospital in Trondheim. The tissue samples were cut to fit a 4 mm o.d. rotor with inserts (total sample volume 50 μ L). When positioned in the MAS rotor, the sample was added 40 μ L phosphate buffered saline (PBS) in D₂O containing trimethylsilyl tetradeuteropropionic acid (TSP) as a chemical shift reference. The samples weighed 26.0 mg in average, the largest sample was 38.2 mg and the smallest was 15.6 mg.

HR-MAS Experiments

The HR-MAS experiments were performed on a Bruker AVANCE DRX600 spectrometer equipped with a ¹H/¹³C MAS probe with gradient aligned with the magic angle axis (Bruker BioSpin GmbH, Germany). The samples were spun at 5 kHz and all experiments were performed at instrumental temperature setting of 4°C.

Two sets of one-dimensional experiments were performed for all the samples. A single pulse experiment with 3.0 seconds of water presaturation (zgpr; BRUKER) was performed using a 60° flip angle over a sweep width of 20 ppm. The FID was acquired during 1.36 seconds and Fourier transformed into 32K, resulting in a repetition time of 4.36 seconds. 16 transients were collected. Chemical shift scale was calibrated to the TSP signal at 0 ppm.

Spin-echo experiments (cpmgpr; BRUKER) were performed using 2 seconds of water suppression prior to a 90 degree excitation pulse. 128 transients over a spectral region of 10 kHz were collected into 32K points, giving an acquisition time of 1.64 seconds. T₂-filtering was obtained using a delay of 1 ms repeated 136 times resulting in a 285 ms effective echo time. The repetition time was 3.93 seconds.

Histopathologic examination of HR-MAS analyzed samples

After HR-MAS analysis, the samples were fixed in 10 % formalin and embedded in paraffin. One 5 μ m section was cut from each block, stained with haematoxylin, erythrosin and saffron, and examined microscopically. Preparation of the species were performed by bio-engineer Eli Johannesen at Department of Laboratory Medicine, Children's and Women's Health, The Faculty of Medicine, St.Olavs hospital. The histological evaluation of tumor composition, revealing the relative areas of normal elements, necrotic tissue and fibrous tissue, were scored visually by associate professor Jostein Halgunset at Department of Laboratory Medicine, Children's and Women's Health, The Faculty of Medicine, St.Olavs hospital.

3.7 Post-Processing Analyses

3.7.1 Calculation of Tumor Volume from MR Images

The volume was calculated pixel by pixel in the MR images by using the software nICE (Nordic Ice Medical AS, Bergen, Norway). For each slice, the tumor ROI was found by manual tracking. The total tumor volume was found by summing up the ROIs in every slice with the slice thickness and gap between the slices, see Equation 3.5.

$$V_{MR} = (ST + Gap) \cdot \sum_{i=1}^n ROI \quad (3.5)$$

where n is the number of slices and ST is the slice thickness.

3.7.2 Spectroscopy

The MRS data were transferred to a remote Unix PC for further processing where peak integration was performed on the spectra in order to obtain metabolite and unsuppressed water peak areas. The spectra were reconstructed using a zero-filling with 1024 points and spectral apodization with a gauss function. This was done by using SAGE, the software provided by the manufacturer. The metabolite areas were normalized to the unsuppressed water value acquired at short TE.

Specific terms used throughout this work include choline, referring to the trimethylamine ($-\text{N}(\text{CH}_3)_3-$) proton resonance at 3.21 ppm, lipid methylene ($-\text{CH}_2-$) centered at 1.30 ppm, and methyl ($-\text{CH}_3-$) centered at 0.90 ppm.

For all tumors, the metabolite areas of choline, lipid methylene and methyl normalized to the unsuppressed water value acquired at short TE were found for both short TE and long TE spectra. The area of other pronounced peaks were found in some of the spectra. These 'other' peaks included creatine, myo-Inositol, glucose, glutamine, glutamate, fatty acids, N-acetylaspartate, alanine and aspartate. The change in choline ratio were inspected to see if it could monitor the tumor response to treatment.

3.7.3 *Ex vivo* HR-MAS Spectroscopy

The spectra were Fourier transformed and the baseline was individually adjusted using a second order linear function. Chemical shifts were calibrated to the TSP singlet at 0 ppm.

Principal Component Analysis (PCA) was performed using both water suppressed spectra and spin-echo spectra. Various spectral regions and sample groups were selected for PCA.

PCA was carried out in an unsupervised manner, with full cross-validation and mean centering using the program The Unscrambler (Camo, Norway). Score values and principal components were examined for correlation to experiment groups, tumor size, results from *in vivo* spectroscopy, tumor ADCs and tissue composition.

3.7.4 Diffusion

The obtained image data were transferred to a remote PC where quantitative diffusion measurements were obtained by calculation of ADC from user defined regions of interest (ROIs) by using the software nICE (Nordic Ice Medical AS, Bergen, Norway). For the central slice of the tumor, ROIs were drawn on trace-value maps using the corresponding T₂-weighted scans to identify the targeted tissue. The ADC for each ROI was calculated offline on a pixel-by-pixel basis as the natural algorithm of the slope of the signal intensities from differently diffusion sensitized images [$ADC = \ln(S_1/S_2)/(b_2-b_1)$]; S_1 and S_2 : signal intensities of diffusion weighted images with two different b values ($b_1 = 0$ s/mm², $b_2 = 300$ s/mm²).

3.8 Statistics

Statistical analysis was performed using SPSS 13.0, see chapter 2.9. Histograms and QQ-plots were made to test the assumption of normal distribution of the values achieved. When normal distribution was achieved, results were visualized as the mean value and standard error of the mean (SEM) of each group. Nonparametrical procedures were applied when the results deviated from the normal distribution. Paired comparisons were performed by using the Mann-Whitney Wilcoxon test with p-values 0.05 and 0.1.

Chapter 4

Results

The results from the two experiments in this work are presented separately.

4.1 Experiment 1

The experiment included 16 tumors in the radiation therapy group (Group 1) and 8 tumors in the control group (Group 2). No adverse affects were observed in the groups and all mice were alive throughout the experiment until they were sacrificed.

4.1.1 Radiation Therapy

The average radiation dose to the tumors was 15.88 Gy (range; 12.220 - 17.201 Gy). This indicates that the tumors were placed a little further into the radiation field than 1.5 cm. Table 1 in Appendix B shows the radiation doses for all the tumors in Group 1.

4.1.2 Tumor Growth Curves

Tumor growth curves based on slide caliper measurements are shown in Figure 4.1. Since all mice were sacrificed within 12 days after radiation therapy, tumor regression growth (TRG) could not be observed. The tumor volumes were found to approximately follow a normal distribution and the mean volume and corresponding standard error of the mean (SEM) for the two groups are shown in Figure 4.1. All measurements are normalized to the volumes measured at Day 1. Tumor volumes before inclusion to experiment are listed in Table 2 in Appendix B, while the tumor volumes after inclusion are given in Table 3 in Appendix B.

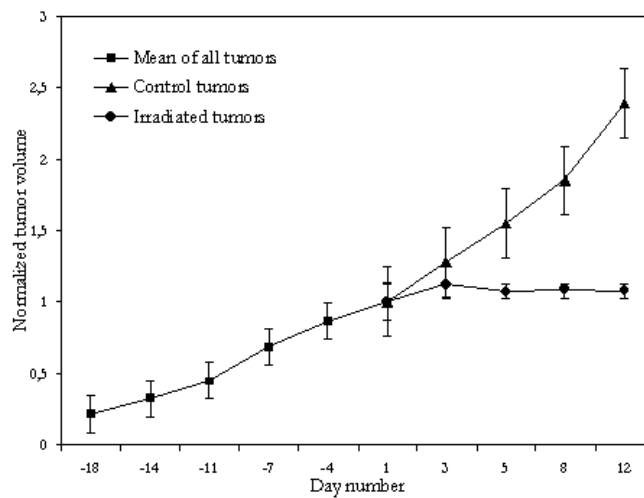


Figure 4.1: Mean values and standard error of the mean (SEM) of normalized tumor volumes for all tumors. The data is normalized to tumor volumes at Day 1. Squares indicate the mean of all the tumors prior to inclusion into the experiment, dots are the irradiated tumors and triangles are the control tumors. Days with minus (-) indicates measurements prior to radiation therapy.

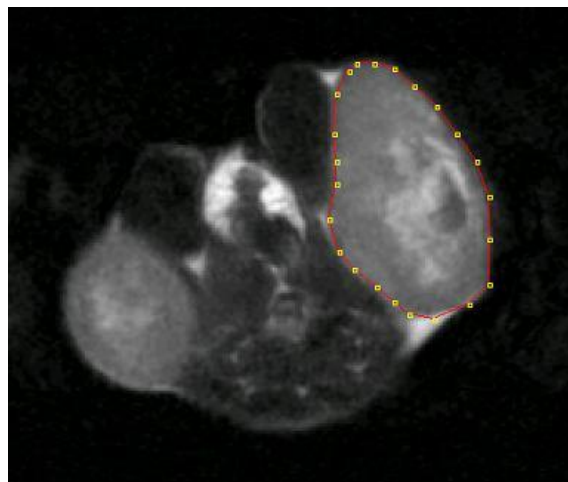


Figure 4.2: Tumor ROI was marked manually in every slice in the T_2 -weighted MR images and summed with the slice gap and slice thickness to obtain the tumor volume. The two large bright areas are the two tumors of this mice, while the bright area in the middle is the spine.

In Figure 4.2, a manually marked tumor ROI in a T_2 -weighted slice is shown. A comparison of volumes calculated from slide caliper measurements to the volumes calculated from T_2 -weighted MR images are shown in Figure 4.3. A ratio of 1 indicates equal tumor volumes calculated. By using slide caliper a little larger volume is calculated in the

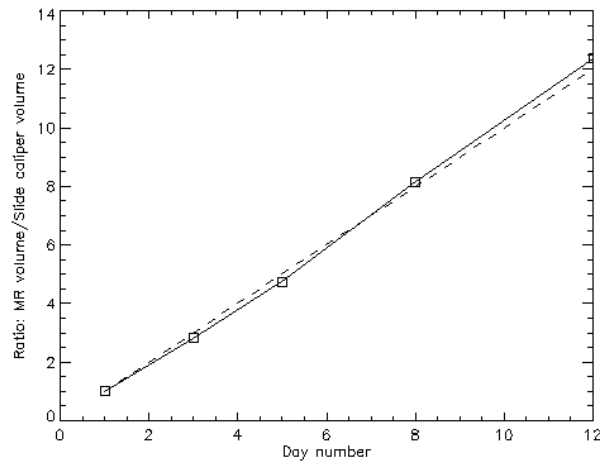


Figure 4.3: Solid line with squares shows the ratio of volume estimated from T_2 -weighted MR images to the volume calculated by slide caliper measurements for each of the five experiment days. The dashed line shows a linear curve with ratio equal to 1.

beginning of the experiment, while in the last part the volume calculated by slide caliper measurements is less than the volumes calculated in the T_2 -weighted MR images. Tumor volumes measured in T_2 -weighted MR images are listed in Table 4 in Appendix B.

4.1.3 Tumor Histology

Table 4.1 shows the extent of necrosis and fibrosis in the tumors. The stains were examined with respect to the degree of necrosis, fibrosis and viable tumor. Figure 4.4 shows a HE-stain with fibrosis, necrosis and viable cells. The median values of NF were 35.03 % at Day 1, 56.68 % at Day 3, 52.00 % at Day 5, 49.10 % at Day 8 and 54.87 % at Day 12. In Figure 4.5 the NF are shown graphically. Since there are few tumors, the data can not be considered to have a normal distribution and the tumors' NF are shown as a box-and-whiskers plot.

There were no fibrosis in the necrotic area at Day 1. After irradiation, an increase of necrosis occurred in the central part of the tumor, as can be seen from the NF at Day 3. At Day 5, the NF is reduced, but the degree of fibrosis in the necrotic area has increased. More fibrosis are observed in the stains corresponding to the outer parts of tumor, while the central part of tumor contain little fibrosis. At Day 8, there are fibrosis also in the central part of tumor, while the extent of necrosis are decreasing. The NF of the tumors at Day 8 differed with only 0.67 %. This is reflected by Figure 4.5 where the NF at Day 8 are seen as only the median value. At Day 12, the necrotic fraction is increasing again, and the presence of fibrosis is decreased. There are almost no fibrosis observed in the tumor. The only fibrosis observed are in the viable cells in the outer part of tumor.

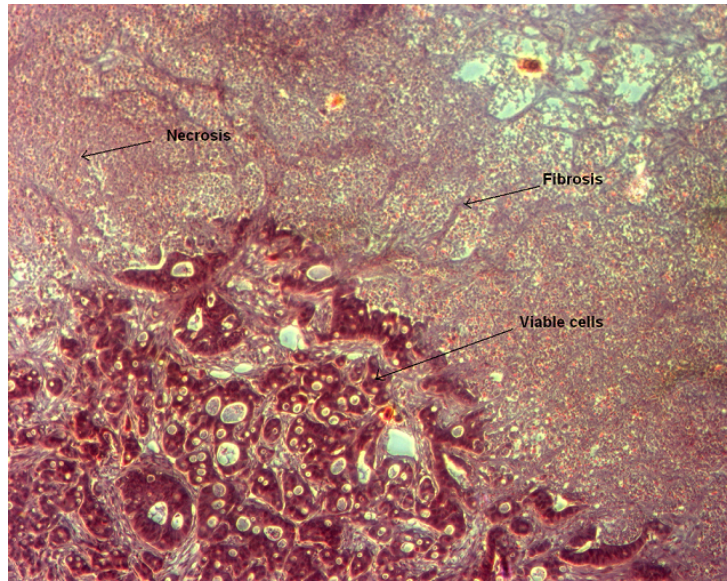


Figure 4.4: A photo of a HE-stain showing viable cells, necrosis and fibrosis in a tumor.

| Tumor No | Day of Excise | NF | Degree of Fibrosis |
|----------|---------------|---------|--------------------|
| 24 | 1 | 31.75 % | Little |
| 22 | 1 | 45.52 % | Little |
| 20 | 1 | 38.31 % | Little |
| 18 | 1 | 28.83 % | Little |
| 16 | 3 | 60.57 % | Little |
| 14 | 3 | 52.79 % | Little |
| 12 | 5 | 58.96 % | Some |
| 10 | 5 | 45.03 % | Some |
| 8 | 8 | 49.43 % | A lot |
| 6 | 8 | 48.76 % | A lot |
| 4 | 12 | 51.26 % | Little |
| 2 | 12 | 58.48 % | Little |

Table 4.1: Tumor necrotic fraction (NF) and the degree of fibrosis in tumor. NF is found by manual marking of necrotic areas in HE-stains. Fibrosis is divided into three levels corresponding to little (10 - 30 %), some (30 - 60 %), and a lot of fibrosis (60 - 100 %) in the tumor.

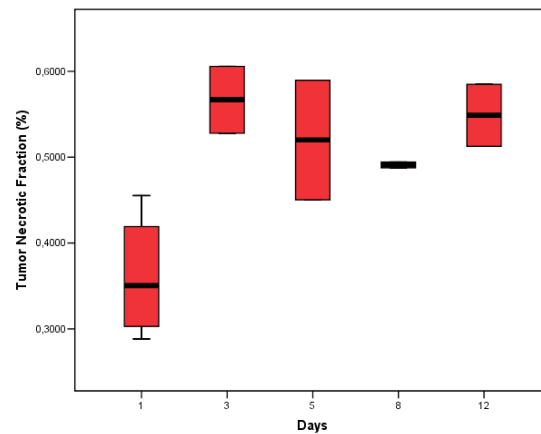


Figure 4.5: Box-and-whiskers plots (median, the whiskers indicate the 5 or 95 % quantal) of tumor necrotic fraction (NF) for each of the five days.

4.1.4 *In vivo* MR Spectroscopy

T_2 -weighted images were used for positioning the $[4 \text{ mm}]^3$ spectroscopy voxel, see Figure 4.6. A typical example of a short ($TE = 35 \text{ ms}$) and a long ($TE = 144 \text{ ms}$) echo time spectrum is illustrated in Figure 4.7. The spectra were obtained at Day 3 for one of the tumors.

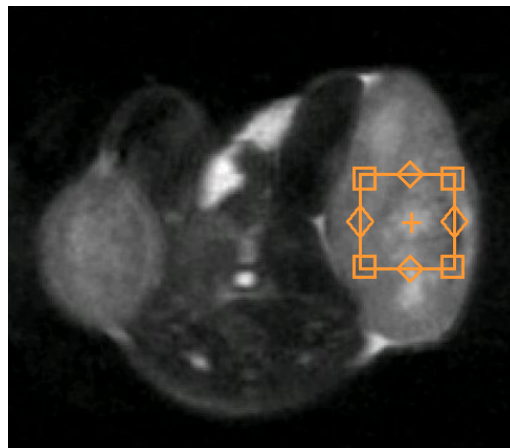


Figure 4.6: Illustration of placing of the VOI $[4 \text{ mm}]^3$ in the axial T_2 -weighted image. Spectra were obtained from this VOI.

The normalized choline ratios are changed during the 12 days of the experiment (Figure 4.8). The normalized choline ratio for all tumors at both short and long TE are listed in Table 5 in Appendix B. At short TE, the median value of the normalized choline ratios

were 0.568×10^{-3} at Day 1, 0.670×10^{-3} at Day 3, 0.296×10^{-3} at Day 5, 0.375×10^{-3} at Day 8 and 0.480×10^{-3} , at Day 12. At long TE, the median value of the normalized choline ratios were 0.182×10^{-3} at Day 1, 0.240×10^{-3} at Day 3, 0.160×10^{-3} at Day 5, 0.151×10^{-3} at Day 8 and 0.277×10^{-3} at Day 12.

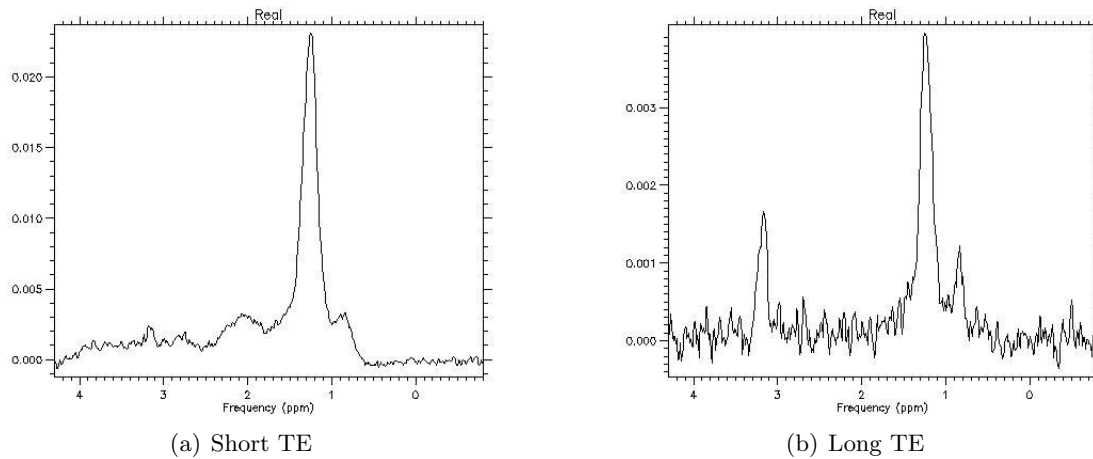


Figure 4.7: Examples of (a) short ($TE = 35$ ms) and (b) long ($TE = 144$ ms) 1H MR spectra. The spectra are from the Day 3 measurement of tumor number 1. Choline, lipid methylene and methyl are present at both TEs.

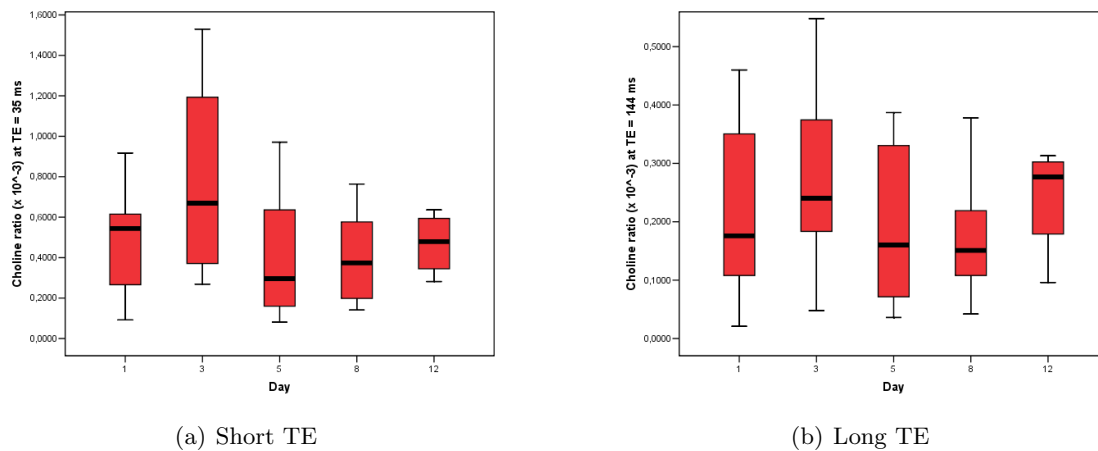


Figure 4.8: Box-and-whiskers plots (median, the whiskers indicate the 5 or 95 % quantal) of normalized choline ratios acquired at (a) $TE = 35$ ms, and (b) at $TE = 144$ ms, relative to the unsuppressed 35 ms TE water signal in the same voxel.

Histograms and QQ-plots of the choline ratios could not support the assumptions needed for normal distribution. The tumors were treated as independent samples. The non-

parametrical Mann-Whitney Wilcoxon test of the choline ratios showed no statistically significant differences between the two groups at Day 1 using a p-value of 0.05. The test gave a p-value of 0.358 for short TE and 0.159 for long TE. Figure 4.8 shows the choline ratios for the irradiated tumors.

Wilcoxon signed ranks test of the choline ratios obtained at the different experiment days showed that no differences were statistically significant for neither short TE nor long TE at the 0.05 level. At the 0.1 level there are statistically significant differences between the ratios at Day 5 and Day 12 ($p = 0.068$) for short TE and between the ratios at Day 3 and Day 8 ($p = 0.050$) for long TE.

4.1.5 Diffusion Tensor Imaging (DTI) and ADC

Figure 4.9 shows an ADC map with manually marked tumor ROI. In the figure the brightest area in the middle of the tumor is necrosis, while the small dark area is fibrosis.

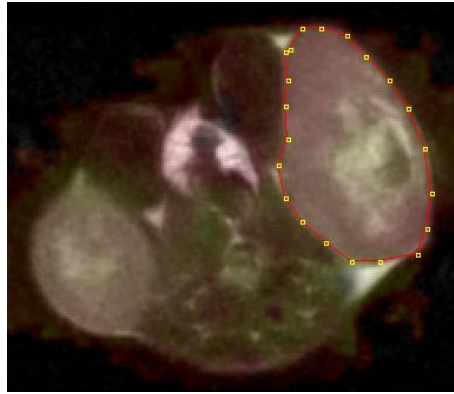


Figure 4.9: An ADC map of the mid slice of a tumor. The bright tumor region is marked by a ROI to obtain the tumor mean ADC value. The bright area shown at the opposite side is the other tumor, while the circular area in the middle is the spine.

The correct b-value was found by repeated DTI of 4 tumors with five different b-values at Day 1. The b-values were $b = 100, 200, 300, 400$ and 500 s/mm². The correct b-value are the one giving an ADC of 1.00×10^{-3} s/mm² in the tumor and 3.00×10^{-3} s/mm² in water/urine. A b-value of 300 s/mm² resulted in the ADCs closest to 1 in the four tumors, with ADCs ranging from 0.526 to 0.657×10^{-3} mm²/s at Day 1.

The calculated ADCs of the 24 tumors are listed in Table 6 in Appendix B. Figure 4.10 summarizes the tumor ADCs. The median values for ADC were 57.95×10^{-5} mm²/s at Day 1, 58.45×10^{-5} mm²/s at Day 3, 54.85×10^{-5} mm²/s at Day 5, 54.75×10^{-5} mm²/s at Day 8 and 60.95×10^{-5} mm²/s at Day 12.

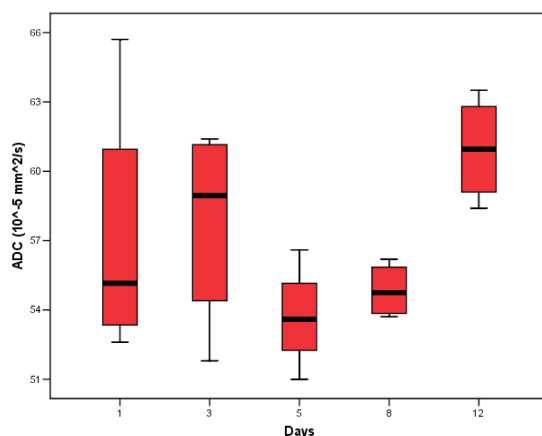


Figure 4.10: Box-and-whiskers plots (median, the whiskers indicate the 5 or 95 % quantal) of ADCs (10^{-5} mm²/s) during radiation therapy.

The ADCs were found to approximately follow a normal distribution when all tumors in both Group 1 and Group 2 were analysed. When the tumors were divided into two groups, they did not satisfy the assumptions of normal distribution. The ADCs of both Group 1 and Group 2 at Day 1 were analyzed using the non-parametrical Mann-Whitney Wilcoxon test at a p level of 0.05. The test showed no statistically significant differences between the two groups at Day 1 ($p = 0.759$).

Wilcoxon signed ranks test of the ADCs obtained at the different experiment days showed that no differences were statistically significant at the 0.05 level. At the 0.1 level there are statistically significant differences between the ratios at Day 3 and Day 5 ($p = 0.05$), Day 5 and Day 12 ($p = 0.068$) and Day 8 and Day 12 ($p = 0.068$).

4.1.6 *Ex vivo* HR-MAS MR Spectroscopy

Spectra

The HR-MAS MR spectra of tumor tissue samples gave high signal resolution, allowing almost complete separation of the different compounds in the one-dimensional spectra. In Figure 4.10 a ¹H spin-echo HR-MAS MR spectrum from control tumor 19 is shown. The 58 recognized peaks are listed in Table 4.2. The table gives both the chemical group, the chemical shift and the multiplet of each metabolite.

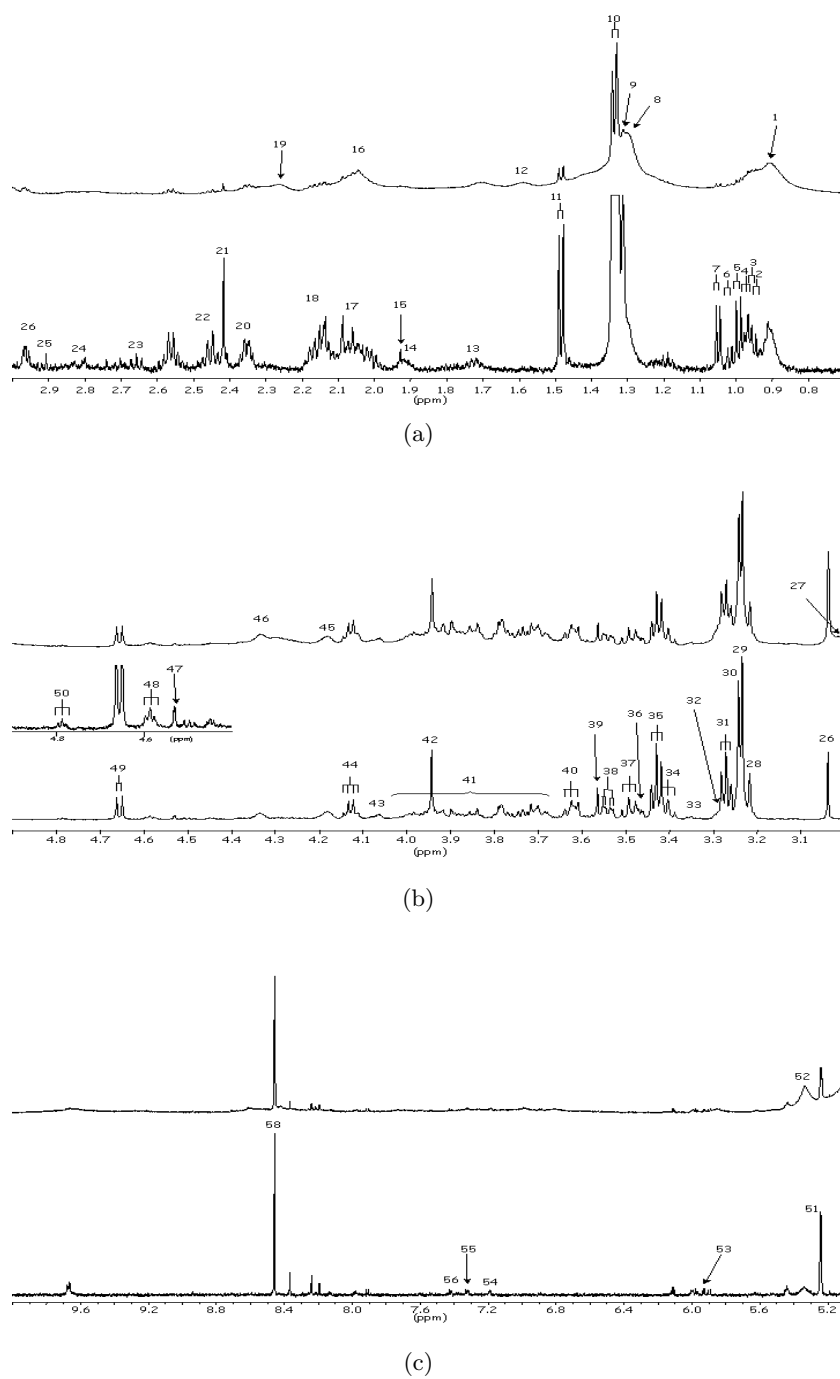


Figure 4.11: ^1H HR-MAS MR spin echo spectra of biopsy from tumor 19 (control) acquired with water suppression, showing (a) the region 3.0 - 0.7 ppm, (b) the region 4.9 - 3.0 ppm, and (c) the region 9.7 - 4.9 ppm. The assignments in the figure corresponds to the data in Table 4.2.

| Metabolite | Chemical group | Assigned number | Chemical shift (ppm) | ¹ H multiplet |
|-----------------------|---|-----------------|----------------------|--------------------------|
| Fatty acids | -CH ₃ | 1 | 0.91 | m |
| Isoleucine | δCH ₃ | 2 | 0.95 | d |
| Leucine | δ'CH ₃ | 3 | 0.96 | d |
| Leucine | δCH ₃ | 4 | 0.97 | t |
| Valine | γCH ₃ | 5 | 0.99 | d |
| Isoleucine | γCH ₃ | 6 | 1.02 | d |
| Valine | γ'CH ₃ | 7 | 1.05 | d |
| Fatty acids | -(CH ₂) _n | 8 | 1.30 | m |
| Fatty acids | -CH ₂ -CH ₃ | 9 | 1.31 | m |
| Lactate | CH ₃ | 10 | 1.33 | d |
| Alanine | CH ₃ | 11 | 1.48 | d |
| Fatty acids | -CH ₂ -CH ₂ -CO | 12 | 1.59 | m |
| Leucine | βCH ₂ | 13 | 1.72 | m |
| Isoleucine | βCH | 14 | 1.92 | m |
| Acetate | CH ₃ | 15 | 1.93 | s |
| Fatty acids | -CH=CH-CH ₂ -CH ₂ - | 16 | 2.04 | m |
| Glutamate | βCH ₂ | 17 | 2.06 | c |
| Glutamine | βCH ₂ | 18 | 2.14 | c |
| Fatty acids | -CH ₂ -CH ₂ -CO | 19 | 2.26 | m |
| Glutamate | γCH ₂ | 20 | 2.35 | c |
| Succinate | (All Hs) | 21 | 2.42 | s |
| Glutamine | γCH ₂ | 22 | 2.45 | c |
| Aspartate | βCH | 23 | 2.66 | dd |
| Aspartate | β'CH | 24 | 2.80 | dd |
| Asparagine | βCH | 25 | 2.91 | dd |
| Asparagine | β'CH | 26 | 2.96 | dd |
| Creatine | CH ₃ | 27 | 3.04 | s |
| Choline | N(CH ₃) ₃ | 28 | 3.22 | s |
| Phosphocholine | N(CH ₃) ₃ | 29 | 3.23 | s |
| Glycerophosphocholine | N(CH ₃) ₃ | 30 | 3.24 | s |
| Taurine | N-CH ₂ | 31 | 3.27 | t |
| myo-Inositol | C5H | 32 | 3.28 | t |
| scyllo-Inositol | (All Hs) | 33 | 3.35 | s |
| β-Glucose | C4H | 34 | 3.40 | t |
| Taurine | S-CH ₂ | 35 | 3.43 | t |
| α-Glucose | C3H | 36 | 3.47 | dd |
| β-Glucose | C3H | 37 | 3.49 | dd |
| myo-Inositol | C1H, C3H | 38 | 3.54 | dd |
| Glycine | αCH ₂ | 39 | 3.56 | s |
| myo-Inositol | C4H, C6H | 40 | 3.62 | dd |
| Amino acid residues | αCH | 41 | 3.65 - 4.05 | |

| | | | | |
|-----------------------------|-------------------------------------|----|------|---|
| Creatine | CH ₂ | 42 | 3.94 | s |
| myo-Inositol | C2H | 43 | 4.07 | t |
| Lactate | CH | 44 | 4.13 | q |
| Glycerol in triglycerides | $\frac{1}{2}$ CH ₂ OCOR | 45 | 4.18 | m |
| Glycerol in triglycerides | $\frac{1}{2}$ CH ₂ OCOR | 46 | 4.33 | m |
| Ascorbate | | 47 | 4.53 | d |
| Glutathione | | 48 | 4.58 | t |
| β -Glucose | C1H | 49 | 4.65 | d |
| Glutathione | | 50 | 4.79 | t |
| α -Glucose | C1H | 51 | 5.24 | d |
| Fatty acids | -CH=CH-CH₂-CH=CH- | 52 | 5.33 | m |
| Uracil | C6H, ring | 53 | 5.93 | d |
| Phenylalanine | C2H, C6H, ring | 54 | 7.19 | m |
| Phenylalanine | C4H, ring | 55 | 7.32 | m |
| Phenylalanine | C3H, C5H, ring | 56 | 7.42 | m |
| Uracil | C5H, ring | 57 | 7.91 | d |
| Formate (added with buffer) | HCOO' | 58 | 8.46 | s |

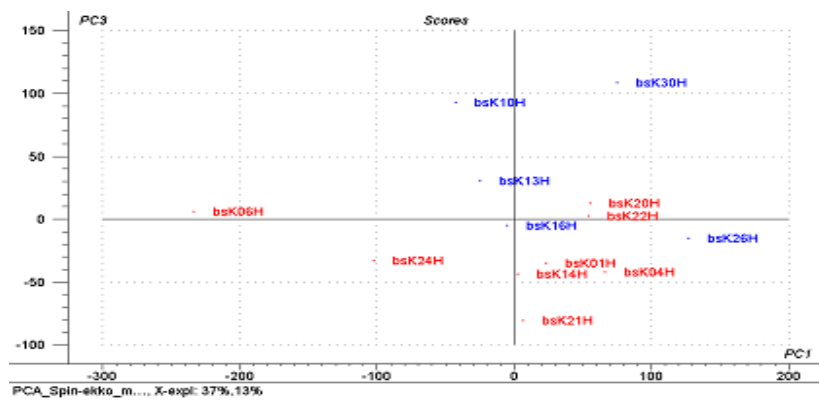
Table 4.2: ¹H chemical shift assignment on HR-MAS MR spectra of rectum cancer xenografts. Chemical shift referencing is relative to TSP. For fatty acids, the resonating group is given in bold. Peak multiplicity is given as s: singlet, d: doublet, dd: double doublet, t: triplet, q: quartet, m: multiplet or c: complex. Assigned numbers corresponds to numbering in Figure 4.11 [30].

Principal Component Analysis

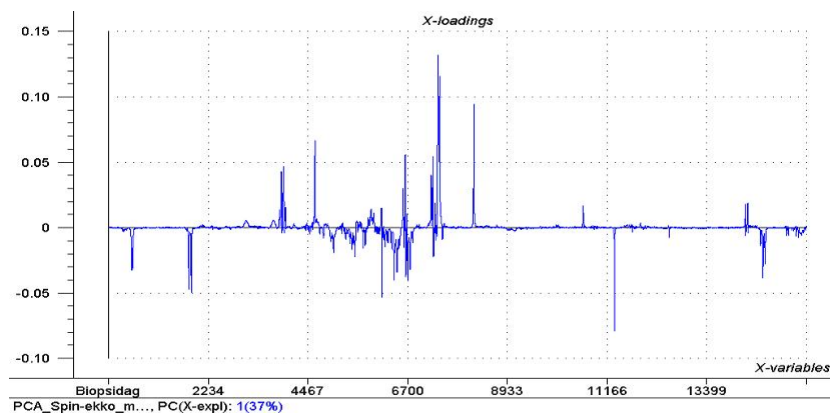
PCA was performed using both water suppressed spectra and spin-echo spectra. Inspection of different score plots against clinical parameters revealed some apparent relationships. Score values and principal components were examined for correlation to experiment groups, tumor size, results from *in vivo* spectroscopy, tumor ADCs and tissue composition.

The most noticeable connection in the spin echo spectra was found between PCA score values of the HR-MAS MR spectra and the tumor grouping (irradiated/control). In the spin echo spectra a range from 10 to 0.2 ppm was chosen. The range over the water signal (down to 4.8 ppm) and the residues of the lipid signals (at 2.8 ppm and from 1.3 ppm to 0.2 ppm) were excluded. The specter range used in PCA was described by 15 620 points. A PCA score plot and loading profile based on the spin echo spectra of the samples are shown in Figure 4.12. It is the third principal component, PC3, that determines the grouping. The loading profile of PC1 describes 37 % of the variation in the spectra, while PC3 describes 13 % of the variation.

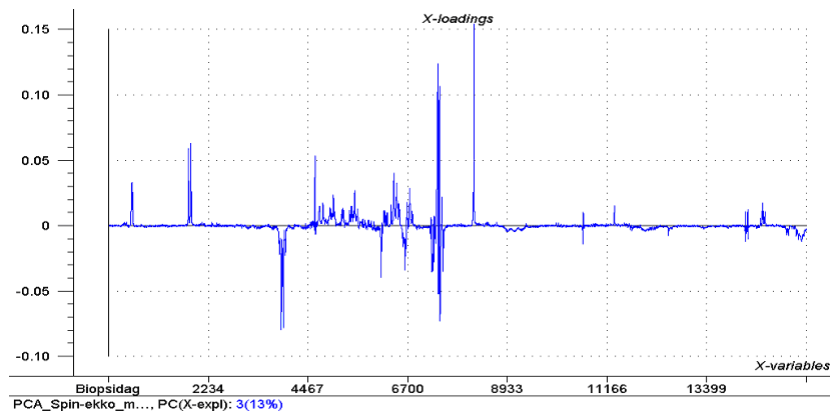
In the single-puls spectra, a connection between the PCA score values of the HR-MAS MR spectra and the necrotic fraction of the tumors are observed. In the single-puls spectra a range from 10 to 0.2 ppm was chosen. The range over the water signal (down to 4.8 ppm) was excluded. The specter range used in PCA was described by 16 185 points. A



(a) Score-plot

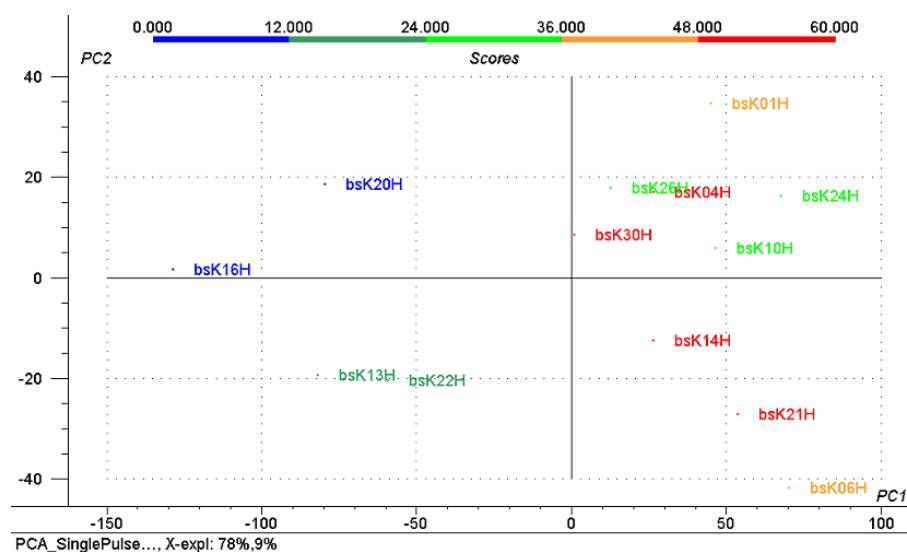


(b) Loading profile PC1

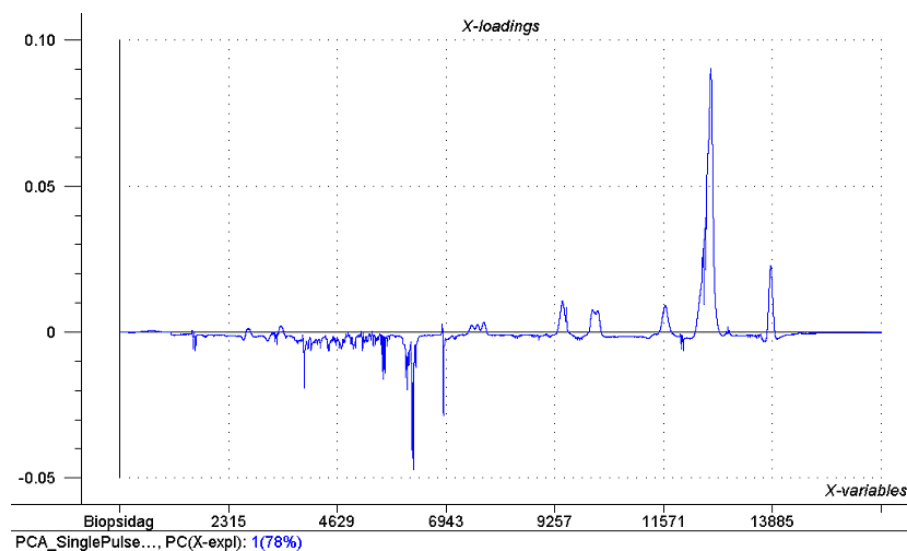


(c) Loading profile PC3

Figure 4.12: The figure shows (a) the score-plot of PC1 and PC3 for the spin-echo spectra, (b) the loading profile for PC1 and (c) the loading profile for PC3. Blue are the control tumors, red are the irradiated tumors.



(a) Score-plot



(b) Loading profile

Figure 4.13: (a) The score-plot of PC1 and PC2 for the single-pulse spectra. The coloring refers to the degree of necrotic tissue in tumor, colour scale is shown at the top. (b) The loading profile for PC1 that describes 78 % of the variation in the spectra.

PCA score plot and loading profile based on the single-pulse spectra of the samples are shown in Figure 4.13. It is the second principal component, PC2, that determines the grouping. The loading profile of PC1 describes 78 % of the variation in the spectra. PC1 is dominated by signals from lipids, mainly CH_2 .

Histology of the HR-MAS examined tumors

Examples of histological stains of tumors with and without necrosis are shown in Figure 4.14. The relative areas of normal elements, necrotic tissue and fibrous tissue for all tumors are listed in Table 4.3.

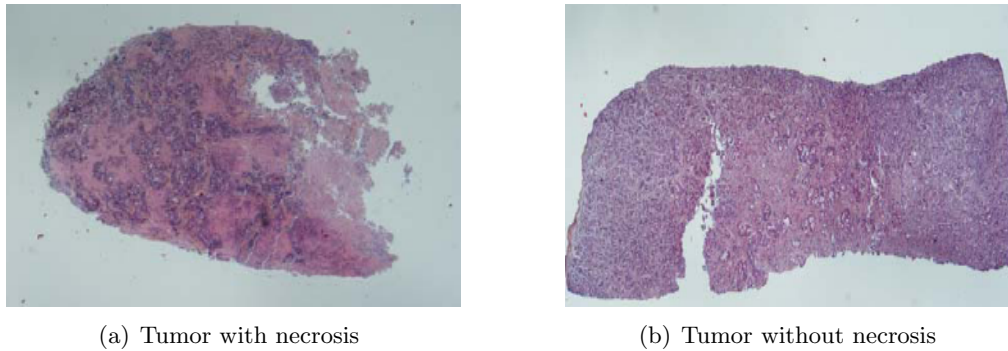


Figure 4.14: Histological preparations of (a) tumor number 13 (Group 1) and (b) tumor number 19 (Group 2). Tumor number 13 contained a lot of necrosis (60 %), while the tissue sample from tumor number 19 (control) contained no necrosis.

| Tumor no. | Tumor tissue | Necrosis | Fibrosis |
|-----------|--------------|----------|----------|
| 1 | 20 % | 20 % | 40 % |
| 3 | 40 % | 30 % | 30 % |
| 5 | 40 % | 20 % | 30 % |
| 7 | 30 % | 50 % | 20 % |
| 9 | 50 % | 40 % | 10 % |
| 11 | 30 % | 60 % | 10 % |
| 13 | 35 % | 60 % | 5 % |
| 15 | 50 % | 20 % | 30 % |
| 17 | 60 % | 30 % | 10 % |
| 19 | 90 % | - | 10 % |
| 21 | 60 % | 30 % | 10 % |
| 23 | 40 % | 50 % | 10 % |

Table 4.3: Histology of the tumors examined with HR-MAS MR spectroscopy. The histological results shows the amount of tumor tissue, necrosis and fibrosis in the tumors.

4.2 Experiment 2

Xenografts were implanted on 21 mice. 4 mice died between implantation of tumor tissue and onset of treatment. Another 3 died during the experiment, 2 of the mice in Group 2 (Day 1) and 1 of the mice in Group 3 (Day 3). The deaths caused an uneven number of mice in each group. In Group 1, one of the mice had only 1 tumor. The experiment included totally 33 tumors.

Table 4.4 shows the tumor numbers, at which day the mice were sacrificed and grouping.

| Tumor No | Day of Excise | Group |
|-------------------|---------------|-------|
| IR-1, 1 | 5 | 1 |
| IR-2 | 5* | 1 |
| IR-3, 3 | 10 | 1 |
| IR-4, 4 | 10 | 1 |
| IR-5, 5 | 5 | 1 |
| IR-C-1, C-1 | 5 | 2 |
| IR-C-2, C-2 | 5 | 2 |
| IR-C-3, C-3 | 10 | 2 |
| IR-C-4, C-4 | 1** | 2 |
| IR-C-5, C-5 | 1** | 2 |
| IR-C-OX-1, C-OX-1 | 10 | 3 |
| IR-C-OX-2, C-OX-2 | 5 | 3 |
| IR-C-OX-3, C-OX-3 | 3*** | 3 |
| IR-C-OX-4, C-OX-4 | 5 | 3 |
| IR-C-OX-5, C-OX-5 | 10 | 3 |
| IR-C-OX-6, C-OX-6 | 10 | 3 |
| IR-C-OX-7, C-OX-7 | 10 | 3 |

Table 4.4: Numbering of the 33 tumors in Experiment 2 and the different days the tumors were excised. IR = irradiated, C = Capecitabine and OX = Oxaliplatin. * Mouse 2 in group 1 had only one tumor, the tumor received irradiation. ** Mice 4 and 5 in Group 2 died the Day 1. *** Mouse 3 in Group 3 died Day 3.

4.2.1 Chemoradiation Therapy

Radiation Therapy

The mean radiation dose to the tumors was 14.51 Gy (range; 9.505 - 16.950 Gy). This indicates that the tumors were placed a little farther out than 1.5 cm into the radiation field. Table 7 in Appendix B lists the radiation doses for all the tumors.

Chemotherapy

All the three groups experienced body weight loss during the experiment. All weights are listed in Table 8 in Appendix B. Group 3 mice receiving both Oxaliplatin, Capecitabine and irradiation had the largest weight loss, Group 2 had a little less than group 3, while Group 1 had a much lower weight loss than the two other groups. In Group 1 the maximum body weight loss was 3.56 % (Day 4), in Group 2 9.23 % (Day 4) and in Group 3 a weightloss of 10.36 % (Day 4) was observed. The largest weight loss of a single mouse was 14.64 %. The largest weight loss was observed at Day 4 for all the groups. The mice recovered when chemotherapy ended and at Day 10 Group 1 had a body weight of + 2.17 % compared to Day 1, Group 2 had - 2.02 % compared to Day 1 and Group 3 had a weight of + 1.90 % compared than Day 1. Figure 4.15 shows the body weight loss in percent compared to Day 1 for all the groups. The body weights were normal distributed and the figure shows the mean value and standard error of the mean (SEM).

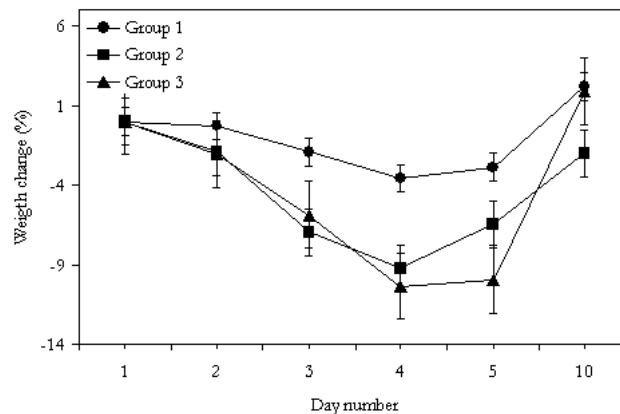


Figure 4.15: Body weight loss for the three groups. The weight loss is given in percent compared to body weight at Day 1. Dots indicate group 1, squares group 2 and triangles group 3.

4.2.2 Tumor Growth Curves

Tumor growth curves for both (a) slide caliper measurements and (b) volumes calculated from T_2 -weighted MR images are shown in Figure 4.16. The tumor volumes were found to approximately follow a normal distribution and the mean volume and corresponding standard error of the mean (SEM) are shown in Figure 4.1. All measurements are normalized to the volumes found at Day 1. Tumor volumes before inclusion to experiment are listed in Table 9 in Appendix B, while the tumor volumes after inclusion are given in Table 10 in Appendix B. Tumor volumes measured from T_2 -weighted MR images are listed in Table 11 in Appendix B.

In Figure 4.17 and 4.18 the irradiated and controls in the three groups are shown separately. The caliper volumes contains volumes from 18 days prior to onset of treatment, while the MR image calculations are from Day 1. Both volume calculations were performed until the mice were sacrificed. The tumor volumes were normal distributed and the curve shows the mean value and standard error of the mean (SEM). All measurements are normalized to Day 1.

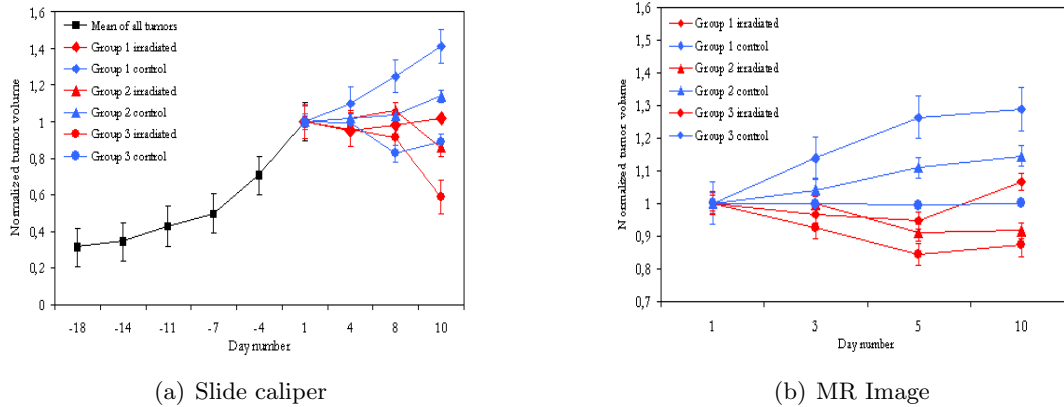


Figure 4.16: Mean values and standard error of the mean (SEM) of normalized tumor volume for all tumors in the three groups. (a) Volumes calculated after slide caliper measurements, (b) Volumes calculated from T_2 -weighted MR-images. The data in both figures are normalized to Day 1. Black squares are mean of all the tumors before inclusion in the experiment. Red indicates radiated tumors, while blue are control tumors that not recieved irradiation. In red and blue, diamonds are group 1, triangles are group 2 and dots are group 3.

In Group 3, treatment with both irradiation, Oxaliplatin and Capecitabine resulted in shrinking of tumor size. The control tumors in Group 3 did also show this effect in a small shrinking or stop of tumor growth. Group 2 showed a small shrinking in tumor size for the irradiated tumors. The control tumors in Group 2 continued to grow, but at a slower growth rate than the controls in Group 1. In Group 1, the irradiated tumors stopped growing, while the control tumors continued to grow after a small drop from Day 1 to Day 3.

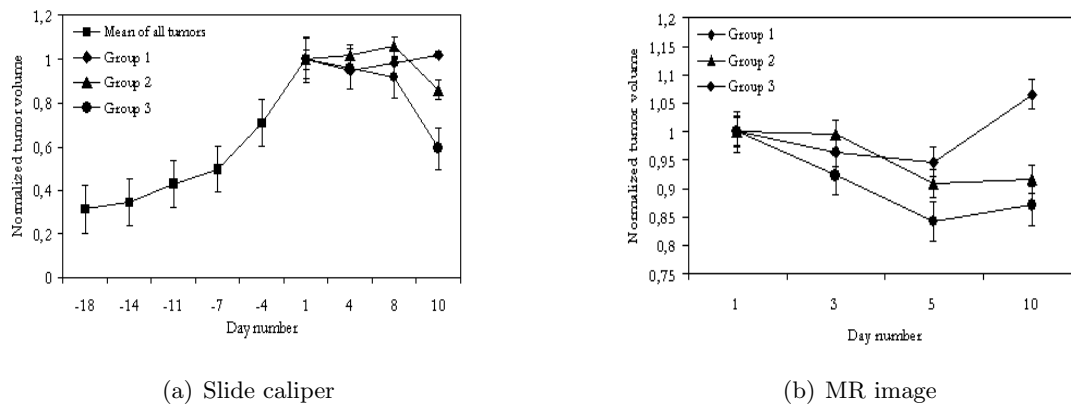


Figure 4.17: Mean values and standard error of the mean (SEM) of normalized tumor volume for the irradiated tumors in the three groups. (a) Volumes calculated after slide caliper measurements, (b) Volumes calculated from T_2 -weighted MR-images. The data in both figures are normalized to Day 1. Black squares are mean of all the tumors before inclusion in the experiment. Red indicates radiated tumors, while blue are control tumors that not received irradiation. In red and blue, diamonds are group 1, triangles are group 2 and dots are group 3.

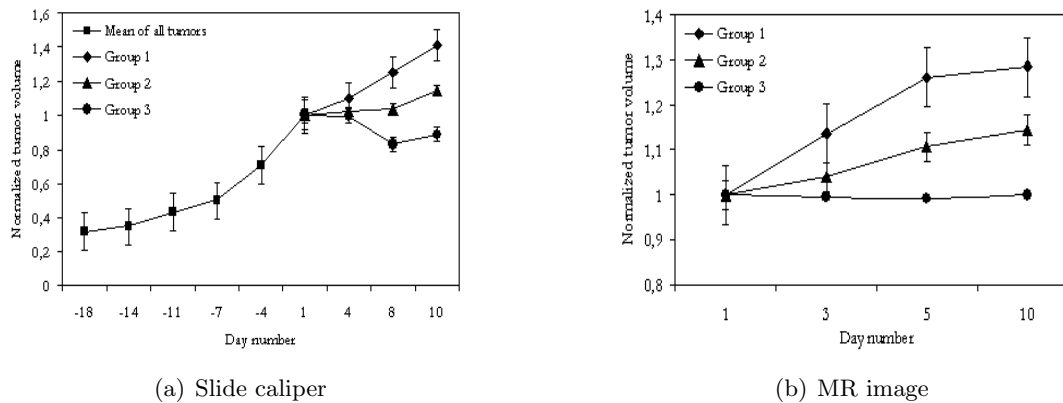


Figure 4.18: Mean values and standard error of the mean (SEM) of normalized tumor volume for the control tumors in the three groups. (a) Volumes calculated after slide caliper measurements, (b) Volumes calculated from T_2 -weighted MR-images. The data in both figures are normalized to Day 1. Black squares are mean of all the tumors before inclusion in the experiment. Red indicates radiated tumors, while blue are control tumors that not received irradiation. In red and blue, diamonds are group 1, triangles are group 2 and dots are group 3.

4.2.3 Tumor Histology

The histological results are shown in Table 4.5. All tumors receiving treatment, both chemotherapy and radiation therapy showed high amounts of necrosis in the tumors. Fibrosis was observed in all tumors receiving treatment. The number of values in each group is too low to visualize the results graphically.

| Tumor No | Day of Excise | NF | Degree of Fibrosis |
|-----------|---------------|---------|--------------------|
| 1 | 5 | 56.60 % | Little |
| 3 | 10 | 0 | - |
| 4 | 10 | 42.29 % | Little |
| 5 | 5 | 13.88 % | Little |
| IR-1 | 5 | 57.16 % | A lot |
| IR-2 | 5 | 59.70 % | A lot |
| IR-3 | 10 | 64.04 % | A lot |
| IR-4 | 10 | 45.60 % | Some |
| IR-5 | 5 | 39.10 % | A lot |
| C-1 | 5 | 63.91 % | A lot |
| C-2 | 5 | 58.64 % | A lot |
| C-3 | 10 | 77.60 % | Some |
| IR-C-1 | 5 | 73.97 % | A lot |
| IR-C-2 | 5 | 58.81 % | A lot |
| IR-C-3 | 10 | 25.41 % | Some |
| C-OX-1 | 10 | 64.35 % | Some |
| C-OX-2 | 5 | 97.82 % | Some |
| C-OX-4 | 5 | 44.87 % | A lot |
| C-OX-5 | 10 | 49.62 % | Some |
| C-OX-6 | 10 | 36.60 % | Some |
| C-OX-7 | 10 | 54.92 % | Some |
| IR-C-OX-1 | 10 | 66.42 % | Some |
| IR-C-OX-2 | 5 | 82.34 % | A lot |
| IR-C-OX-4 | 5 | 45.72 % | A lot |
| IR-C-OX-5 | 10 | 56.70 % | A lot |
| IR-C-OX-6 | 10 | 60.77 % | Some |
| IR-C-OX-7 | 10 | 61.40 % | Some |

Table 4.5: Necrotic fraction and the degree of fibrosis in tumor. NF is found by manual delineation of necrotic areas in HE-stains. Fibrosis is divided into three levels: little (10 - 30 %), some (30 - 60 %), and a lot of fibrosis (60 - 100 %) in the tumor respectively. Tumor number 3 contained only viable cells.

4.2.4 *In vivo* MR Spectroscopy

The tumors in Experiment 2 were smaller than the tumors in Experiment 1, leading to difficulties in placing the $4 \times 4 \times 4$ mm³ voxel for acquiring MR spectra. MR spectra were not achieved at all for some tumors, while for several other tumors, the treatment response could not be monitored since the tumor volume decreased after treatment. Do to the few data obtained, the *in vivo* MR Spectroscopy results are left out in Experiment 2.

4.2.5 Diffusion Tensor Imaging (DTI) and ADC

The calculated ADCs of the 33 tumors are listed in Table 12 in Appendix B. Statistically, the irradiated and control tumors from the same mouse are related samples. Since there were few mice in each group, the results were not tested for statistical significancies. The resulting ADCs at the four experiment days are visualized as box-and-whiskers plots in Figure 4.19.

The ADC of the tumors that were irradiated (Group 1) increases at Day 3, followed by a decrease at Day 5 and another increase at Day 10. The ADCs of the control tumors in Group 1 remains constant during all experiment days. In Group 2 the ADCs increased at Day 3 for both irradiated and control tumors followed by a small decrease at Day 5. The control tumor continued to decrease while the irradiated tumor increased. The ADC of Day 10 consist of only one irradiated and one control tumor since two mice died in this group. The same tendency as in Group 2 exist in Group 3, except for Day 10. The Day 10 ADC increased a lot for both irradiated and control tumors.

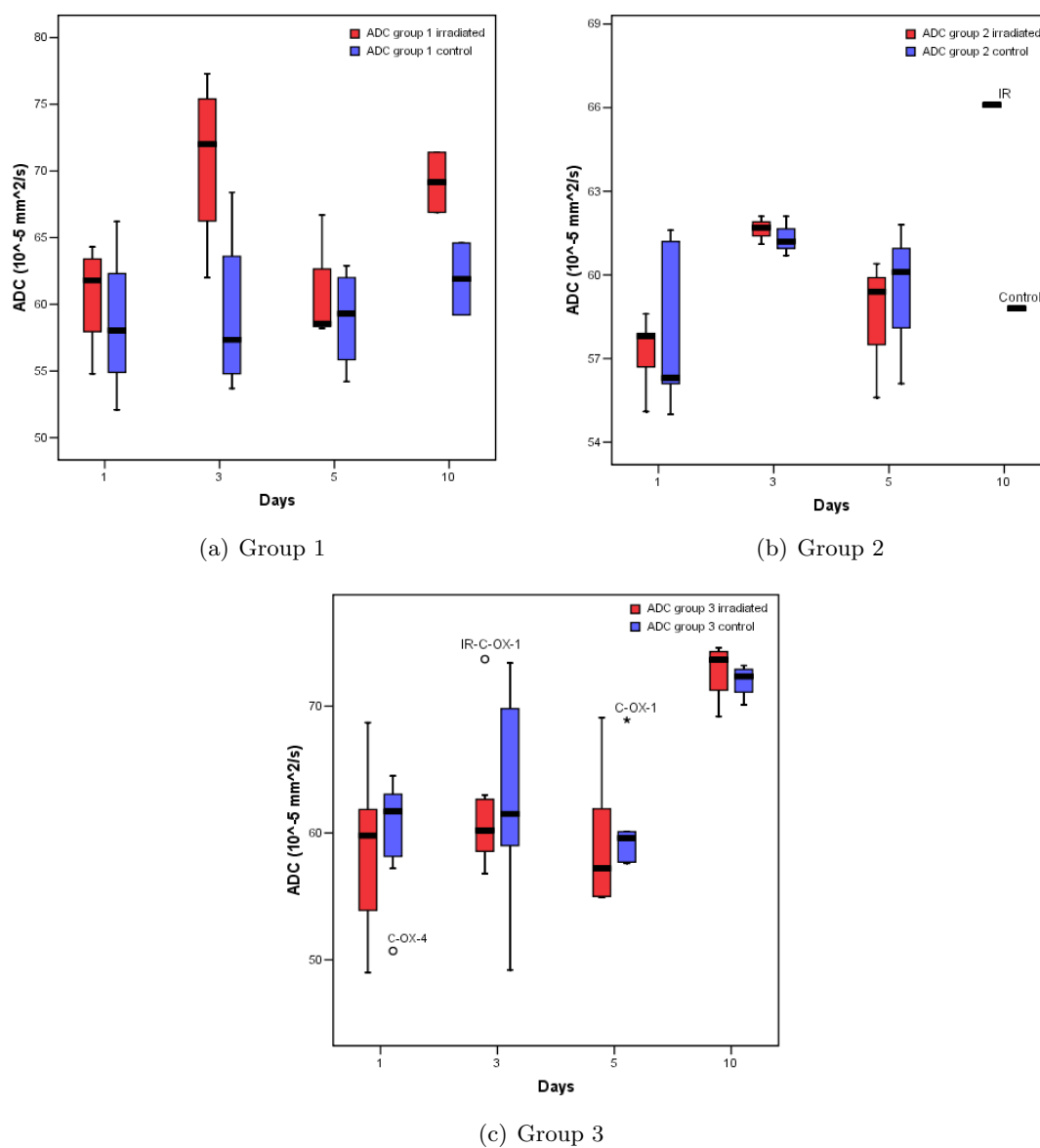


Figure 4.19: Box-and-whiskers plot (median, the whiskers indicate the 5 or 95 % quantal) of ADCs ($10^{-5} \text{ mm}^2/\text{s}$) of the tumors (irradiated and controls) in Group 1, 2 and 3. Red indicates irradiated tumors, blue are control tumors. In (b) the ADC of Day 10 consist of only one irradiated- and one control since two mice died in this group. In (c) three outliers can be seen (C-OX-4 at Day 1, IR-C-OX-1 at Day 3 and C-OX-1 at Day 5.)

Chapter 5

Discussion

5.1 Tumor Model

One of the benefits using xenografts as tumor model is that the xenografts highly preserve the characteristic histology of the original human tumor. Additionally, the xenografts response to radiation- and chemotherapy is similar to the response of the original human tumor. After inoculation of tumor tissue, the defect immune defence of these nude mice accelerates the tumor metabolism. The metabolism in mice occurs 5 times faster than in humans [21]. The tumor metabolism due to radiation- and chemotherapy can be intercepted within few days after onset of treatment.

HT29 xenografts have a high tumor take, which is also proved in this work where nearly all tumor tissues continued to grow after inoculation. This is one of the reasons of choosing this cell line. Additionally, the cell line is well-characterized and used in several other experiments.

In Experiment 1, tumors were included into the experiment by selecting the mice with large enough tumors into the treatment group. The controls were included into the experiment as the last parallel. This implies that the controls had tumors growing slower than the tumors in the treatment group. The process of selecting the tumors should have been done randomly. However, statistical analyses of the groups resulted in no statistically significant differences between the groups at Day 1. From this it can be assumed that this error, if any, is small. By selecting the tumors reaching a tumor size of 10 mm at the shortest axis to inclusion into the experiments, a selection is already performed, since this selection not were performed randomly. In the first experiment all 24 tumors are assumed to be independent. Since the mice had tumors on both flanks, these tumors are not completely independent. The assumption of independence is made since all tumors in Group 1 recieved identical treatment.

Anaesthesia influence a mouse by lowering the body temperature. Mice in Experiment 2 were sedated daily during radiation- and chemotherapy and MR acquisitions, leading to a lower consumption of food and water since the mice were sleeping more than usual. This could also have influenced the body weight loss. The weight loss is expected to be approximately equal for all groups.

The tumors in these experiments are not orthotropic, but chosen in order to make the experiments practically feasible. To obtain orthotropic tumors the tumor tissue should have been placed in the intestinals of the mouse, achieving the proper conditions with respect to circulation and the tumors original environment. Orthotropic tumors would have made it impossible to monitor the tumor volume by a slide caliper. *In vivo* MR spectroscopy could not have been performed as the size of the intestinals restricts the maximum tumor size and hence the ability to achieve a volume large enough for placement of a VOI.

5.2 Radiation- and Chemotherapy

Three mice died during Experiment 2. The two deaths at Day 1 and the one at Day 3 could arise from cytotoxicity of the chemotherapy drugs. It was performed a post-mortem of one of the mice to see if Capecitabine (administered by gavage) was in the lungs or in the bronchi. The autopsy showed that Capecitabine was in the stomach as intended. The deaths could also stem from i.v. injection of Oxaliplatin, anaesthesia or bacterias. The mice were taken out of sterile environments during radiation therapy and MR examinations, leading to exposure of bacterias. Since nude mice lacks immune defence, they are easily influenced and this could have lead to these deaths. Since there were no mortality in Experiment 1, it is expected that the additional stress associated with combined chemoradiation therapy causes the deaths in Experiment 2. If the 3 deaths are expected to arise from toxicity, the total toxic mortality was 17.6 %.

Prior to Experiment 2 there was investigated which doses of Capecitabine and Oxaliplatin that was recommended for this kind of experiments. The doses of Capecitabine and Oxaliplatin, as well as the type of placebo and how to administer the drugs, were chosen with respect to the results obtained by other groups ([24], [25], [48], [49], [50], [51], [52]). The maximum tolerable doses were not exceeded.

Several causes could have induced the deaths prior to the experiments. Compared to female mice, fighting is part of the male mice's nature, leading to bloody injuries that might result in death. After inoculation of tumor tissue, the mice were taken out from the animal department at Rikshospitalet-Radiumhospitalet HF and kept at a less sterile place during the experiments. This place did satisfy the conditions of temperature, air humidity and hygiene, but the mice could have been exposed for bacterias during this relocation.

In Experiment 2 there is a question whether the right tumor also received irradiation. The measuring of radiation doses with the phantom prior to the experiment revealed that a dose of 0.28 Gy was given 1.8 cm outside the field, and 5.10 Gy was given at the corner of the radiation field. No change in ADC of the control tumors in Group 1 in Experiment 2 after radiation therapy (Figure 4.19a) indicates that there are little scattered radiation to this tumor. This can also be seen from the growth curves (Figure 4.16), where the control tumors in Group 1 continued to grow.

Since the mice were sacrificed within few days there can not be known whether the tumors receiving combined chemotherapy would completely vanish or if they would start to grow again when treatment ceased. To compare the tumors from all groups at the same days, the mice were sacrificed on the selected days in order to the maximum allowed size of a tumor (20 mm) on the flank of a mouse. This size was reached shortly after start of experiment for control tumors, and a mouse can not be followed much longer than about 12 days after start of the experiment when the size at inclusion is 10 mm.

5.3 Calculation of Tumor Volume

All volume calculations, both with slide caliper and delineation of tumor areas in T₂-weighted MR images, were performed of the same person. There exist an uncertainty in that the mice were measured both alive and sedated. This uncertainty might be about ± 1 mm.

Experiment 1

Compared to the controls (Group 2), tumor growth was inhibited by irradiation (Group 1), with a mean tumor volume of 54.87 % as compared to the controls at Day 12. Since all mice were sacrificed only 12 days after start of radiation therapy, tumor regression growth (TRG) could not be observed. The tumor volumes calculated by slide caliper were compared to volumes calculated from T₂-weighted MR images (Figure 4.3). The deviation from a linear curve can be explained by Equation 3.1. The equation is based on the assumption that the height is equal to the tumor shortest axis. If the height is less than the shortest axis, a too large volume is estimated, and vice versa the volume of a tumor with height larger than the shortest axis will be estimated less than the real volume. The tumors are expanding outwards in the beginning, before they start to expand upwards.

Experiment 2

Oxaliplatin and Capecitabine resulted in shrinking of tumor size (Figure 4.16). The control tumors in Group 3 did also show this effect in a small shrinking or stop of tumor growth. Since the tumors in Group 2 not shrunked that much, this effect might arise from Oxaliplatin. Group 2 showed a small shrinking in tumor size for the irradiated tumors. The control tumors in Group 2 continued to grow, but at a slower growth rate than the

controls in Group 1. In Group 1, the irradiated tumors stopped growing, while the control tumors continued to grow after a small drop from Day 1 to Day 3. This was also shown in the growth curves in Experiment 1.

The tumors showed a reduction of tumor volume during therapy. Although individual tumor volumes strongly varied, it is interesting to note that the average tumor volume showed a clear decrease for both ionizing radiation alone and combined with radiosensitizing drugs. The results showed that radiation therapy alone reveals the largest effect on tumor reduction. Tumor volumes from Group 3 in Experiment 2 suggests that there might be a synergetic effect when chemotherapy includes both Capecitabine and Oxaliplatin.

The partial volume effect in MR images may overestimate tumor volume measured by MR. This effect arise from the selection of slices. By selecting a slice thickness of e.g. 1 mm, the outer part of tumor will not fill the outermost slice. This is reflected in an overestimation of tumor volume since the slice thickness is part of the volume estimation (Equation 3.5).

5.4 Histology

In Experiment 2, each tumor was cut in three pieces, giving samples for all analysis. In Experiment 1 only left-sided tumors were taken out for histology. The benefit of using the whole tumor for histological HE-staining, as in Experiment 1, is a more precise estimation of the tumor necrotic fraction. The results from the histological analyses in Experiment 1 was in accordance with the results from the MR acquisitions, revealing that analyzing 8 histological stains of the whole tumor provides correct outcome.

To minimize the variance between observers, all histological analyses were performed of the same observer. There exists an uncertainty in the calculation of necrotic fraction in the stains. Both a microscope and a PC for manual delineation of ROIs were used. The uncertainty relies on the ability to find exactly the same areas in the scanned stains at the PC (with lower resolution) as the ones found by using the microscope.

The main challenge in determination of the necrotic fractions was small holes without biological material in the histological stains. These small holes without biological material are most likely caused by damages performed to the stains in the preparation process. The damages can be due to stretching of the histological stains in the water bath or cutting the stains with a knife that was not perfectly sharp. In the majority of the stains the holes were small and surrounded by necrosis. These holes do most likely consist of necrosis, and they were therefore considered to be necrosis in the analyses. In some histological stains, there were small holes in between the viable cells. These holes might stem from viable cells and were considered to be viable cells. Three stains from three different tumors contained large holes without biological material, resulting in difficulties in obtaining necrotic

fractions. These stains were excluded in the analyses. These stains were all in Experiment 1 and the tumor necrotic fraction (NF) for these tumors was found on the basis of 7 stains instead of 8 stains. This might have lead to an error in calculation of NF in these tumors. The assessment of holes in biological material involved a certain use of rough calculations. These evaluations implied a certain uncertainty in determination of necrotic fraction. For the majority of tumors this uncertainty is assumed to be minimal.

Experiment 1

Typical of rapidly growing adenocarcinomas, the large, well developed HT29 tumors had necrotic centers and appeared to be poorly vascularized. This can be seen from the tumor necrotic fraction (NF) at Day 1. All tumors showed ingrowth of fibrosis in the viable tumor area. Fibrosis is unlike necrosis contained throughout the entire tumor. Hence the degree of fibrosis were divided into three levels; a little fibrosis (10 - 30 %), some fibrosis (30 - 60 %), and a lot of fibrosis in the tumor (60 - 100 %).

At Day 1, there was no fibrosis in the necrotic areas. After irradiation at Day 2, the necrosis increased dramatically in the central part of the tumor, as can be seen of the NF at Day 3 (Table 4.1, Figure 4.5). This reflects the radiation-induced effects. Fibrosis starts developing from outside and into the tumor. At Day 5, the NF shows a decrease at the same time as the degree of fibrosis in the necrotic area increases. More fibrosis are observed in the stains corresponding to the outer parts of the tumors, while the central part of tumor contain little fibrosis. The growth of fibrosis is stimulated by the increased amount of necrosis. At Day 8, there are fibrosis present also in the central part of tumor, while the extent of necrosis is decreasing. At Day 12, the long-term effect of radiation therapy occurs and the necrotic fraction is increasing again, and the presence of fibrosis is decreasing. At Day 12, the only fibrosis observed was in the viable cells in the outer part of tumor.

Experiment 2

In this experiment only one stain of each tumor was prepared. This stain correspond to the central slice used for apparent diffusion coefficient (ADC) calculation. The selection of one slice overestimates the tumor necrotic fraction since the necrosis are concentrated in the central part of the tumors.

For all treated tumors, large amounts of necrosis were observed in the histological stains (Table 4.5). For all tumors except the control tumors in Group 1, fibrosis were observed. This fibrotic response was present in all tumors, as a response to tumor necrosis. As there were few tumors in each group there was not possible to find any significant differences between the amount of necrosis and fibrosis in the tumors at the different days. The result showed that both tumors receiving only chemotherapy and tumors receiving combined chemoradiation therapy had high amounts of necrosis in tumor and that this had stimulated the growth of fibrosis in the necrotic areas of tumor.

Tumor necrotic fraction based on a single central slice is assumed to be less reliable than

the tumor necrotic fraction calculated from 8 slices covering the whole tumor. Future experiments should be performed using more than one stain and stains from all tumors. Additionally, the distance between the slice used for ADC calculation compared to where the HE-stain of the tumor were taken from represents an uncertainty.

5.5 *In vivo* MR Spectroscopy

Biochemical information from *in vivo* MRS must arise from well-localized regions in order to be valuable. *In vivo* MRS is most often based on volume selective pulse sequences. First, MR images with a good visualization of the anatomy and pathology of interest are obtained. A volume of interest (VOI) is placed in the desired region and spectra from single or multiple volume elements are acquired. The most common pulse sequences for volume localization are STEAM and PRESS. The PRESS technique has a better SNR and is less sensitive to motion and diffusion, while using STEAM it is possible to obtain spectra with shorter echo times.

When using a longer echo time, better visualization of the chemical structures with longer relaxation times is achieved. From the spectra obtained in this work (e.g. Figure 4.7), the choline peak at 3.21 ppm was observed in all spectra with low peak SNR at short TE, and higher SNR at long TE. Other metabolites observed in all spectra include the lipid methylene peak at 1.23 ppm and methyl at 0.91 ppm, both peaks having larger area than choline. The creatine peaks at 3.04 and 3.94 ppm can usually not be seen at short TE, but was seen at long TE in some spectra. Around 2.00 ppm there was observed a group of peaks in the short TE spectra that corresponds to several amino acids, among them glutamate at 2.06 ppm and glutamine at 2.14 ppm. In addition, myo-Inositol at 3.54/3.62 ppm and glucose at 3.40/3.47/3.49 ppm were observed in some spectra.

Choline is related to tumor growth and the results in this work shows elevated levels of choline metabolites in the tumors at Day 1. The change in choline ratios obtained in Experiment 1 shows the same change as the tumor necrotic fraction, suggesting that the normalized choline ratio reflects the tumor response to irradiation. In the spectra, choline compounds could be observed at 3.21 ppm. *Ex vivo* HR-MAS MRS showed that phosphocholine gives the major contribution to this signal (Peak number 29 in Figure 4.11b). The choline signal changes during radiation therapy, giving a reduction in choline signal compared to prior to onset of treatment. Few of the differences were statistically significant, but there exist a tendency. These tendencies might become statistically significant if the experiment contains more tumors, recommending that the experiment should be repeated to see if these significancies are achieved.

There are several approaches for analyzing MRS data. In this work, metabolite peak ratios are calculated and related to the unsuppressed water signal at 4.7 ppm, acquired at TE = 35 ms. The relative difference between signals has often been estimated by calculat-

ing peak areas or peak intensities and comparing ratios. This method has been used for evaluating the *in vivo* MRS data in this work. In monitoring brain diseases, the ratio of choline to creatine are used as a standard. The level of creatine in the brain has shown to be constant ([53], [54], [55]), yielding information about the alteration in choline with this ratio. In colorectal tumors, the water content has shown to be fairly constant. In this work all water peak areas ranged from 25.96 to 71.55 mm². About 90 % of the water peak areas was in the range 30 mm² to 40 mm². This reveals that using water as an internal standard should give reliable results for the means of monitoring tumor response by assessing the normalized choline ratio. The ratios are used to compare changes occurring in a series of spectra. A more accurate ratio of signals would be obtained by comparing areas of signals using curve-fitting routines since line broadening effects then are reduced.

In this work, manual marking of three peaks (choline, lipid methylene and methyl) in addition to water was performed in all spectra. In addition, areas of other pronounced peaks were found in some spectra. It should be examined whether the results would have been better by using an automated peak selection where for example all peaks with a SNR larger than two times the noise were selected. The manual option was used since the peaks were easily identified in the spectra.

The VOI is not placed exactly in the same position during the repeated MR examinations due to change of tumor geometry and size. The relative experimental uncertainty increased with increasing tumor volume in most instances. In decreasing tumors (during treatment), it was difficult to place the VOI, resulting in poor spectra due to contribution from fat and tissue outside the tumor.

Typical *in vivo* ¹H MR spectra demonstrate relative broad lines. However, signals from lipids, choline compounds, creatine and some amino acids, were easy to assign. Sample heterogeneity will influence the MRS results. With a large amount of fatty tissue present, triglycerides from such tissue will make a significant contribution to the signals in the spectra. Thus, not only inter-tumor variation but also sample heterogeneity will contribute to variation in the metabolic concentrations determined by *in vivo* ¹H MRS.

Treatment induced changes in the ¹H MR spectroscopy of experimental tumors have been studied by several investigators ([56], [35], [40]). But, there exist no literature, known to the author, that describes the use of HT29 xenografts in *in vivo* ¹H MR spectroscopy.

5.6 Diffusion Tensor Imaging and ADC

In this work, DW-MRI was studied as a possible means to monitor the response of tumor tissue during only radiation therapy and combined chemoradiation therapy at a cellular level. The hypothesis was that changes of the cellular structure within tumor tissue, due to its interaction with ionizing radiation and radiosensitizing drugs, should manifest as

changes of the corresponding ADC coefficient. This coefficient reflects the changes of the molecular water mobility.

Ionizing radiation leads to a change of vessel permeability for water resulting in an increase of extracellular volume (ECV), i.e. to an interstitial edema, which are observed as an increased ADC compared to the pre-therapy value. As tumor cells get damaged during the course of radiation- and chemoradiation therapy, the integrity of cell membranes is compromised. With a failure of the $\text{Na}^+\text{-K}^+\text{-ATPase}$ pump, a cytotoxic edema will form due to a shift of water from the ECV to ICV, which is supposed to be accompanied by an overall decrease in the observed ADC values. Later, as a consequence of the cytotoxic edema, cell death will occur, which will lead to an increase of the interstitial space due to cell loss. These effects are expected to increase the mobility of water molecules within the damaged tissue [11], which should lead to another increase in ADC values [41], [57], [9], [43].

In accordance with these arguments, a shift of the ADC value to higher ADC was observed from Day 1 to Day 3 in both Experiment 1 and Experiment 2 (Figure 4.10 and Figure 4.19). This is expected to show an early response to treatment as has also been reported in other studies [8], [43]. Increased ADC fit the above described formation of an interstitial edema at the beginning of therapy. Since this increase of ADC was statistically significant in Experiment 1, this behavior might be a predictor of therapy outcome. After Day 3, it was observed a clear decrease in ADC which corresponds to the formation of cytotoxic edema. Later on, cell death should occur characterized by a renewed increase of ADC. This increase was observed from Day 8 to Day 12 in Experiment 1 and from Day 5 to Day 10 in Experiment 2. As with the choline ratios, some of the differences were statistically significant, but to obtain more statistically significant differences, the experiments should be repeated.

In diffusion weighted imaging, the magnetic resonance signal arises from both intracellular and extracellular compartments. Due to the higher content of relatively impermeable impeding barriers like cell and nuclear membranes, organelles, cytoskeleton and matrix fibers, lower ADCs are reported in the intracellular compartment. Thus, ADC changes are thought to reflect changes of the ECV/ICV ratio [10]. The high tumor ADC is correlated with a high necrotic fraction, mainly because of the increased extracellular water. The same effect has also been shown by other groups [57], [43]. The increase in ADC at Day 12 do most likely stem from the elevated level of necrosis, but can also indicate radiation-induced inflammation. These results shows that the median tumor water ADC is correlated with the degree of tumor response after radiation- and chemoradiation therapy. Dzik-Jurasz et Al. [9], showed that the mean tumor ADC acts as a surrogate marker of tumor necrosis.

In Experiment 2, the ADCs of the control tumors in Group 1 remained constant throughout the 10 experiment days. The ADCs of the irradiated tumors in Group 1 showed the same tendency as the tumors in Group 1 in Experiment 1. This tendency was also seen

from the results in Group 2 in Experiment 2. But Group 2 contained only 3 three mice. The results showed an increase in ADC at Day 3 for the irradiated tumors. A decrease is seen at Day 5 and a high increase at Day 10 due to the elevated level of necrosis. The control tumor ADC remains low at Day 10. The difference between Day 10 and Day 5 in Group 2 compared to Group 1 might arise from the treatment with Capecitabine in Group 2. This is also in accordance with the tumor volume curves (Figure 4.17) where it is shown that the irradiated tumors in Group 2 had a larger growth inhibition than irradiated tumors in Group 1.

It was a large variability between the parallels of the irradiated tumors in Group 3 at Day 3. Some of the tumors had a large increase in ADC while others decreased. This is reflected by only a small increase of the median ADC, and not a large increase as might be expected. It could be that the short-term effect occurs faster due to the combined chemoradiation therapy and that the growth of fibrosis has already started, resulting in a lower ADC. But the long-term effect is intercepted at Day 10 with a large increase in ADC. The difference between combined chemoradiation therapy compared to only radiation therapy is the percentual increases/decreases between the days.

Technical difficulties affecting measurements should be considered. Signal attenuation of DW-MRI depends on incoherent molecular displacements of water molecules. Apart from molecular diffusion processes, this effect is also influenced by all other kinds of motion during data acquisition. However, the mice were sleeping during the examination and breathing artefacts were almost entirely avoided since the mouse was placed with the body weight over the tumor (Figure 3.6a). Even if gross organ movements can be excluded, one still has to consider the effects of capillary microcirculation on measured ADC values. In *in vivo* tissues, the reported ADCs have often shown higher values than expected. This has been attributed to the influence of perfusion on signal attenuation in DW-MRI [58].

Until recently, diffusion tensor images have been acquired by single-shot echo-planar imaging, EPI, methods achieving a good SNR with a low RF power deposition. EPI utilizes gradient rephasing, which results in spatial distortions from magnetic susceptibility effects, especially near air interfaces. In addition, EPI suffers from geometric image distortions created by significant eddy currents arising from the large magnetic field gradients used. Overall, these EPI related artefacts have detrimental effect on the image quality. Recent studies has demonstrated the feasibility of using radiofrequency, RF, or RF-refocused single-shot fast spin echo, SSFSE-based diffusion MR acquisitions, providing images without the significant degree of spatial distortions [59].

5.7 *Ex vivo* HR-MAS MR Spectroscopy

Ex vivo HR-MAS MRS provide spectra with narrow lines and thereby biochemical information of numerous metabolites (Figure 4.11). Line broadening due to intermolecular

interactions in solid material is reduced by spinning the sample about its own axis inclined 54.7° to the magnetic field. 58 metabolites in the tumor tissue samples were assigned in the spectra using *ex vivo* HR-MAS MRS.

Cheng et. Al [7], showed that HR-MAS spectra of tissue samples from breast cancer patients correlates well with histopathological examinations. In this work, *ex vivo* ^1H HR-MAS spectra were acquired from 12 HT29 xenografts. The correlation between necrosis and HR-MAS spectra are also found in this work (Figure 4.13). The results from the single-puls spectra indicate that there is a higher content of principal component 1 in species with a high degree of necrosis. These results suggests that there is a correlation between *ex vivo* and *in vivo* MR data as both methods revealed a connection with the amount of necrosis in tumor.

The most noticeable connection in the spin echo spectra was found between PCA score values of the HR-MAS MR spectra and the tumor grouping (irradiated/control). The HR-MAS MRS experiments contained only 12 tumors and there is a need for repeating the experiments with a larger group of samples.

Multivariate Analysis

MRS data consist of large amounts of information. The benefit of using multivariate analysis is that the whole spectrum or selected parts can be used as input to the analysis, as opposed to conventional analysis where single areas or peak ratios are used. With multivariate analysis, several variables can be compared and co-variations can be found and taken into account in one analysis, not by analyzing one parameter at the time. Such analysis has been performed on MR spectra from tissue samples by several groups [39], [40], [60].

MR data can be analyzed using peak areas as input or spectral raw data. Standard principal component analysis (PCA) and various neural network analysis techniques use digitized spectra where defined regions of chemical shifts and corresponding signal intensities are used as input. The neural networks are trained to recognize patterns in the spectra based on a set of spectra with a known classification. Assuming that the training set is large enough and contain information that differ the groups, the network can then classify unknown spectra.

5.8 Clinical Relevance

The results from the experiments in this work suggests that the non-invasive *in vivo* methods MRS and DW-MRI can be used for monitoring of treatment response of HT29 xenografts in mice.

A limiting factor in *in vivo* MR spectroscopy is the size of the VOI. In the clinical scanner

used in this work this VOI has to be at least $4 \times 4 \times 4 \text{ mm}^3$. This limitation is due to the gradients in the MR scanner. In *in vivo* MR spectroscopy the signal loss in a patient is large compared to the losses in a mouse in the mouse coil and a VOI of around $20 \times 20 \times 20 \text{ mm}^3$ is needed to obtain sufficient signal. The geometry of rectal tumors is often complex, yielding difficulties in placement of a VOI of the desired size. In contrast to xenografts on mice, the tumors in patients are surrounded by fat and intestinals, that will be reflected in the spectra. The treatment response is also difficult to monitor as the tumor shrinks due to treatment, and the placement of the voxel varies from examination to examination. However, the method has potential in other types of cancer, for example breast, where the tumor are more compact and homogeneous.

However, by performing acquisitions with several excitations, the size of the VOI can be lowered and still obtain enough signal to achieve acceptable spectra. With patients, this method is not used since acquisition with several excitations results in more artefacts due to patient movement, breathing and flow. Using fixed tumors where artefacts due to breathing and flow are absent, several excitations can be used to achieve spectra from smaller VOIs.

The aim of monitoring the treatment response in tumors by non-invasive methods is the ability to individualize the treatment to each patient. Taken into account the LARC-RRP study, the purpose is to identify factors that can provide information about the individual tumor and hence be able to adjust the treatment during the course of treatment. With respect to ADCs there might be that different tumors demonstrate different ADC correlated with the treatment response. This has been suggested by Dzik-Jurasz et Al. [9], in a study where the ADC were measured before and after chemotherapy and chemoradiation therapy in 14 patients with locally advanced colorectal cancer. They found a strong negative correlation between mean pre-treatment tumor ADC and percentage size change of tumors after chemotherapy and chemoradiation therapy. They suggested that the persistence of low ADC in responders after chemotherapy could represent loss of a non-viable fraction of the treated tumor. In the LARC-RRP study, *in vivo* MR examinations are performed prior to treatment and after 6 Gy of radiation therapy. If factors that can reveal information about the tumor are intercepted at the examination after 6 Gy, the treatment for the patients in the study can be changed, possibly giving an increased prognosis for survival.

The hope is that *in vivo* MR examinations could give information of tumor and the histological conditions of tumor resulting in improved treatment. Intensity-modulated radiation therapy implies that there can be given a heterogeneous radiation dose to tumor, giving less radiation to the necrotic parts while proliferating, viable cells are receiving more radiation. The total radiation dose and the side effects are the same as in a homogeneous dose. By using this method it is expected an improved outcome of cancer treatment resulting in increased survival.

The findings in this work suggest that *in vivo* MRS and DW-MRI could yield clinically

important information for the evaluation of treatment response of rectal cancer. The approach needs validation and a prospective study of reproducibility of patients with clinically advanced rectal cancer.

5.9 Suggestions for Further Work

Both experiments performed in this work were pilot studies. The experiments were executed with a minimum of mice due to the 3 R's (Replacement, Refinement and Reduction) in execution of animal experiments. This lead to problems in acquiring enough data to statistical analyses. To verify (or eventually disprove) the results obtained in this work, they have to be repeated. Then the amount of data is sufficient to perform complete statistical analysis.

The overall aim of prediciting and monitoring the early treatment response is to provide means for individualized cancer treatment. Experimental studies should therefore investigate whether tumor response to a given treatment correlates with the alteration in tumor metabolism and diffusion. In clinical practice, dose escalation radiation therapy protocols for selected groups of patients represents the first step towards individualized radiation therapy. This may contribute to increased local tumor control in cancer patients, but may additionally increase late toxicity. In the future, *in vivo* ^1H MRS and DW-MRI may become useful tools in stratifying patients entering such dose escalation protocols.

It has been recognized that the aim of radiation therapy not is to deliver a homogeneous radiation dose to the tumor. Regions in the tumor may require higher doses than safely can be delivered to the entire volume. *In vivo* MRS and DW-MRI may provide necessary spatial information about tumor physiological factors that influence radiosensitivity. Thus, the methods may hence identify what regions of the tumor that require higher radiation doses. The usefulness of this approach can be tested in an experimental study where higher radiation doses are given to regions of the tumor according to these methods.

In an evidence-based review [61], it was estimated that the implementation of novel strategies - currently at the research level - into clinical radiation oncology, could potentially increase the 5-year survival of cancer patients with loco-regional failure with 10 %. It is therefore reasonable to believe that further research in radiation oncology will contribute significantly to the improved outcome of cancer treatment in the coming decades.

New insights in molecular signatures of radiation response may lead to new strategies for radiation therapy. It is expected that combining current radiation regimes with molecular targeting will significantly improve loco-regional response and thus survival [62].

Chapter 6

Conclusion

This work has shown that *in vivo* magnetic resonance spectroscopy (MRS) and diffusion-weighted magnetic resonance imaging (DW-MRI) are feasible for non-invasive monitoring of treatment response in an experimental tumor model.

From *in vivo* MRS data, tumor growth was assessed by monitoring the level of choline in tumor. The normalized choline ratio changed in accordance with the amount of necrosis in tumor. A correlation of *ex vivo* and *in vivo* MRS exist as the principal component analysis (PCA) of high resolution *ex vivo* magic angle spinning (HR-MAS) MR spectroscopy also showed a connection with necrosis in tumor.

In vivo DW-MRI showed alterations of the molecular water mobility due to interaction with ionizing radiation and radiosensitizing drugs. This was reflected by changes of the corresponding apparent diffusion coefficient (ADC), which agreed with the change in tumor necrotic fraction.

These methods were tested on an experimental tumor model using HT29 xenografts and further validations needs to be done. These initial data encourage further studies to prove the possible value of *in vivo* non-invasive MRS and DW-MRI in evaluation of therapy outcome.

Bibliography

- [1] Kreftforeningen. <http://www.kreftforeningen.no>.
- [2] W.G. Negendank. Studies of human body tumors by MRS - a review. *NMR Biomed*, 5(303-324), 1992.
- [3] J.L. Griffin and J.P. Shockcor. Metabolic profiles of cancer cells. *Nature*, 4(551-561), 2004.
- [4] C.V. Dang and G.L. Semenza. Oncogenic alterations of metabolism. *Trends Biochem Sci*, 24(68-72), 1999.
- [5] J. Ruiz-Cabello and J.S. Cohen. Phospholipid metabolites as indicators of cancer cell function. *NMR Biomed*, 5(226-233), 1992.
- [6] A. Dzik Jurasz, P.S. Murphy, M. George, T. Prock, D.J. Collins, I. Swift, M.O. Leach, and I.J. Rowland. Human rectal adenocarcinoma: demonstration of ^1H -MR spectra *in vivo* at 1.5 T. *J Magn Reson Imaging*, 47(809-811), 2002.
- [7] L.L. Cheng, I.W. Chang, and R.G. Gonzalez. Evaluating human breast ductal carcinomas with high-resolution magic-angle spinning proton magnetic resonance spectroscopy. *J Magn Reson Imaging*, 135(194-202), 1998.
- [8] T.L. Chenevert, L.D. Stegman, and J.M. Taylor et Al. Diffusion magnetic resonance imaging: an early surrogate marker of therapeutic efficacy in brain tumors. *J Natl Cancer Inst*, 92(2029-2036), 2000.
- [9] A. Dzik Jurasz, C. Domenig, M. George, J. Wolber, A. Padhani, G. Brown, and S. Doran. Diffusion MRI for prediction of response of rectal cancer to chemoradiation. *The Lancet*, Vol 360, 2002.
- [10] A. Szafer, J. Zhong, and J.C. Gore. Theoretical model for water diffusion in tissues. *Magn Reson Med*, 33(697-712), 1995.
- [11] H. Lyng, O. Haraldseth, and E.K. Rofstad. Measurement of cell density and necrotic fraction in human melanoma xenografts by diffusion weighted magnetic resonance imaging. *Magn Reson Med*, 43(828-836), 2000.
- [12] D. Le Bihan and R. Turner. Molecular diffusion, tissue microdynamics and microstructure. *NMR Biomed*, 8(375-386), 1995.

- [13] M. Eis, T. Els, and M. Hoehn-Berlage. High resolution quantitative relaxation and diffusion MRI of three different experimental brain tumors in rat. *Magn Reson Med*, 34(835-844), 1995.
- [14] D.M. Parkin, F. Bray, J. Ferlay, and P. Pisani. Estimating the world cancer burden: Globocan 2000. *Int. J. Cancer*, 94(153-156), 2001.
- [15] B. Alberts, D. Bray, J. Lewis, M. Raff, and J.D. Watson K. Roberts. *Molecular Biology of the Cell*. Garland Publishing, 1998.
- [16] D. Hanahan and R.A. Weinberg. The hallmarks of cancer. *Cell*, 100(57-70), 2000.
- [17] Cancer in Norway 2004. Cancer Registry of Norway. http://www.kreftregisteret.no/forekomst_og_overlevelse_2004/kreft_i_norge_2004web.pdf.
- [18] J.E. Husband and R.H. Reznick. *Imaging in Oncology*. Taylor & Francis, 2004.
- [19] R.J. Heald, B.J. Moran, R.D.H. Ryall, R. Sexton, and J.K. MacFarlane. The Basingstoke experience of Total Mesorectal Excision, 1978-1997. *Archives of Surgery*, 133(894-899), 1998.
- [20] J.M. Berg, J.L. Tymoczko, and L. Stryer. *Biochemistry*. W.H. Freeman and Company, 2001.
- [21] E.J. Hall. *Radiobiology for the Radiologist*. J.B. Lippincott Company, 1994.
- [22] Cancer Facts and Figures 2003. American Cancer Society. <http://www.cancer.org>.
- [23] Y. Tsukamoto, Y. Kato, M. Ura, I. Horii, T. Ishikawa, H. Ishitsuka, and Y. Sugiyama. Investigation of 5-FU disposition after oral administration of Capecitabine, a triple-prodrug of 5-FU, using a physiologically based pharmacokinetic model in a human cancer xenograft model: Comparison of the simulated 5-FU exposures in the tumor tissue between human and xenograft model. *Biopharmaceutics & Drug Disposition*, 22(1-14), 2001.
- [24] E. Raymond, S.G. Chaney, A. Taamma, and E. Cvitkovic. Oxaliplatin: A review of preclinical and clinical studies. *Annals of Oncology*, 9(1053-1071), 1998.
- [25] A. Cividalli, F. Ceciarelli, E. Livdi, P. Altavista, G. Cruciani, P. Marhchetti, and D.T. Danesi. Radiosensitization by oxaliplatin in a mouse adenocarcinoma: influence of treatment schedule. *Int J. Radiation Oncology Biol. Phys*, 52(1092-1098), 2002.
- [26] Wikipedia. <http://www.wikipedia.org>.
- [27] F. Podo. Tumour phospholipid metabolism. *NMR Biomed*, 12(413-439), 1999.
- [28] J. Ruiz Cabello and J.S. Cohen. Phospholipid metabolites as indicators of cancer cell function. *NMR Biomed*, 12(226-233), 1992.
- [29] C. Westbrook and C. Kaut. *MRI in Practice*. Blackwell Science Ltd., 1998.

- [30] R.A. de Graaf. *In vivo NMR Spectroscopy, Principles and Techniques*. John Wiley & Sons, 2002.
- [31] R.H. Hashemi and W.G. Bradley Jr. *MRI The Basics*. Williams and Wilkins, 1997.
- [32] S. Webb. *The Physics of Medical Imaging*. Institute of Physics Publishing Ltd, 2002.
- [33] B.A.J. Angelsen. *Forelesningsnotater TTK4160/TTK4165*. Emantec, 2000.
- [34] T. Seierstad and B. Høvik. Construction and characterization of a new transmit-receive capacitive overlap coil for imaging of small animals and objects in a clinical whole-body scanner at 1.5 T. *In progress*.
- [35] N.R. Jagannathan. Functional and pathophysiological study of disease processes in humans and animal systems: Role of magnetic resonance imaging and *in vivo* MR spectroscopy. *Current Science*, 86(42-61), 2004.
- [36] I.J. Bakken, T. Skjetne, I.S. Gribbestad, and K.A. Kvistad. *In vivo* magnetic resonance spectroscopy. *Tidsskrift for Den norske lægeforening*, 122(1365-1368), 2002.
- [37] E.R. Andrew. *Magic Angle Spinning, Encyclopedia of Nuclear Magnetic Resonance*. Wiley, Chichester, 1996.
- [38] W. El Deredy. Pattern recognition approaches in biomedical and clinical magnetic resonance spectroscopy: A review. *NMR Biomed*, 10(99-124), 1997.
- [39] G. Hagberg. From magnetic resonance spectroscopy to classification of tumors. A review of pattern recognition methods. *NMR Biomed*, 11(148-156), 1998.
- [40] M.C. Preul, Z. Caramanos, R. Leblanc, J.G. Villemure, and D.L. Arnold. Using pattern analysis of *in vivo* proton MRSI data to improve the diagnosis and surgical management of patients with brain tumors. *NMR Biomed*, 11(192-200), 1998.
- [41] C. Kremser, W. Judmaier, P. Hein, J. Griebel, P. Lukas, and A.F. DeVries. Preliminary results on the influence of chemoradiation on apparent diffusion coefficients of primary rectal carcinoma measured by magnetic resonance imaging. *Strahlentherapie und Onkologie*, 9(641-649), 2003.
- [42] P.A. Hein, C. Kremser, W. Judmaier, J. Griebel, K.P. Pfeiffer, A. Kreczy, E.B. Hug, P. Lukas, and A.F. DeVries. Diffusion-weighted magnetic resonance imaging for monitoring diffusion changes in rectal carcinoma during combined, preoperative chemoradiation: preliminary results of a prospective study. *Eur J Radiol*, 45(214-222), 2003.
- [43] L. Lemaire, F.A. Howe, L.M. Rodrigues, and J.R. Griffiths. Assessment of induced rat mammary tumour response to chemotherapy using the apparent diffusion coefficient of tissue water as determined by diffusion-weighted ^1H -NMR spectroscopy *in vivo*. *MAGMA*, 8(20-26), 1999.
- [44] F.M. Khan. *The Physics of Radiation Therapy*. Lippincott Williams and Wilkins, 1994.

- [45] Nordic Ice Medical. <http://www.nordicicemedical.com>.
- [46] Hammamatsu Phottonics. <http://www.hpj.co.jp/Eng/products/SYSE/aquaE.htm>.
- [47] SPSS. <http://www.spss.com>.
- [48] S. Guichard, S. Arnould, I. Hennebelte, R. Bugat, and P. Canal. Combination of oxaliplatin and irinotecan on human colon cancer cell lines. activity *in vitro* and *in vivo*. *Anti-Cancer Drugs*, 12(741-751), 2001.
- [49] C. Louvet, A.M. Coudray, C. Tournigand, S. Prevost, E. Raymond, A. de Gramont, M. Chazard, and C. Gespach. Synergistic antitumoral activity of combined UFT, folinic acid and oxaliplatin against human colorectal HT29 cell xenografts in athymic nude mice. *Anti-Cancer Drugs*, 11(579-582), 2000.
- [50] D. Balin-Gauthier, J.P. Delord, P. Rochaix, V. Mallard, F. Thomas, I. Hennebelle, R. Bugat, P. Canal, and C. Allal. *In vivo* and *in vitro* antitumor activity of oxaliplatin in combination with cetuximab in human colorectal tumor cell lines expressing different levels of EGFR. *Cancer Chemother Pharmacol*, 57(709-718), 2005.
- [51] D. Simpson, C. Dunn, M. Curran, and K.L. Goa. Oxaliplatin: A review of its use in combination therapy for advanced metastatic colorectal cancer. *Drugs*, 63(2127-2156), 2003.
- [52] F.O. Kaori, M. Yanagisawa, F. Sekiguchi, and Y. Tanaka. Antitumor activity of erlotinib in combination with capecitabine in human tumor xenograft models. *Cancer Chemother Pharmacol*, 57(693-702), 2006.
- [53] T. Hammen, H. Stefan, and B. Tomandl. The role of clinical *in vivo* ^1H -MR spectroscopy in the evaluation of epilepsies. *Spectroscopy*, 16(297-306), 2002.
- [54] M. Hund-Georgiadis, D.G. Norris, T. Guthke, and D.Y. von Cramon. Characterization of cerebral small vessel disease by proton spectroscopy and morphological magnetic resonance. *Cerebrovasc Dis*, 12(82-90), 2001.
- [55] Y.I. Chung, L.G. Rider, J.D. Bell, R.M. Summers, L.S. Zemel, R.M. Rennebohm, M.H. Passo, J. Hicks, F.W. Miller, and D.L. Scott. Muscle metabolites, detected in urine by proton spectroscopy, correlated with disease damage in juvenile idiopathic inflammatory myopathies. *Arthritis Care & Research*, 53(565-570), 2005.
- [56] P.E. Sijens, H.K. Wijrdeman, M.A. Moerland, C.J. Bakker, J.W. Vermeulen, and P.R. Luyten. Human breast cancer *in vivo*: H-1 and P-31 MR spectroscopy at 1.5 T. *Radiology*, 169(615-620), 1988.
- [57] A.M. Herneth, S. Guccione, and M. Bednarski. Apparent diffusion coefficient: a quantitative parameter for *in vivo* tumor characterization. *European Journal of Radiology*, 45(208-213), 2003.
- [58] C. Harriet, M.D. Thoeny, F. de Keyzer, C. Boesch, and R. Hermans. Diffusion-


weighted imaging of the parotid gland: Influence of the choice of b-values on the apparent diffusion coefficient value. *J Magn Reson Imaging*, 20(786-790), 2004.

- [59] D. Xu, R.G. Henry, P. Mukherjee, L. Carvajal, S.P. Miller, A.J. Barkovich, and D.B. Vigneron. Single-shot fast spin-echo diffusion tensor imaging of the brain and spine with head and phased array coils at 1.5 T and 3.0 T. *Magnetic Resonance Imaging*, 22(751-759), 2004.
- [60] R.L. Somorjai, B. Dolenko, A.K. Nikulin, N. Pizzi, G. Scarth, P. Zhilkin, W. Halliday, D. Fewer, N. Hill, I. Ross, M. West, I.C. Smith, S.M. Donnely, A.C. Kuesel, and K.M. Briere. Classification of ^1H MR spectra of human brain neoplasms: the influence of processing and computerized consensus diagnosis on classification accuracy. *J Magn Reson Imaging*, 6(437-444), 1996.
- [61] U. Ringborg et Al. The Swedish council on technology assessment in health care (SBU) systematic overview of radiotherapy for cancer including a prospective survey of radiotherapy practice in Sweden 2001 - summary and conclusions. *Acta Oncol*, 42(357-365), 2003.
- [62] A.C. Von Eschenbach. A vision for the national cancer program in the United States. *Nat Rev Cancer*, 4(820-828), 2004.

Appendix A

The signed application forms to 'Forsøksdyrutvalget' for both experiments are enclosed. Two different experiments were performed on the mice in the first experiment. Svetlana Stoknes did bioimpedance measurements of the tumors at the same days as MR acquisitions were performed.

The application form of Experiment 1 comes first, followed by the application form to Experiment 2.

| | | | | | | | |
|--|--|----------------------|-------------|-------------|----------------------|-------------|------------|
|  | Forsøksdyrutvalget, P.b. 8147 Dep, 0033 Oslo Telefon / Telefax: 23216584 / 22856501 e-post: fdu@dvrehelsetilsynet.no www.fdu.no | Utvalgets ref.: | | | | | |
| | SKJEMA TIL BRUK VED SØKNAD OM TILLATELSE TIL Å UTFØRE FORSØK MED DYR. (Eksempel på utfylling: Se www.fdu.no) | | | | | | |
| Type søknad: <table border="1" style="display: inline-table; margin-left: 20px;"> <tr> <td>Nytt forsøk</td> <td>Pilotforsøk</td> <td>Videreføring/endring</td> <td>Blokksøknad</td> <td>Feltforsøk</td> </tr> </table> | | | Nytt forsøk | Pilotforsøk | Videreføring/endring | Blokksøknad | Feltforsøk |
| Nytt forsøk | Pilotforsøk | Videreføring/endring | Blokksøknad | Feltforsøk | | | |

Til bruk for ansvarshavende ved forsøksdyravdelingen:

Feltforsøk: Angi, så godt som mulig, sted/område hvor forsøket skal gjennomføres

| | |
|---|----------------------------|
| Navn på institusjon hvor forsøket er planlagt gjennomført: | Avdelingens nr.: 32 |
| Ansvarshavende: Lena Kjempengren | Avdelingens refereransnr.: |
| Adresse: Det Norske Radiumhospital, Dyreavdelingen Montebello | 102-06 |
| Postnummer: 0310 Sted: Oslo | Telefon: 22 93 56 45 |
| e-postadresse: lenak@ulrik.uio.no | Telefax: 22 93 56 44 |

| | | | |
|---|---|--|---|
| Type forsøk (A-F): E | Brukes anestesi/analgesi? Ja Nei | Start (måned/år): 02/06 | Slutt (måned/år): 06/06 |
| Art og type forsøksdyr*: GBNIH nude mus | Antall dyr 20 | Antall dyr ved gjenbruk, jfr. forskriftens § 15: 0 | Er søknaden helt eller delvis fortrolig? Ja Nei |
| Er lignende forsøk utført tidligere ved avdelingen? Ja Nei | Er lignende forsøk utført tidligere av forskeren? Ja Nei | Er prosjektleders kompetanse iht. Landbruksdepts krav? Ja Nei | |

EK-statistikk (fylles også ut for feltforsøk):

| | | | | |
|---------------------|-------------------------|-------------------------|-------------------------|----------------------------|
| Tab. 1 (kilde): 1.1 | Tab. 2 (formål): 2.1 | Tab. 3 (utdyper 2.4): - | Tab. 4 (sykdom): 4.1 | Tab.: 5 (iht lovverk) 0 |
|---------------------|-------------------------|-------------------------|-------------------------|----------------------------|

* For hund og katt skal individnummer angis:

Godkjent Kopi oversendes utvalget.

Avslått/videresendt forsøksdyrutvalget for avgjørelse. Begrunnelse for avslag skal legges ved.

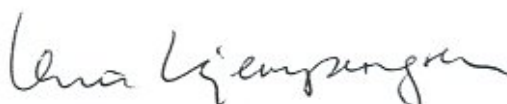
Videresendt forsøksdyrutvalget for avgjørelse. Begrunnelse for videresendelse skal legges ved.

Dato godkjent: 23. januar 2006

Dato godkjenning utløper: 1. juli 2006

Dato sendt FDU: 11/2-06

Ansvarshavendes underskrift:



Prosjekttipe, egenerklæring:

Institutt-rådet ved DNR har pr. 1. juli 2004 vedtatt nye priser for oppdragsforskning og samarbeidsprosjekter med eksterne parter. All oppdragsforskning og samarbeidsprosjekter skal administreres av Forskningsstiftelsen.

Definisjoner:

A: Internt prosjekt: Ingen eksterne interesser involvert.

B: Samarbeidsprosjekt: Forsøk som gjennomføres for og finansieres av eksternt samarbeidspartner og hvor resultatene eies av forskeren som gjennomfører prosjektet.

C: Oppdragsforskning: Forsøk som utføres på oppdrag fra eksternt samarbeidspartner og hvor resultatene tilhører samarbeidspartneren.

Priser:

| | Samarbeidsprosjekt | Oppdragsforskning |
|--|--------------------|-------------------|
| Egenavlede nude mus, pr. dyr: | 250,- | 400,- |
| Mus, oppstalling pr. bur/uke | 30,- | 40,- |
| Egenavlede nude rotter, pr. dyr: | 350,- | 500,- |
| Rotter, oppstalling pr. bur/uke | 35,- | 45,- |
| Eksterne mus, oppstalling pr. bur/uke | 30,- | 40,- |
| Eksterne rotter, oppstalling pr. bur/uke | 35,- | 45,- |

Egenerklæring:

Jeg erklærer med dette at dette prosjektet er et:

A. Internt prosjekt

B. Samarbeidsprosjekt

Sett X der det passer

C. Oppdragsprosjekt

Dato: 27/1-06

Signatur: Kathrine Ree

Til bruk for søkeren:**1. Opplysninger om søkeren (prosjektleder).**

| | | | |
|--|---|---|----------------|
| Navn og stilling: Kathrine Røe, Student Svetlana Stoknes, Student | Arbeidssted og adresse: Strålingsbiologi v/ Dag Rune Olsen, Radiumhospitalet Montebello 0310 OSLO | Tlf.: 92437646/90055289/22935071 Fax:22934607 E-post: kathrr@stud.ntnu.no svetlanastoknes@hotmail.com | |
| Utdannelse: Masterstudenter i medisinsk signalbehandling og biofysikk/medisinsk fysikk. | | | |
| Erfaring med tilsvarende forsøk: Nei | Gjennomgått kurs i forsøksdyrlære: Ja | | |
| Erfaring med denne dyreart: Nei | Kurssted Universitetet i Oslo | Kursnavn Forsøksdyrlære | Kursår 2006 |
| Andre medarbeidere som skal arbeide med dyrene: | | | |
| Navn | Stilling og utdanning | Kurs i forsøksdyrlære | Kontakttelefon |
| Therese Seierstad | Stipendiat | Ja | 22935071 |
| Marita Martinsen | Avd. ingeniør tumorbiologi | Ja | 22935412 |

2. Offentlighet (se vedlagt veiledning)

| |
|--|
| Inneholder søknaden opplysninger av konfidensiell art og som ikke er egnet til offentliggjørelse? Nei I tilfelle ja, legg ved en kort begrunnelse om hvorfor og hvilke opplysninger som ønskes unntatt offentlighet. |
|--|

3. Generelle opplysninger

| | | | |
|---|--|---|---|
| Oppgi forsøkets arbeidstitel: A) Bioimpedans og monitorering av behandlingsrespons. B) In vivo MR spektroskopi og MR diffusjon for evaluering av behandlingsrespons. | | | |
| Skriv to setninger som beskriver forsøket, beregnet på offentliggjøring (arkivbeskrivelse, årsrapport): Det skal utføres bioimpedansmålinger og MR-opptak på mus med implantert tumor for en gruppe mus med strålebehandling og en gruppe uten behandling. | | | |
| Forsøkets varighet i dager/måneder: 5 måneder | Planlagt start (måned/år): Februar 2006 | Planlagt slutt (måned/år): Juni 2006 | Varigheten for det enkelte dyr i timer eller dager: 30 dager |

4. Karakteristikk av de valgte dyr:

| | | | | |
|--|----------------|-------|------------|-------------------------|
| Dyreart | Linje/stamme | Kjønn | Alder/vekt | Antall dyr som behøves: |
| Mus | GBNIH nude mus | ♂ | 20-25gram | 20 |
| Antall dyr ved gjenbruk, jfr. forskriftens § 15: | | | | |

Forventes noen ufysiologisk tilstand hos dyrene som følge av behandling/genmodifikasjon (reproduksjonsproblemer, CNS symptomer, nedsatt immunforsvar, alopeci)
Nei.

Hvilke tiltak skal evt iverksettes/anbefales. Bløte foret, fore dem i forkopp i strø i stedet for i krybbe, avlive dyr, tørke øyne hver dag, redusere lyset i rommet. skru temperaturen opp/skru temperaturen ned, "handle with special care" osv.

Ingen spesielle tiltak.

Genmodifiserte dyr: Ja Nei

| | | |
|--|----|-----|
| Skal dyrene avles ved institusjonen? | Ja | Nei |
| Dato meldt fra til Sosial og helsedirektoratet: | | |
| Dato meldt fra til Direktoratet for naturforvaltning (kun transport) | | |

5. Begrunnelse for valg av dyremodell

Begrunn valget av den aktuelle dyremodell, jfr. forskriftens § 8 – dyreart, linje, spesielle egenskaper, genmodifikasjoner:

Metodikken med å dyrke disse kolorektale cellelinjene som subcutane tumorer på mus er en etablert teknikk og vil gi oss informasjon som man ikke vil kunne oppnå ved eksperimentelle studier *in vitro*.

6. Alternativer til dyreforsøk

Det forutsettes alltid at alternative, vitenskapelig tilfredsstillende, metoder til bruk av levende dyr er vurdert. Redegjør for hvilke alternativer som måtte foreligge, hvorfor disse er forkastet, sett i lys av de 3 R-er:

Erstatning:

I MR spektroskopi får man informasjon om den biokjemiske sammensetningen i et utvalgt volumelement, og forandringer i denne under behandling. Denne sammensetningen er et resultat av metabolske prosesser som finner sted i kroppen. MR diffusjon gir ytterligere informasjon ved at man får kunnskap om diffusjonsegenskapene i tumor og mellom tumor og omliggende vev.

Fysiologi følges underveis og man har svært god eksperimentell kontroll.
In vitro studier kan ikke gi samme type kunnskap.

Poenget med å gjøre forsøk med tumor i mus er å skape bilde av fysiologi i vevet lignende mennesker. Bioimpedansmetoden kan gi informasjon om ledeevnen til vevet som funksjon av volum, uten å ødelegge vevet. Ingen andre metoder *in vitro* kan gi samme informasjon.

Raffinering av dyremodell ift tidligere forsøk

Det gjøres en pilotstudie hvor en kun benytter 2 dosenivå.

Reduksjon av antall forsøksdyr

I og med at forsøket er en pilotstudie er antall dyr redusert til et minimum. Antall dyr er valgt slik at man får tilstrekkelig informasjon til å konkludere.

Prosjektbeskrivelse

7. Bakgrunn og hensikt

Gi en kort presentasjon, i en allment tilgjengelig språkform, for bakgrunn og hensikt med forsøket og angi eventuell hypotese som skal testes. Angi særskilt hvis spesielle lovbestemmelser/krav fra off. myndigheter krever at forsøket skal utføres:

Hypotese: MR spektroskopi, MR diffusjon og bioimpedansmålinger kan benyttes til å monitorere behandlingsrespons.

8. Metodebeskrivelse

Forberedelsen av dyrene før forsøket, beskriv eventuell merkemetode:

Dyrene blir anestesert med katte-zoletilmix (0.15ml/25g mus) under MR-opptak. Katte-zoletilmix (0.05ml/25g) benyttes for bestråling og bioimpedansmålinger.

Behandling under selve forsøket (legg evt med tegning over kirurgisk inngrep)

Xenografts fra de humane kolorektale cellelinjene HT29, HCT116 og SW620 dyrkes ved passasje av tumorvev. Det plasseres to tumorer på hver mus, en på hver side av rumpa. De er ikke plassert på flanken for å unngå puste-artefakter ved MR-avbildning.

Tumorstørrelse monitoreres to ganger per uke og selve forsøket starter når tumorene har nådd en diameter på 10 mm på den korteste siden.

PILOTSTUDIE (12 mus):

DAG 1:

MR-opptak ca 30 min pr mus, bioimpedansmåling ca 10 min pr mus. Dette gjøres for alle musene.

DAG 2:

Bestråling av 8 mus, dose 15 Gy enkeltfraksjon med ⁶⁰Co-apparat.

DAG 3 – 15:

Musene anesteseres og det gjøres et MR-opptak per mus på ulike dager og bioimpedansmålinger 3 dager pr uke.

Musene avlives på ulike tidspunkt underveis. Tumor tas ut og det lages histologiske snitt for bestemmelse av nekrotisk fraksjon. Resttumor legges i flytende nitrogen for eventuell høyopløselig ¹H Magic Angle Spinning Spektroskopi.

Størrelsen på bestrålt og ikke-bestrålt tumor måles to ganger pr. uke og musene avlives når en av tumorene blir 20 mm i diameter.

Det forventes ikke at dyrene vil bli påført ubehag av forsøkene da bioimpedansmålinger og MR-opptak er ikke-invasive metoder.

Etter at musene er tatt ut av dyreavdelingen oppbevares de på LAMYK underveis i forsøket og fram til forsøket er avsluttet.

| |
|--|
| <p>3 av musene vil transporteres til Gaustad for CT-undersøkelse med kontrast for kartlegging av karnettverk. Musene sederes her før de transporteres i privatbil til Gaustad. De holdes varme ved hjelp av varmeputer.</p> |
| <p>Hva måles på dyrene under/etter forsøket</p> <p>Bioimpedansteknikken gir oss informasjon om den elektriske ledningsevnen til biologisk vev og er sterkt avhengig av vevets tilstand.</p> <p>MR-opptak gir et bilde av den kjemiske sammensetningen i tumor samt diffusjonsegenskapene i tumor og mellom tumor og omkringliggende vev.</p> <p>Størrelse på tumor måles 2 ganger pr. uke.</p> |
| <p>Beskriv kort forsøksgrupper og eventuelle kontrolldyr:</p> <p>Resultat av forsøk med bestrålte mus kontrolleres mot mus som ikke har fått strålebehandling.</p> |
| <p>Oppfølging og overvåkning under forsøket, beredskapsordning:</p> <p>Man forventer ingen merkbare fysiologiske endringer hos musene som følge av forsøket utover tumordannelsen.</p> |
| <p>Avlivingsmetode</p> <p>Musene vil avlives ved nakkedislokasjon etter bildetaking etter behandling.</p> |
| <p>Beskrivelse av humant endepunkt – når dyrene skal avlives dersom de anses å lide mer enn beskrevet under pkt 10.</p> <p>Musene forventes ikke å utsettes for lidelse utover den omtalte behandlingen, men de vil bli fulgt opp i hht. interne retningslinjer for klinisk observasjon og vil bli avlivet før forsøkets slutt dersom tumor når 20 mm før forsøket er ferdig eller dersom det viser tydelige tegn til mistrivsel eller har et vekttap på mer enn 10 %.</p> |

9. Sedasjon, anestesi og analgesi

| | | |
|--|---|--|
| <p>Antas forsøket å være forbundet med smerte, skal det normalt nyttes smertelindring, jfr. forskriftens §§ 8 og 14. Ved kroniske forsøk i forbindelse med kirurgiske inngrep skal det detaljert redegjøre for det postoperative regime med hensyn til overvåkning og smertekontroll. Tillatelse til forsøk der dyrene påføres vedvarende eller betydelig smerte, og forsøket er av en slik art at analgetiske midler vanskelig kan benyttes, kan bare gis av Forsøksdyrutvalget.</p> <p><input type="checkbox"/> ikke aktuelt</p> | | |
| <p>Dyrene blir anestisert med zoletil-miks (zolazepam/tiletamin, xylasin og butorphanol)(0.15ml/25g mus) under MR-opptak.</p> <p>For bestråling og bioimpedansmåling anesteseres med zoletil-miks(0.05ml/25g mus).</p> <p>Øyesalve brukes på musene ved anestisering.</p> | | |
| <p>Anestesi (preparat, dose)</p> <p>Zoletil-miks (0.05/0.15ml/25g mus)</p> | <p>Analgesi (preparat, dose)</p> <p>Ingen</p> | <p>Eutanasi (preparat, dose)</p> <p>Nakkedislokasjon</p> |
| <p>Annen medikamentering Hvis det i forbindelse med anestesian anvendes nevro-muskulære blokkere, skal dette angis spesielt med en kort begrunnelse: <input type="checkbox"/> ikke aktuelt</p> | | |

10. Smerte og ubehag

| | |
|--|-------------------|
| Oppgi styrken på forventet maksimal smerte de mest utsatte dyrene kan oppleve under forsøket | Ubetydelig |
| Varighet av smerte | Sekunder |

11. Beregning av antall forsøksdyr

| | | | |
|--|----------------|--------------------------------|-------------------------------|
| Begrunn behovet for antall forsøksdyr. Ved usikkerhet om populasjonsstørrelse skal det gjennomføres pilotforsøk, jfr. forskriftens § 13. Det anbefales å søke hjelp hos statistiker dersom du selv ikke føler deg kompetent. Beskriv forsøksgrupper og gruppestørrelser. | | | |
| Det utføres en pilotstudie der 12 mus brukes. Det er søkt om 20 mus for å sikre at tumor fester seg på minst 12 av musene. Dette er et minimum for å få nok informasjon til å konkludere etter at forsøket er utført. | | | |
| Metode brukt for beregning av antall dyr: | | | |
| Power analyse | Ressurslikning | Annen metode, beskriv nedenfor | ikke aktuelt (begrunn) |
| Dette er en pilotstudie. | | | |

Avvik fra forsøksplanen skal forelegges ansvarshavende/forsøksdyrutvalget for godkjenning. Forsøksdyrutvalget skal ha melding etter avsluttet/avbrutt forsøk gjennom ansvarshavende. Ved prosjekter av lengre varighet skal det leveres kort rapport om status en gang årlig. Forsøksdyrutvalget er primært interessert i opplysninger som belyser konsekvenser for forsøksdyrene og om resultatene berettiger den påkjenning forsøket har vært for dyrene.

Det skal skrives rapport ved forsøksslutt.

Sted og dato: 27/01-2006

Søkerens underskrift: Kathrine Røe Svellava F. Stoknes

Underskrift til eventuell prosjektleder; annen enn søker:

| | | |
|--|--|-----------------|
|  | Forsøksdyrutvalget, P.b. 8147 Dep, 0033 Oslo Telefon / Telefax: 23216584 / 22856501 e-post: fdu@dyrehelsetilsynet.no www.fdu.no | Utvalgets ref.: |
| | SKJEMA TIL BRUK VED SØKNAD OM TILLATELSE TIL Å UTFØRE FORSØK MED DYR. (Eksempel på utfylling: Se www.fdu.no) | |
| Type søknad: <input checked="" type="checkbox"/> Nytt forsøk <input type="checkbox"/> Pilotforsøk <input type="checkbox"/> Videreføring/endring <input type="checkbox"/> Blokk søknad <input type="checkbox"/> Feltforsøk | | |

Til bruk for ansvarshavende ved forsøksdyravdelingen:

Feltforsøk: Angi, så godt som mulig, sted/område hvor forsøket skal gjennomføres

| | |
|---|--|
| Navn på institusjon hvor forsøket er planlagt gjennomført: Ansvarshavende: Lena Kjempengren Adresse: Det Norske Radiumhospital, Dyreavdelingen Montebello Postnummer: 0310 Sted: Oslo e-postadresse: lenak@ulrik.uio.no | Avdelingens nr.: 32 Avdelingens refereransnr.: 06-04-06 Telefon: 22 93 56 45 Telefax: 22 93 56 44 |
|---|--|

| | | | |
|--|--|--|--|
| Type forsøk (A-F): E | Brukes anestesi/analgesi? <input checked="" type="radio"/> Ja <input type="radio"/> Nei | Start (måned/år): 04/06 | Slutt (måned/år): 06/06 |
| Art og type forsøksdyr*: Mus GBN itt under | Antall dyr 30 | Antall dyr ved gjenbruk, jfr. forskriftens § 15: 0 | Er søknaden helt eller delvis fortrolig? <input type="radio"/> Ja <input checked="" type="radio"/> Nei |
| Er lignende forsøk utført tidligere ved avdelingen? <input checked="" type="radio"/> Ja <input type="radio"/> Nei | Er lignende forsøk utført tidligere av forskeren? <input checked="" type="radio"/> Ja <input type="radio"/> Nei | Er prosjektleders kompetanse iht. Landbruksdepts krav? <input checked="" type="radio"/> Ja <input type="radio"/> Nei | |
| EK-statistikk (fyller også ut for feltforsøk): | | | |
| Tab. 1 (kilde): 1.1 | Tab. 2 (formål): 2.1 | Tab. 3 (utdyper 2.4): - | Tab. 4 (sykdom): 4.1 Tab.: 5 (iht lovverk) - |

* For hund og katt skal individnummer angis:

X Godkjent Kopi oversendes utvalget.

Avslått/videresendt forsøksdyrutvalget for avgjørelse. Begrunnelse for avslag skal legges ved.

Videresendt forsøksdyrutvalget for avgjørelse. Begrunnelse for videresendelse skal legges ved.

Dato godkjent: 7/4-06 Dato godkjenning utløper: 1/1-07 Dato sendt FDU: 7/4-06

Ansvarshavendes underskrift: *Lena Kjempengren*

Prosjekttype, egenerklæring:

Institutt-rådet ved DNR har pr. 1. juli 2004 vedtatt nye priser for oppdragsforskning og samarbeidsprosjekter med eksterne parter. All oppdragsforskning og samarbeidsprosjekter skal administreres av Forskningsstiftelsen.

Definisjoner:

A: Internt prosjekt; Ingen eksterne interesser involvert.

B: Samarbeidsprosjekt; Forsøk som gjennomføres for og finansieres av eksternt samarbeidspartner og hvor resultatene eies av forskeren som gjennomfører prosjektet.

C: Oppdragsforskning; Forsøk som utføres på oppdrag fra eksternt samarbeidspartner og hvor resultatene tilhører samarbeidspartneren.

Priser:

| | Samarbeidsprosjekt | Oppdragsforskning |
|--|--------------------|-------------------|
| Egenavlede nude mus, pr. dyr: | 250,- | 400,- |
| Mus, oppstalling pr. bur/uke | 30,- | 40,- |
| Egenavlede nude rotter, pr. dyr: | 350,- | 500,- |
| Rotter, oppstalling pr. bur/uke | 35,- | 45,- |
| Eksterne mus, oppstalling pr. bur/uke | 30,- | 40,- |
| Eksterne rotter, oppstalling pr. bur/uke | 35,- | 45,- |

Egenerklæring:

Jeg erklærer med dette at dette prosjektet er et:

A. Internt prosjekt

B. Samarbeidsprosjekt

Sett X der det passer

C. Oppdragsprosjekt

Dato: 7/4-06

Signatur: Kathrine Røe

Til bruk for søkeren:**1. Opplysninger om søkeren (prosjektleder).**

| | | | |
|---|---|---|----------------|
| Navn og stilling: Kathrine Røe, Student | Arbeidssted og adresse: Strålingsbiologi v/ Dag Rune Olsen, Radiumhospitalet Montebello 0310 OSLO | Tlf.: 92437646/22935071 | |
| Utdannelse: Masterstudent i medisinsk signalbehandling | | Fax: 22934607 | |
| | | E-post: kathrr@stud.ntnu.no | |
| Erfaring med tilsvarende forsøk: Ja | Gjennomgått kurs i forsøksdyrlære: Ja | | |
| Erfaring med denne dyreart: Ja | Kurssted Universitetet i Oslo | Kursnavn Forsøksdyrlære | Kursår 2006 |
| Andre medarbeidere som skal arbeide med dyrene: | | | |
| Navn | Stilling og utdanning | Kurs i forsøksdyrlære | Kontakttelefon |
| Therese Seierstad | Stipendiat | Ja | 22935071 |
| Marita Martinsen | Avd. ingeniør tumorbiologi | Ja | 22935412 |

2. Offentlighet (se vedlagt veiledning)

Inneholder søknaden opplysninger av konfidensiell art og som ikke er egnet til offentliggjørelse?
Nei
I tilfelle ja, legg ved en kort begrunnelse om hvorfor og hvilke opplysninger som ønskes unntatt offentlighet.

3. Generelle opplysninger

| | | | |
|--|--|---|---|
| Oppgi forsøkets arbeidstitel: In vivo MR spektroskopi og MR diffusjon for evaluering av behandlingsrespons. | | | |
| Skriv to setninger som beskriver forsøket, beregnet på offentliggjøring (arkivbeskrivelse, årsrapport): Det skal gis strålesensitiverende medikamentell behandling og/eller strålebehandling til mus som har to implanterte tumorer hver. Deretter skal det foretas opptak av MR spektroskopi og MR diffusjon av disse musene. Kontroll gjøres ved kun å bestråle en av to tumorer og la den andre være kontroll. | | | |
| Forsøkets varighet i dager/måneder: 3 måneder | Planlagt start (måned/år): April 2006 | Planlagt slutt (måned/år): Juni 2006 | Varigheten for det enkelte dyr i timer eller dager: 30 dager |

4. Karakteristikk av de valgte dyr:

| | | | | |
|--|----------------|-------|------------|-------------------------|
| Dyreart | Linje/stamme | Kjønn | Alder/vekt | Antall dyr som behøves: |
| Mus | GBNIH nude mus | ♂ | 20-25gram | 30 |
| Antall dyr ved gjenbruk, jfr. forskriftens § 15: | | | | |

Forventes noen ufysiologisk tilstand hos dyrene som følge av behandling/genmodifikasjon (reproduksjonsproblemer, CNS symptomer, nedsatt immunforsvar, alopeci)
Nei.

Hvilke tiltak skal evt iverksettes/anbefales. Bløte foret, fore dem i forkopp i strø i stedet for i krybbe, avlive dyr, tørke øyne hver dag, redusere lyset i rommet. skru temperaturen opp/skru temperaturen ned, "handle with special care" osv.

Ingen spesielle tiltak utover normalt daglig tilsyn.

Genmodifiserte dyr: Ja Nei

| | | |
|--|----|-----|
| Skal dyrene avles ved institusjonen? | Ja | Nei |
| Dato meldt fra til Sosial og helsedirektoratet: | | |
| Dato meldt fra til Direktoratet for naturforvaltning (kun transport) | | |

5. Begrunnelse for valg av dyremodell

Begrunn valget av den aktuelle dyremodell, jfr. forskriftens § 8 – dyreart, linje, spesielle egenskaper, genmodifikasjoner:

Metodikken med å dyrke disse kolorektale cellelinjene som subcutane tumorer på mus er en etablert teknikk og vil gi oss informasjon som man ikke vil kunne oppnå ved eksperimentelle studier in vitro.

6. Alternativer til dyreforsøk

Det forutsettes alltid at alternative, vitenskapelig tilfredsstillende, metoder til bruk av levende dyr er vurdert. Redegjør for hvilke alternativer som måtte foreligge, hvorfor disse er forkastet, sett i lys av de 3 R-er:

Erstatning:

I MR spektroskopi får man informasjon om den biokjemiske sammensetningen i et utvalgt volumelement, og forandringer i denne under behandling. Denne sammensetningen er et resultat av metabolske prosesser som finner sted i kroppen. MR diffusjon gir ytterligere informasjon ved at man får kunnskap om diffusjonsegenskapene i tumor og mellom tumor og omliggende vev. Ved å kjøre flere diagnostiske metoder på samme mus vil vi få best mulig resultater med færrest mulig mus.

Fysiologi følges underveis og man har svært god eksperimentell kontroll.

In vitro studier kan ikke gi samme type kunnskap.

Ingen andre metoder *in vitro* kan gi samme informasjon.

Raffinering av dyremodell ift tidligere forsøk

Ut i fra en tidligere pilotstudie med 2 dosenivå bestråling og minimal bruk av antall mus, ønskes en videreføring av forsøket med medikamentell behandling kombinert med strålebehandling. Pilotstudiet ga indikasjoner på resultater og antallet mus som trengs i den utvidede studien.

Reduksjon av antall forsøksdyr

Antall dyr er valgt slik at man får tilstrekkelig informasjon til å konkludere. Antall dyr som behøves er vurdert ut i fra pilotforsøket.

Prosjektbeskrivelse

7. Bakgrunn og hensikt

Gi en kort presentasjon, i en allment tilgjengelig språkform, for bakgrunn og hensikt med forsøket og angi eventuell hypotese som skal testes. Angi særskilt hvis spesielle lovbestemmelser/krav fra off. myndigheter krever at forsøket skal utføres:

Hypotese: MR spektroskopi og MR diffusjon kan benyttes til å monitorere behandlingsrespons.

8. Metodebeskrivelse

Forberedelsen av dyrene før forsøket, beskriv eventuell merkemetode:

Dyrene blir anestesert med katte-zoletilmix (0.15ml/25g mus) under MR-opptak. Katte-zoletilmix (0.05ml/25g) benyttes for bestråling og når det skal gis medikamentell behandling.

Dyrene merkes i ørene når de er anestesert.

Behandling under selve forsøket (legg evt med tegning over kirurgisk inngrep)

Xenografts fra den humane kolorektale cellelinjen HT29 dyrkes ved passasje av tumorvev.

Det plasseres to tumorer på hver mus, en på hver side av rumpa. De er ikke plassert på flanken for å unngå puste-artefakter ved MR-avbildning.

Tumorstørrelse monitoreres to ganger per uke og selve forsøket starter når tumorene har nådd en diameter på 10 mm på den korteste siden.

Musene deles opp i tre grupper med 6 mus i hver gruppe. Gruppe 1 får ingen strålesensitiverende behandling, men bestråling med en enkeltfraksjon på 15 Gy på en av de to tumorene. Gruppe 2 får medikamentell behandling med Oxaliplatin (10mg/kg mus) og bestråling med enkeltfraksjon på 15 Gy på en av de to tumorene. Gruppe 3 får behandling med Oxaliplatin (10mg/kg mus) og Capecitabine (359 mg/kg mus) og bestråling av en av de to tumorene med enkeltfraksjon på 15 Gy.

For alle gruppene vil en av tumorene bestråles, mens den andre tumoren blir kontroll til den bestrålte.

OVERSIKT:

DAG 0: Det tas MR-opptak, ca 40 min per mus. Musene blir anestesert med katte-zoletilmix (0.15ml/25g mus) under avbildningen.

DAG 1: Gruppe 2 og 3 gis medikamentell behandling, Oxaliplatin (10 mg/kg mus i 5mg/ml glukoseløsning som tilsvare 0,25 ml/25 g mus), intravenøst. Musene blir anestesert med katte-zoletilmix (0.05ml/25g mus) under behandlingen.

DAG 2: Gruppe 3 får medikamentell behandling, Capecitabine (359 mg/kg mus, tilsvare 9 mg/25 g mus. Capecitabine løses i citrat-buffer som inneholder 5 % arabic gum), med sonde 2 timer før bestråling med enkeltfraksjon på 15 Gy med ⁶⁰Co-apparat.

Gruppe 1 og 2 får også bestråling med enkeltfraksjon på 15 Gy. Musene blir anestesert med katte-zoletilmix (0.05ml/25g mus) under behandling og bestråling.

VIDERE:

Musene anesteseres og det utføres MR-undersøkelse på ulike dager etter behandlingen.
Tumorstørrelse og musene sin vekt blir målt to ganger per uke.

Musene avlives på ulike tidspunkter underveis ved at 2 mus fra hver gruppe tas ut etter MR-opptak på forsøksdagene 3, 8 og 12. Tumor tas ut og det lages histologiske snitt for bestemmelse av nekrotisk fraksjon. Resttumor legges i flytende nitrogen for høyoppløselig ^1H Magic Angle Spinning Spektroskopi.

Musene avlives på ulike tidspunkter underveis, eller når en av tumorene blir 20 mm i største diameter.

Det forventes ikke at dyrene vil bli påført ubehag av forsøkene da MR-opptak er en ikke-invasiv metode.

Etter at musene er tatt ut av dyreavdelingen oppstalles de på LAMYK underveis i forsøket og fram til forsøket er avsluttet.

Hva måles på dyrene under/etter forsøket

MR-opptak gir et bilde av den kjemiske sammensetningen i tumor samt diffusjonsegenskapene i tumor og mellom tumor og omkringliggende vev.

Størrelse på tumor og musene sin vekt måles 2 ganger pr. uke.

Beskriv kort forsøksgrupper og eventuelle kontrolldyr:

Gruppe 1 får ingen medikamentell behandling, gruppe 2 får Oxaliplatin, mens gruppe 3 får både Oxaliplatin og Capecitabine.

Alle gruppene vil bestråles på en av to tumorer med enkeltfraksjon på 15 Gy. Da vil den andre ubestrålte tumoren fungere som kontroll til den bestrålte tumoren.

Oppfølging og overvåkning under forsøket, beredskapsordning:

Ut i fra tidligere forsøk med samme dose Oxaliplatin forventes et vekttap på 8 % og en dødelighet på 8 % som følge av toksisitet.

Tidligere forsøk med Capecitabine har ikke gitt noen tegn på toksisitet og det kan også antas at det i dette forsøket ikke blir noen toksisitet på grunn av Capecitabine.

Foruten dette, vil man ikke forvente noen merkbare fysiologiske endringer hos musene utover tumordannelsen.

Avlivingsmetode

Musene avlives ved nakkedislokasjon etter MR-opptak.

Og musene avlives når tumor på en av sidene på musene når 20 mm i diameter.

Beskrivelse av humant endepunkt – når dyrene skal avlives dersom de anses å lide mer enn beskrevet under pkt 10.

Musene forventes ikke å utsettes for lidelse utover den omtalte behandlingen, men de vil bli fulgt opp i henhold til interne retningslinjer for klinisk observasjon og vil for øvrig bli avlivet før forsøkets slutt dersom tumor når 20 mm som største diameter før forsøket er ferdig eller dersom det viser tydelige tegn til mistriivsel eller har et vekttap på mer enn 10 %.

9. Sedasjon, anestesi og analgesi

Antas forsøket å være forbundet med smerte, skal det normalt nyttes smertelindring, jfr. forskriftens §§ 8 og 14. Ved kroniske forsøk i forbindelse med kirurgiske inngrep skal det detaljert redegjøre for det postoperative regime med hensyn til overvåkning og smertekontroll. Tillatelse til forsøk der dyrene påføres vedvarende eller betydelig smerte, og forsøket er av en slik art at analgetiske midler vanskelig kan benyttes, kan bare gis av Forsøksdyrutvalget.

ikke aktuelt

Dyrene blir anestisert med zoletil-miks (zolazepam/tiletamin, xylasin og butorphanol)(0.15ml/25g mus) under MR-opptak.

For bestråling og medikamentell behandling anestesieres de med zoletil-miks(0.05ml/25g mus).

Nøytral øyesalve brukes på musene ved anestisering.

| Anestesi (preparat, dose) | Analgesi (preparat, dose) | Eutanasi (preparat, dose) |
|---------------------------------------|---------------------------|---------------------------|
| Zoletil-miks (0.05/0.15ml/25g mus) | Ingen | Nakkedislokasjon |

Annen medikamentering Hvis det i forbindelse med anestiseringen anvendes nevrologiske blokkere, skal dette angis spesielt med en kort begrunnelse: ikke aktuelt

10. Smerte og ubehag

Oppgi styrken på forventet maksimal smerte de mest utsatte dyrene kan oppleve under forsøket

Ubetydelig

Varighet av smerte

Sekunder

11. Beregning av antall forsøksdyr

Begrunn behovet for antall forsøksdyr. Ved usikkerhet om populasjonsstørrelse skal det gjennomføres pilotforsøk, jfr. forskriftens § 13. Det anbefales å søke hjelp hos statistiker dersom du selv ikke føler deg kompetent. Beskriv forsøksgrupper og gruppestørrelser.

Antall dyr er beregnet ut i fra at hvor mange man må ha for å få nok informasjon for å konkludere. Dette er beregnet ut ifra resultatene fra pilotstudien.

Metode brukt for beregning av antall dyr:

Power analyse Ressurslikning Annen metode, beskriv nedenfor **ikke aktuelt (begrunn)**

Avvik fra forsøksplanen skal forelegges ansvarshavende/forsøksdyrutvalget for godkjenning. Forsøksdyrutvalget skal ha melding etter avsluttet/avbrutt forsøk gjennom ansvarshavende. Ved prosjekter av lengre varighet skal det leveres kort rapport om status en gang årlig. Forsøksdyrutvalget er primært interessert i opplysninger som belyser konsekvenser for forsøksdyrene og om resultatene berettiger den påkjenning forsøket har vært for dyrene.

Det skal skrives rapport ved forsøksslutt.

Sted og dato: Montebello 7. ^{april} ~~mars~~ 2006

Søkerens underskrift: *Kathrine Røe*

Underskrift til eventuell prosjektleder; annen enn søker:

Appendix B

The results achieved in this work are listed in tables in this Appendix. First, the results from Experiment 1 are given, before the results from Experiment 2.

| Tumor No | Dose [Gy] | SD [%] |
|----------|-----------|--------|
| 1 | 16.101 | 10.5 |
| 2 | 16.589 | 2.0 |
| 3 | 16.252 | 3.6 |
| 4 | 15.784 | 4.8 |
| 5 | 12.220 | 13.6 |
| 6 | 15.774 | 7.0 |
| 7 | 16.570 | 4.6 |
| 8 | 16.730 | 3.0 |
| 9 | 17.033 | 2.6 |
| 10 | 15.352 | 10.7 |
| 11 | 16.146 | 3.7 |
| 12 | 17.201 | 3.8 |
| 13 | 16.291 | 3.3 |
| 14 | 15.555 | 6.3 |
| 15 | 16.095 | 2.9 |
| 16 | 14.353 | 2.6 |

Table 1: TLD measurements of radiation dose for all the tumors in Group 1 in Experiment 1. The results are given as dose in Gy and standard deviation (SD) in %.

| Tumor No | 01/02 | 06/02 | 09/02 | 13/02 | 16/02 | 20/02 | 23/02 | 27/02 | 02/03 | 06/03 | 09/03 |
|----------|-------|-------|-------|-------|-------|-------|-------|--------|--------|-------|-------|
| 1 | 87.1 | 187.9 | 187.9 | 269.3 | 466.3 | | | | | | |
| 2 | 47.7 | 143.7 | 268.0 | 423.9 | 423.9 | | | | | | |
| 3 | 41.9 | 95.0 | 205.2 | 268.0 | 381.5 | | | | | | |
| 4 | 37.7 | 143.7 | 143.7 | 264.9 | 448.7 | | | | | | |
| 5 | 14.1 | 65.4 | 220.8 | 220.8 | 235.5 | 334.9 | 435.4 | | | | |
| 6 | 47.7 | 95.0 | 143.7 | 143.7 | 179.5 | 179.5 | 448.7 | | | | |
| 7 | 72.0 | 165.8 | 205.2 | 243.6 | 435.4 | 468.9 | 519.2 | 657.1 | 811.2 | | |
| 8 | 37.7 | 113.0 | 169.6 | 188.4 | 216.7 | 294.9 | 294.9 | 385.2 | 435.4 | | |
| 9 | 72.0 | 165.8 | 250.2 | 250.2 | 402.7 | 663.5 | 899.7 | 899.7 | 899.7 | | |
| 10 | 4.2 | 4.2 | 14.1 | 33.5 | 53.0 | 160.1 | 179.0 | 435.4 | 661.2 | | |
| 11 | 53.0 | 113.0 | 179.5 | 220.8 | 268.0 | 301.4 | 448.7 | 1003.6 | 1038.2 | | |
| 12 | 4.2 | 22.4 | 47.7 | 65.4 | 124.3 | 158.3 | 190.0 | 226.1 | 287.4 | | |
| 13 | 65.4 | 113.0 | 179.5 | 179.5 | 205.2 | 279.7 | 720.6 | 942.0 | 942.0 | | |
| 14 | 4.2 | 47.7 | 47.7 | 84.8 | 150.7 | 207.2 | 307.7 | 529.4 | 529.4 | | |
| 15 | 4.2 | 72.0 | 85.0 | 85.0 | 131.9 | 160.1 | 169.6 | 264.9 | 279.7 | | |
| 16 | 4.2 | 25.6 | 143.7 | 318.2 | 318.2 | 551.1 | 706.5 | | | | |
| 17 | 78.5 | 154.8 | 179.5 | 321.4 | 402.7 | 549.5 | 759.9 | 759.9 | 759.9 | 759.9 | |
| 18 | 4.2 | 33.5 | 87.1 | 87.1 | 179.5 | 179.5 | 179.5 | 250.2 | 250.2 | 309.1 | |
| 19 | 4.2 | 22.4 | 33.5 | 33.5 | 143.7 | 179.5 | 230.8 | 318.2 | 434.8 | 628.0 | |
| 20 | 4.2 | 4.2 | 14.1 | 22.4 | 33.5 | 111.2 | 117.8 | 230.8 | 282.1 | 323.8 | |
| 21 | 25.6 | 53.0 | 113.0 | 143.7 | 220.8 | 235.5 | 368.0 | 635.9 | 657.1 | 915.8 | |
| 22 | 4.2 | 4.2 | 14.1 | 22.4 | 47.7 | 113.0 | 113.0 | 220.8 | 220.8 | 220.8 | 284.7 |
| 23 | 14.1 | 25.6 | 33.5 | 87.1 | 113.0 | 179.5 | 218.0 | 284.7 | 284.7 | 586.1 | 741.8 |
| 24 | 4.2 | 4.2 | 14.1 | 14.1 | 22.4 | 33.5 | 79.5 | 142.5 | 334.9 | 334.9 | |

Table 2: Tumor volume (mm^3) calculated from slide caliper measurements prior to start of Experiment 1. Tumors 1 to 16 are Group 1 and tumors 17 to 24 are Group 2. Group 1 tumors were included on three consecutive Mondays (February 20, February 27 and March 6). Group 2 tumors were excised after MR examinations and sacrifice at two different dates (March 7 and March 9).

| Tumor No | Day 1 | Day 3 | Day 5 | Day 8 | Day 12 |
|----------|--------|--------|--------|-------|--------|
| 1 | 519.5 | 549.5 | 575.7 | 549.5 | 549.5 |
| 2 | 519.5 | 575.7 | 575.7 | 523.3 | 523.3 |
| 3 | 495.9 | 519.5 | 575.7 | 472.3 | 523.3 |
| 4 | 448.7 | 472.3 | 495.9 | 523.3 | 548.1 |
| 5 | 435.4 | 614.0 | 635.9 | 635.9 | |
| 6 | 448.7 | 523.3 | 549.5 | 523.3 | |
| 7 | 811.2 | 811.2 | 811.2 | 785.0 | |
| 8 | 435.4 | 551.1 | 491.5 | 468.9 | |
| 9 | 899.7 | 1055.0 | 854.9 | | |
| 10 | 661.2 | 635.9 | 551.1 | | |
| 11 | 1038.2 | 1076.5 | 1044.8 | | |
| 12 | 661.7 | 763.0 | 602.9 | | |
| 13 | 942.0 | 942.0 | | | |
| 14 | 529.4 | 529.4 | | | |
| 15 | 279.7 | 445.1 | | | |
| 16 | 706.5 | 981.5 | | | |
| 17 | 865.1 | | | | |
| 18 | 368.4 | | | | |
| 19 | 865.1 | | | | |
| 20 | 453.7 | | | | |
| 21 | 1139.8 | | | | |
| 22 | 334.9 | | | | |
| 23 | 942.0 | | | | |
| 24 | 415.9 | | | | |

Table 3: Tumor volume (mm^3) calculated from slide caliper measurements at the five experiment days in Experiment 1. Tumors 1 to 16 are Group 1 and tumors 17 to 24 are Group 2. Irradiation of tumors 1 - 16 was performed at Day 2.

| Tumor No | Day 1 | Day 3 | Day 5 | Day 8 | Day 12 |
|----------|-------|-------|-------|-------|--------|
| 1 | 0.59 | 0.47 | 0.60 | 0.56 | 0.55 |
| 2 | 0.58 | 0.71 | 0.72 | 0.50 | 0.53 |
| 3 | 0.43 | 0.65 | 0.59 | 0.69 | 0.64 |
| 4 | 0.45 | 0.37 | 0.51 | 0.46 | 0.57 |
| 5 | 0.53 | 0.63 | 0.58 | 0.61 | |
| 6 | 0.51 | 0.59 | 0.51 | 0.63 | |
| 7 | 1.11 | 1.11 | 0.97 | 1.08 | |
| 8 | 0.32 | 0.44 | 0.49 | 0.50 | |
| 9 | 1.10 | 1.04 | 0.89 | | |
| 10 | 0.95 | 0.87 | 0.79 | | |
| 11 | 1.22 | 1.35 | 1.00 | | |
| 12 | 0.72 | 0.74 | 0.67 | | |
| 13 | 0.89 | 0.91 | | | |
| 14 | 0.72 | 0.77 | | | |
| 15 | 0.29 | 0.32 | | | |
| 16 | 1.01 | 0.94 | | | |
| 17 | 0.63 | | | | |
| 18 | 0.58 | | | | |
| 19 | 1.00 | | | | |
| 20 | 0.55 | | | | |
| 21 | 1.17 | | | | |
| 22 | 0.35 | | | | |
| 23 | 0.76 | | | | |
| 24 | 0.36 | | | | |

Table 4: Tumor volume (cm³) calculated from the T₂-weighted MR images in Experiment 1. Tumors 1 to 16 are Group 1 and tumors 17 to 24 are Group 2. Irradiation of tumors 1 - 16 was performed at Day 2.

| Tumor No | Normalized choline ratio ($\times 10^{-3}$) | | | | | | | | | |
|----------|---|-------|-------|-------|--------|--------------------------------|-------|-------|-------|--------|
| | Short echo time (TE: 35 ms) | | | | | Long echo time (TE: 144 ms) | | | | |
| | Day 1 | Day 3 | Day 5 | Day 8 | Day 12 | Day 1 | Day 3 | Day 5 | Day 8 | Day 12 |
| 1 | 0.579 | 0.371 | 0.165 | 0.520 | 0.408 | 0.398 | 0.346 | 0.153 | 0.277 | 0.096 |
| 2 | 0.534 | 0.796 | 0.364 | 0.147 | 0.552 | 0.303 | -* | 0.387 | 0.147 | 0.292 |
| 3 | 0.103 | 0.209 | 0.155 | 0.764 | 0.282 | 0.171 | 0.177 | 0.040 | 0.378 | 0.262 |
| 4 | 0.432 | 0.269 | 0.227 | 0.141 | 0.636 | 0.047 | 0.356 | 0.080 | 0.111 | 0.313 |
| 5 | 0.603 | 0.779 | 0.379 | 0.250 | | 0.439 | 0.441 | 0.359 | 0.161 | |
| 6 | 0.617 | 1.193 | 0.971 | 0.633 | | 0.466 | 0.546 | 0.036 | 0.042 | |
| 7 | 0.364 | 0.368 | 0.742 | 0.326 | | 0.179 | 0.120 | 0.167 | 0.155 | |
| 8 | 0.615 | 0.514 | 0.747 | 0.423 | | 0.121 | 0.393 | 0.342 | 0.105 | |
| 9 | 0.092 | 0.463 | 0.148 | | | 0.021 | 0.048 | 0.063 | | |
| 10 | 0.379 | 0.285 | 0.219 | | | 0.537 | 0.240 | 0.319 | | |
| 11 | 0.648 | 0.566 | 0.530 | | | 0.460 | 0.190 | 0.238 | | |
| 12 | 0.151 | 0.339 | 0.081 | | | 0.182 | 0.207 | 0.081 | | |
| 13 | 0.266 | 1.530 | | | | 0.095 | 0.228 | | | |
| 14 | 0.556 | 0.530 | | | | 0.173 | 0.050 | | | |
| 15 | 0.884 | 1.522 | | | | 0.280 | 0.548 | | | |
| 16 | 0.746 | 0.560 | | | | 0.348 | 0.344 | | | |
| 17 | 0.868 | | | | | 0.140 | | | | |
| 18 | 0.538 | | | | | 0.354 | | | | |
| 19 | 0.427 | | | | | 0.293 | | | | |
| 20 | 0.684 | | | | | 0.229 | | | | |
| 21 | 0.723 | | | | | 0.245 | | | | |
| 22 | 0.398 | | | | | 0.299 | | | | |
| 23 | 0.571 | | | | | 0.287 | | | | |
| 24 | 0.410 | | | | | 0.192 | | | | |

Table 5: An assessment of the choline peak area in Experiment 1 relative to the unsuppressed 35 ms TE water area in the same voxel is expressed as normalized metabolite ratio. Choline refers to the trimethylamine ($-N(CH_3)_3$) resonance at 3.21 ppm. All voxels were 64 mm^3 . *Missing data due to technical errors. Irradiation of tumors 1 - 16 was performed at Day 2.

| Tumor No | Day 1 | Day 3 | Day 5 | Day 8 | Day 12 |
|----------|------------|------------|------------|------------|------------|
| 1 | 56.2 (6.8) | 61.4 (5.3) | 51.0 (5.6) | 53.7 (3.6) | 63.5 (5.5) |
| 2 | 52.6 (6.9) | 51.8 (5.8) | 53.5 (6.6) | 56.2 (8.6) | 62.1 (5.7) |
| 3 | 65.7 (5.4) | 60.9 (7.5) | 53.7 (5.2) | 54.0 (4.1) | 58.4 (7.4) |
| 4 | 54.1 (5.8) | 57.0 (4.1) | 56.6 (3.9) | 55.5 (4.4) | 59.8 (6.0) |
| 5 | 53.3 (9.1) | 56.3 (6.5) | 55.3 (4.0) | 56.8 (5.9) | |
| 6 | 54.2 (4.5) | 55.8 (6.1) | 52.4 (7.0) | 48.7 (6.4) | |
| 7 | 62.5 (5.2) | 60.1 (4.2) | 57.9 (4.2) | 59.7 (6.7) | |
| 8 | 54.1 (4.4) | 55.2 (5.7) | 54.4 (3.3) | 53.3 (5.2) | |
| 9 | 59.7 (4.3) | 64.8 (4.8) | 56.2 (3.1) | | |
| 10 | 57.8 (6.1) | 61.9 (4.3) | 67.1 (6.0) | | |
| 11 | 58.2 (3.8) | 53.8 (8.6) | 51.1 (7.5) | | |
| 12 | 61.5 (4.4) | 60.2 (4.0) | 59.5 (4.3) | | |
| 13 | 58.2 (6.8) | 59.9 (5.2) | | | |
| 14 | 58.1 (6.5) | 53.6 (8.5) | | | |
| 15 | 62.7 (6.8) | 64.8 (3.9) | | | |
| 16 | 57.2 (6.3) | 52.0 (5.2) | | | |
| 17 | 60.1 (5.6) | | | | |
| 18 | 54.1 (3.9) | | | | |
| 19 | 57.3 (4.6) | | | | |
| 20 | 58.7 (4.8) | | | | |
| 21 | 59.7 (7.7) | | | | |
| 22 | 49.5 (6.9) | | | | |
| 23 | 56.9 (5.4) | | | | |
| 24 | 58.1 (3.9) | | | | |

Table 6: Tumor ADCs (SD) in 10^{-5} mm²/s at the five experiment days in Experiment 1. Irradiation of tumors 1 - 16 was performed at Day 2.

| Tumor No | Dose [Gy] | SD [%] |
|-----------|-----------|--------|
| IR-1 | 9.505* | 16.6 |
| IR-2 | 13.967 | 7.7 |
| IR-3 | 14.648 | 4.9 |
| IR-4 | 16.736 | 5.5 |
| IR-5 | 16.639 | 0.4 |
| IR-C-1 | 15.499 | 2.1 |
| IR-C-2 | 11.028 | 11.4 |
| IR-C-3 | 13.888 | 2.4 |
| IR-C-OX-1 | 12.441 | 8.4 |
| IR-C-OX-2 | 15.681 | 8.4 |
| IR-C-OX-3 | 13.426 | 9.9 |
| IR-C-OX-4 | 16.512 | 0.8 |
| IR-C-OX-5 | 16.213 | 2.4 |
| IR-C-OX-6 | 16.950 | 5.1 |
| IR-C-OX-7 | -** | - |

Table 7: TLD measurements of radiation dose for all the mices' left tumors in Experiment 2. The results are given as dose in Gy and standard deviation (SD) in %. * Recieved a low radiation dose. ** Dose not measured.

| Group | Mouse No | Day 1 | Day 2 | Day 3 | Day 4 | Day 5 | Day 10 |
|-------|----------|-------|-------|-------|-------|-------|--------|
| 1 | 1 | 26.26 | 26.52 | 25.56 | 26.08 | 25.75 | |
| 1 | 2 | 31.11 | 31.32 | 30.93 | 30.00 | 30.30 | |
| 1 | 3 | 28.14 | 27.58 | 27.74 | 26.65 | 27.85 | 29.51 |
| 1 | 4 | 27.32 | 26.91 | 26.37 | 26.11 | 25.68 | 27.18 |
| 1 | 5 | 29.54 | 29.63 | 29.09 | 28.41 | 28.66 | |
| 2 | 1 | 27.72 | 26.74 | 25.71 | 26.08 | 26.66 | |
| 2 | 2 | 26.91 | 26.38 | 25.30 | 23.73 | 25.43 | |
| 2 | 3 | 25.20 | 24.67 | 23.25 | 22.69 | 22.65 | 24.69 |
| 2 | 4 | 29.48 | 29.43 | | | | |
| 3 | 1 | 22.25 | 23.23 | 22.68 | 20.85 | 22.00 | 21.85 |
| 3 | 2 | 24.18 | 23.12 | 22.75 | 22.08 | 22.38 | |
| 3 | 3 | 23.50 | 23.52 | 22.47 | | | |
| 3 | 4 | 26.09 | 25.55 | 23.85 | 23.72 | 22.90 | |
| 3 | 5 | 25.47 | 24.35 | 23.32 | 21.89 | 21.74 | 24.59 |
| 3 | 6 | 24.50 | 23.01 | 22.06 | 21.15 | 20.98 | 27.18 |
| 3 | 7 | 24.37 | 23.89 | 23.02 | 22.74 | 22.88 | 24.12 |

Table 8: Mice body weights (g) measured during chemotherapy (Day 1 - Day 5) and Day 10 in Experiment 2.

| Tumor No | 30/03 | 03/04 | 06/04 | 10/04 | 12/04 | 17/04 | 20/04 | 24/04 | 27/04 | 01/05 | 04/05 | 08/05 | 11/05 |
|-----------|-------|-------|-------|-------|-------|-------|-------|--------|--------|-------|-------|-------|-------|
| IR-1 | 41.9 | 41.9 | 41.9 | 192.3 | 192.3 | 220.8 | 205.2 | 230.8 | 566.8 | | | | |
| IR-2 | 104.7 | 104.7 | 188.4 | 307.7 | 418.7 | 435.4 | 435.4 | 593.5 | 1139.8 | | | | |
| IR-3 | 8.2 | 33.5 | 113.0 | 220.8 | 268.0 | 340.3 | 634.7 | 634.7 | 1063.0 | | | | |
| IR-4 | 4.2 | 8.2 | 8.2 | 14.1 | 14.1 | 22.4 | 33.5 | 33.5 | 179.5 | 179.5 | 179.5 | 235.5 | 334.9 |
| IR-5 | 4.2 | 4.2 | 4.2 | 4.2 | 14.1 | 14.1 | 33.5 | 47.7 | 47.7 | 47.7 | 87.1 | 113.0 | 113.0 |
| 1 | 4.2 | 4.2 | 18.8 | 18.8 | 25.6 | 33.5 | 33.5 | 33.5 | 65.4 | | | | |
| 3 | 4.2 | 65.4 | 165.8 | 218.0 | 301.4 | 402.7 | 728.2 | 759.9 | 1282.4 | | | | |
| 4 | 4.2 | 4.2 | 4.1 | 4.2 | 25.6 | 87.1 | 113.0 | 113.0 | 179.5 | 179.5 | 381.5 | 381.5 | 402.7 |
| 5 | 4.2 | 4.2 | 4.1 | 4.2 | 14.1 | 22.4 | 33.5 | 65.4 | 65.4 | 65.4 | 65.4 | 65.4 | 65.4 |
| IR-C-1 | 33.5 | 33.5 | 65.4 | 220.8 | 268.0 | 321.4 | 321.4 | 321.4 | 472.3 | | | | |
| IR-C-2 | 22.4 | 47.7 | 65.4 | 220.8 | 268.0 | 268.0 | 268.0 | 268.0 | 381.5 | | | | |
| IR-C-3 | 8.2 | 14.1 | 16.5 | 18.8 | 18.8 | 18.8 | 41.9 | 65.4 | 65.4 | | | | |
| IR-C-4 | 4.2 | 4.2 | 4.2 | 4.2 | 25.6 | 87.1 | 113.0 | 113.0 | 179.5 | 179.5 | 381.5 | 381.5 | 402.7 |
| IR-C-5 | 4.2 | 4.2 | 4.2 | 4.2 | 14.1 | 22.4 | 33.5 | 65.4 | 65.4 | 65.4 | 65.4 | 65.4 | 65.4 |
| C-1 | 14.1 | 22.4 | 33.5 | 65.4 | 102.9 | 154.8 | 179.5 | 179.5 | 340.3 | | | | |
| C-2 | 14.1 | 78.5 | 78.5 | 268.0 | 301.4 | 359.2 | 359.2 | 635.9 | 1130.4 | | | | |
| C-3 | 22.4 | 78.5 | 192.3 | 321.4 | 381.5 | 381.5 | 904.3 | 1238.2 | 1538.6 | | | | |
| C-4 | 8.2 | 8.2 | 8.2 | 8.2 | 33.5 | 65.4 | 65.4 | 87.1 | 113.0 | 113.0 | 179.5 | 220.8 | 381.5 |
| C-5 | 4.2 | 4.2 | 4.19 | 4.2 | 14.1 | 14.1 | 14.1 | 14.1 | 14.1 | 14.1 | 14.1 | 14.1 | |
| IR-C-OX-1 | 16.5 | 25.6 | 85.0 | 110.8 | 141.3 | 160.1 | 187.9 | 415.9 | 508.7 | | | | |
| IR-C-OX-2 | 22.4 | 33.5 | 154.8 | 381.5 | 575.7 | 728.2 | 830.5 | 1335.3 | 1383.0 | | | | |
| IR-C-OX-3 | 22.4 | 22.4 | 72.0 | 179.5 | 179.5 | 205.2 | 205.2 | 268.0 | 423.9 | | | | |
| IR-C-OX-4 | 4.2 | 4.2 | 4.2 | 4.2 | 14.1 | 22.4 | 33.5 | 33.5 | 41.9 | 65.4 | 113.0 | 179.5 | 205.2 |
| IR-C-OX-5 | 8.2 | 8.2 | 22.4 | 22.4 | 33.5 | 33.5 | 33.5 | 33.5 | 65.4 | 65.4 | 65.4 | 65.4 | 98.1 |
| IR-C-OX-6 | 4.2 | 4.2 | 14.1 | 14.1 | 14.1 | 22.4 | 47.7 | 53.0 | 50.2 | 50.2 | 113.0 | 131.9 | 131.9 |
| C-OX-1 | 8.2 | 47.7 | 47.7 | 165.8 | 192.3 | 192.3 | 192.3 | 268.0 | 334.9 | | | | |
| C-OX-2 | 4.2 | 4.2 | 22.4 | 33.5 | 65.4 | 78.5 | 78.5 | 78.5 | 179.5 | | | | |
| C-OX-3 | 33.5 | 65.4 | 154.8 | 321.4 | 381.5 | 402.7 | 423.9 | 466.3 | 949.9 | | | | |
| C-OX-4 | 4.2 | 4.2 | 4.2 | 14.1 | 25.6 | 33.5 | 113.0 | 113.0 | 113.0 | 179.5 | 179.5 | 218.0 | 423.9 |
| C-OX-5 | 8.2 | 8.2 | 22.4 | 28.9 | 41.9 | 78.5 | 78.5 | 91.6 | 264.9 | 264.9 | 334.9 | 466.3 | 508.7 |
| C-OX-6 | 4.2 | 4.2 | 14.1 | 14.1 | 14.1 | 22.4 | 65.4 | 72.0 | 85.0 | 85.0 | 179.5 | 192.3 | 423.9 |

Table 9: Tumor volumes (mm^3) calculated from slide caliper measurements prior to start of Experiment 2. Tumors were included at two Mondays (May 1 and May 15).

| Tumor No | Day 1 | Day 3 | Day 5 | Day 10 |
|-----------|--------|--------|--------|--------|
| IR-1 | 661.2 | 706.5 | | |
| IR-2 | 1356.5 | 1431.8 | | |
| IR-3 | 1282.4 | 1194.0 | 1194.0 | 1538.6 |
| IR-4 | 1017.4 | 979.7 | 1055.0 | 854.9 |
| IR-5 | 165.8 | 122.5 | | |
| 1 | 113.0 | 143.7 | | |
| 3 | 1884.0 | 1884.0 | 2001.8 | 3136.9 |
| 4 | 601.8 | 634.7 | 865.1 | 696.6 |
| 5 | 179.5 | 192.3 | | |
| IR-C-1 | 519.5 | 472.3 | | |
| IR-C-2 | 549.5 | 445.1 | | |
| IR-C-3 | 143.7 | 165.8 | 131.9 | 145.0 |
| IR-C-4 | 508.7 | | | |
| IR-C-5 | 949.9 | | | |
| C-1 | 340.3 | 359.2 | | |
| C-2 | 1431.8 | 1431.8 | | |
| C-3 | 1650.5 | 1650.5 | 1705.5 | 1884.0 |
| C-4 | 495.9 | | | |
| C-5 | 14.1 | | | |
| IR-C-OX-1 | 593.5 | 593.5 | 491.5 | 491.5 |
| IR-C-OX-2 | 2263.2 | 1592.0 | | |
| IR-C-OX-3 | 566.8 | | | |
| IR-C-OX-4 | 256.4 | 230.8 | | |
| IR-C-OX-5 | 169.6 | 169.6 | 205.1 | 126.6 |
| IR-C-OX-6 | 179.5 | 267.9 | 205.1 | 179.5 |
| C-OX-1 | 523.3 | 523.3 | 523.3 | 549.5 |
| C-OX-2 | 359.2 | 301.4 | | |
| C-OX-3 | 1130.4 | | | |
| C-OX-4 | 508.7 | 566.8 | | |
| C-OX-5 | 785.0 | 865.4 | 435.4 | 468.9 |
| C-OX-6 | 680.3 | 628.0 | 628.0 | 692.4 |

Table 10: Tumor volume (mm^3) calculated from slide caliper measurements at the four experiment days in Experiment 2.

| Tumor No | Day 1 | Day 3 | Day 5 | Day 10 |
|-----------|-------|-------|-------|--------|
| IR-1 | 1.05 | 1.07 | 1.03 | |
| IR-2 | 1.24 | 1.21 | 1.16 | |
| IR-3 | 1.10 | 1.08 | 1.09 | 1.19 |
| IR-4 | 0.84 | 0.77 | 0.75 | 0.79 |
| IR-5 | 0.15 | 0.14 | 0.14 | |
| 1 | 0.06 | 0.06 | 0.07 | |
| 3 | 1.46 | 1.55 | 1.70 | 2.03 |
| 4 | 0.44 | 0.48 | 0.49 | 0.52 |
| 5 | 0.10 | 0.14 | 0.16 | |
| IR-C-1 | 0.86 | 0.85 | 0.82 | |
| IR-C-2 | 0.64 | 0.64 | 0.60 | |
| IR-C-3 | 0.12 | 0.12 | 0.10 | 0.11 |
| IR-C-4 | 0.35 | | | |
| IR-C-5 | 0.97 | | | |
| C-1 | 0.33 | 0.35 | 0.39 | |
| C-2 | 1.80 | 1.83 | 1.96 | |
| C-3 | 1.52 | 1.54 | 1.63 | 1.74 |
| C-4 | 0.54 | | | |
| C-5 | 0.01 | | | |
| IR-C-OX-1 | 0.76 | 0.75 | 0.74 | 0.72 |
| IR-C-OX-2 | 1.99 | 1.81 | 1.77 | |
| IR-C-OX-3 | 0.63 | 0.56 | | |
| IR-C-OX-4 | 0.24 | 0.21 | 0.16 | |
| IR-C-OX-5 | 0.12 | 0.11 | 0.09 | 0.10 |
| IR-C-OX-6 | 0.21 | 0.20 | 0.18 | 0.16 |
| IR-C-OX-7 | 0.16 | 0.15 | 0.14 | 0.13 |
| C-OX-1 | 0.44 | 0.47 | 0.49 | 0.47 |
| C-OX-2 | 0.37 | 0.35 | 0.36 | |
| C-OX-3 | 1.13 | 1.18 | | |
| C-OX-4 | 0.51 | 0.46 | 0.41 | |
| C-OX-5 | 0.79 | 0.75 | 0.72 | 0.72 |
| C-OX-6 | 0.53 | 0.54 | 0.56 | 0.53 |
| C-OX-7 | 0.42 | 0.44 | 0.46 | 0.43 |

Table 11: Tumor volume (cm^3) calculated from the T_2 -weighted MR images in Experiment 2.

| Tumor No | Day 1 | Day 3 | Day 5 | Day 10 |
|-----------|-------------|-------------|-------------|-------------|
| IR-1 | 62.5 (6.7) | 73.5 (10.9) | 58.2 (5.3) | |
| IR-2 | 61.1 (9.4) | 70.5 (9.4) | 58.6 (5.9) | |
| IR-3 | 64.3 (11.1) | 77.3 (11.9) | 66.7 (11.8) | 71.4 (11.6) |
| IR-4 | 54.8 (6.2) | 62.0 (8.6) | 58.5 (6.4) | 66.9 (7.3) |
| IR-5 | 57.1 (5.8) | 60.7 (5.1) | 54.6 (5.7) | |
| 1 | 57.7 (6.3) | 55.9 (6.4) | 57.5 (5.3) | |
| 3 | 66.2 (7.5) | 68.4 (8.3) | 61.1 (9.2) | 59.2 (10.6) |
| 4 | 58.4 (5.3) | 58.8 (6.4) | 62.9 (6.6) | 64.6 (9.8) |
| 5 | 52.1 (3.9) | 53.7 (3.9) | 54.2 (2.8) | |
| IR-C-1 | 58.6 (4.8) | 62.1 (7.5) | 60.4 (6.8) | |
| IR-C-2 | 57.8 (4.0) | 61.7 (6.8) | 59.4 (5.3) | |
| IR-C-3 | 56.7 (6.9) | 61.1 (6.2) | 55.6 (6.3) | 66.1 (9.3) |
| IR-C-4 | 55.1 (4.8) | | | |
| IR-C-5 | 57.9 (6.6) | | | |
| C-1 | 61.6 (10.1) | 61.2 (11.7) | 61.8 (8.9) | |
| C-2 | 56.3 (7.0) | 60.7 (6.8) | 56.1 (9.1) | |
| C-3 | 61.2 (8.8) | 62.1 (6.7) | 60.1 (8.7) | 58.8 (11.2) |
| C-4 | 55.0 (7.7) | | | |
| C-5 | 56.1 (4.3) | | | |
| IR-C-OX-1 | 61.0 (6.3) | 73.7 (6.3) | 55.0 (5.8) | 69.2 (5.9) |
| IR-C-OX-2 | 68.7 (9.4) | 60.0 (4.5) | 61.9 (6.9) | |
| IR-C-OX-3 | 62.7 (6.0) | 60.2 (8.4) | | |
| IR-C-OX-4 | 49.0 (3.6) | 56.8 (6.4) | 54.9 (4.9) | |
| IR-C-OX-5 | 57.2 (10.1) | 62.3 (13.4) | 56.7 (2.5) | 74.0 (5.9) |
| IR-C-OX-6 | 50.6 (6.9) | 57.1 (8.2) | 69.1 (4.9) | 74.6 (7.9) |
| IR-C-OX-7 | 59.8 (4.2) | 63.0 (7.2) | 57.7 (5.4) | 73.3 (3.9) |
| C-OX-1 | 64.5 (12.4) | 68.2 (13.1) | 68.9 (9.5) | 73.2 (13.2) |
| C-OX-2 | 62.5 (5.1) | 73.4 (5.7) | 60.1 (6.4) | |
| C-OX-3 | 63.6 (9.6) | 71.4 (10.9) | | |
| C-OX-4 | 50.7 (4.2) | 57.6 (8.5) | 57.7 (6.2) | |
| C-OX-5 | 59.1 (9.3) | 61.5 (9.1) | 59.9 (8.7) | 72.6 (9.9) |
| C-OX-6 | 61.7 (4.8) | 60.4 (4.7) | 59.3 (6.9) | 70.1 (5.1) |
| C-OX-7 | 57.2 (8.7) | 49.2 (7.7) | 57.6 (6.5) | 72.1 (8.8) |

Table 12: Tumor ADCs (SD) in 10^{-5} mm²/s at the four experiment days in Experiment 2.

